5-6-2021

Translating macroscale concepts to microfluidic devices

Nicole Hill
nsh3709@rit.edu

R·I·T

Translating macroscale concepts to microfluidic devices

by

Nicole Hill

A dissertation submitted in partial fulfillment of the requirements
for the degree of Doctorate of Philosophy in Microsystems Engineering

Microsystems Engineering Program
Kate Gleason College of Engineering

Rochester Institute of Technology
Rochester, New York
May 6th, 2021

Translating macroscale concepts to microfluidic devices
by
Nicole Hill

Committee Approval:

We, the undersigned committee members, certify that we have advised and/or supervised the candidate on the work described in this dissertation. We further certify that we have reviewed the dissertation manuscript and approve it in partial fulfillment of the requirements of the degree of Doctor of Philosophy in Microsystems Engineering.

_____

Dr. Blanca Lapizco-Encinas Date
Professor, Biomedical Engineering

_____

Dr. Vinay Abhyankar Date
Assistant Professor, Biomedical Engineering

_____

Dr. Karuna Koppula Date
Senior Lecturer, Chemical Engineering

_____

Dr. Michael Schertzer Date
Associate Professor, Mechanical Engineering

_____

Dr. Moumita Das Date
Associate Professor, Physics and Astronomy

Certified by:

_____

Dr. Stefan Preble Date
Director, Microsystems Engineering Program

ABSTRACT

Kate Gleason College of Engineering
Rochester Institute of Technology

Degree: Doctor of Philosophy **Program**: Microsystems Engineering

Authors Name: Nicole Hill

Advisors Name: Dr. Blanca H. Lapizco-Encinas

Dissertation Title: Translating macroscale concepts to microfluidic devices

Electrokinetics represents an extremely versatile family of techniques that can be used to manipulate particles and fluid in microfluidic devices. This dissertation focused on taking techniques commonly used on a macroscale and developing microscale equivalents utilizing electrokinetics to effectively manipulate and separate microparticles. This analysis focuses on chromatography and separation trains as macroscale techniques translated to microfluidic insulator-based electrokinetic devices. The geometries of insulating post arrays embedded in microchannels were optimized using a combination of mathematical simulations and experimentally derived correction factors. Two particle separations were experimentally demonstrated: a separation based on differences in particle size and a separation based on differences in particle charge. The introduction of nonlinear electrophoresis into the electrokinetics paradigm prompted the creation of an empirical electrokinetic equilibrium condition, an experimentally derived, geometry independent value unique to different particles. This term takes into account particle-particle interactions and the presence of an electric field gradient to help simulate the impact of nonlinear electrophoresis on particle motion and provide an estimate trapping voltages for particles using similar suspending media. Finally, a cascade device design was presented as a type of separation train, built to filter larger contaminants from complex

particle suspensions. Sample purification for a scheme involving manual device transferring of sample versus the cascade device, which required no manual transfer, demonstrated a notably lower sample loss in the cascade device. Bacteriophages were effectively enriched using the cascade scheme, demonstrating the potential use of this technique for purifying valuable biological samples.

ACKNOWLEDGEMENTS

I would like to thank my supervisor, Dr. Blanca H. Lapizco-Encinas, for her invaluable guidance, knowledge, support, and incredible time. Thank you so much for your patience and advice and assistance, and thank you for always including the needs and futures of your students in your plans.

I would also like to thank my Ph.D. Dissertation committee, Dr. Vinay Abhyankar, Dr. Karuna Koppula, and Dr. Michael Schertzer for their wonderful insights and advice, challenging inquests, and precious time.

I would like to thank Mrs. Lisa Zimmerman for her constant support of me and every other student in the Microsystems Engineering Community as well as Dr. Bruce Smith and Dr. Parsian Mohseni for creating a positive and unique degree experience and Dr. Stefan Preble for his assistance with the completion of my degree. Thank you all for creating a wonderful program!

I would like to extend my extreme gratitude to Dr. Julie Thomas, a wonderful researcher and caring and dedicated teacher who donated time and resources and her precious samples to my projects. Your words and insights were truly, truly appreciated and I cannot thank you enough for your constant desire to help.

To the Biomedical Engineering Department, thank you for welcoming me into the department and providing so many small but valuable resources throughout the years.

I need to acknowledge Adriana Coll De Peña and thank her for everything. We started in the laboratory together and I’m extremely grateful for everything we were able to experience together and for your truly amazing work and collaborations and, most importantly, friendship.

Finally, I would like to thank the National Science Foundation for funding my Ph.D. It cannot be understated how important the ability to continue to expand scientific knowledge and understanding is, and thank you for enabling research all across the country in order to do just that (Award CBET-1705895).

LIST OF PUBLICATIONS

1. **Hill, N.**; Coll De Peña, A.; Miller, A.; Lapizco-Encinas, B.H. On the potential of microscale electrokinetic cascade devices, Electrophoresis, Accepted, 2021.
2. Coll De Peña, A.; **Hill, N.**; Lapizco-Encinas, B.H. Determination of the empirical electrokinetic equilibrium condition of microorganisms in microfluidic devices, Biosensors, 10(10) 148, 2020.
3. Coll De Peña, A.; Miller, A.; Lentz, C.J.; **Hill, N.** ; Parthasarathy, A.; Hudson, A. O.; Lapizco-Encinas, B.H.; Creation of an electrokinetic characterization library for the detection and identification of biological cells, Analytical and Bioanalytical Chemistry, 412, 3935-3945, 2020.
4. **Hill, N.** and Lapizco-Encinas, B.H. Continuous flow separation of particles with insulator-based dielectrophoresis chromatography, Analytical and Bioanalytical Chemistry, 412 3891-3902, 2020.
5. Weirauch, L.; Lorenz, M.; **Hill, N.**; Lapizco-Encinas, B.H.; Baune, M.; Pesch, G.; Thöming, J. Material-selective separation of mixed microparticles via insulator-based dielectrophoresis, Biomicrofluidics, 13(6) 064112, 2019.
6. Coll De Peña, A.; Mohd Redzuan, N.H.; Abajorga, M.K; **Hill, N.**; Thomas, J.A.; Lapizco-Encinas, B.H. Analysis of Bacteriophages with Insulator-Based Dielectrophoresis, Micromachines, 10(7) 450, 2019.
7. **Hill, N.** and Lapizco-Encinas, B.H. On the use of correction factors for the mathematical modeling of insulator based dielectrophoretic devices, Electrophoresis, 40 2541-2552, 2019.
8. Polniak, D.; Goodrich, E.; **Hill, N.** ; Lapizco-Encinas, B.H.; Separating large microscale particles by exploiting charge differences with dielectrophoresis, Journal of Chromatography A, 1545:84-92, 2018.

PUBLICATIONS FROM OTHER RESEARCH PROJECTS

9. Huber, C.; Hoitt, M.; Barlow, N.S.; **Hill, N.** ; Keithley, K.; Weinstein, S.J.; On the stability of waves in classically neutral flows, IMA Journal of Applied Mathematics, 85(2) 309-340, 2020.
10. Barlow, N.S.; Stanton, C.R.; **Hill, N.** ; Weinstein, S.J.; Cio, A.G.; On the summation of divergent, truncated, and underspecified power series via asymptotic approximants, The Quarterly Journal of Mechanics and Applied Mathematics, 70(1):21-48, 2017.
11. Gupta, A.; **Hill, N.** ; Valenzuela, P.; Johnson, E.P.; Introducing chemical reactions concepts in K-6 through a hands-on food spherification and spaghetti-fication experiment, JSTEM, 18(1), 2017.

TABLE OF CONTENTS

LIST OF FIGURES

LIST OF TABLES

GLOSSARY AND NOMENCLATURE

Glossary of abbreviated terms	
AC	Alternating current
CE	Capillary electrophoresis
DC	Direct current
DEP	Dielectrophoresis
DI	Deionized
eDEP	Electrode-based dielectrophoresis
EDL	Electrical double layer
E_{EEC}	Electrokinetic equilibrium condition
eE_{EEC}	Empirical electrokinetic equilibrium condition
EK	Electrokinetic(s)
EO	Electroosmosis
EP	Electrophoresis
EP^1	Linear electrophoresis
EP^3	Nonlinear electrophoresis or electrophoresis of the second kind
iDEP	Insulator-based dielectrophoresis
iEK	Insulator-based electrokinetic(s)
nDEP	Negative dielectrophoresis
pDEP	Positive dielectrophoresis
PDMS	Polydimethylsiloxane
sTV	Stable trapping voltage

Nomenclature of variables used			
$\vec{v}_{EP^1}$	Linear electrophoretic velocity	$\vec{v}_{EO}$	Electroosmotic velocity
μ_{EP^1}	Linear electrophoretic mobility	μ_{EO}	Electroomotic mobility
$\vec{v}_{EK}$	Linear electrokinetic velocity	$\vec{v}_{DEP}$	Dielectrophoretic velocity
μ_{EK}	Linear electrokinetic mobility	μ_{DEP}	Dielectrophoretic mobility
$\vec{v}_{EP^3}$	Nonlinear electrophoretic velocity	$\vec{v}_T$	Total particle velocity
μ_{EP^3}	Nonlinear electrophoretic mobility	$\vec{v}_P$	Dielectrophoretic and linear electrokinetic velocity
$\vec{E}$	Electric field	E	Electric field magnitude
ε_M	Media permittivity	η	Viscosity
ζ_P	Zeta potential of the particle	ζ_W	Zeta potential of the wall
f_{CM}	Clausius-Mossotti factor	ε_P^*	Complex permittivity of the particle
ε_M^*	Complex permittivity of the media	ω	Angular frequency
r_P	Particle radius	σ_P	Particle conductivity
σ_M	Media conductivity	c	Correction factor
$\frac{N}{l}$	Number of plates per meter	$t_{r,e}$	Experimentally-derived retention time
LD	Length of the device/post array	W	Peak width
t_R	Simulated retention time	Rs	Resolution
t	t-value	$\bar{x}$	Sample average
s	Sample standard deviation	n	Sample size
ϕ	Electric potential	$\vec{n}$	Vector normal to the surface
$\vec{J}$	Electric current density	$V_{reservoir}$	Electric potential applied to a chosen reservoir

1 INTRODUCTION

1.1 ELECTROKINETICS

Microfluidics as a field is rapidly growing in the modern age with potential applications in several fields including environmental and clinical analyses. Microfluidic devices are fast, efficient, portable, and can be very inexpensive. They require smaller sample sizes than traditional tests, can provide high resolution, high sensitivity results, and can focus, sort, and separate particles [1]–[3]. Another important aspect of microfluidics is the ability to use electrokinetic techniques for fluid and particle manipulation [4]. Electrokinetics (EK) refers to the family of effects generated when an electric field is applied to material exposed to aqueous solutions. Electrokinetic phenomena can be broken into two primary categories: linear EK and nonlinear EK.

Linear EK is comprised of linear electrophoresis (EP^1), or electrophoresis (EP) of the first kind, and electroosmosis (EO). Both of these phenomena depend on the electrical double layer (EDL) and have a linear dependence with the electric field. When microfluidic materials are exposed to aqueous solutions, they acquire a surface charge. The surface charge modifies the distribution of ions in the fluid and form the EDL [5]. Ions of the opposite charge as that of the surface tightly layer the surface, forming the compact, or Stern or Helmholtz, layer. From there, a diffuse, or Gouy-Chapman, layer formed from both types of ions attracted by the strong charges of opposite sign forms around the compact layer. This layer has more freedom to shift than the compact layer. Exposure to an electric field causes the ions in the compact layer to vibrate, which brings about a response in the diffuse layer. If the EDL is associated with the walls of a microchannel, the ion movement in the diffuse layer induces a movement in the solution, leading to EO flow.

The flow profile associated with EO is a nearly flat velocity profile as opposed to the parabolic velocity profile associated with pressure-driven flow, as shown in Figure 1.1.

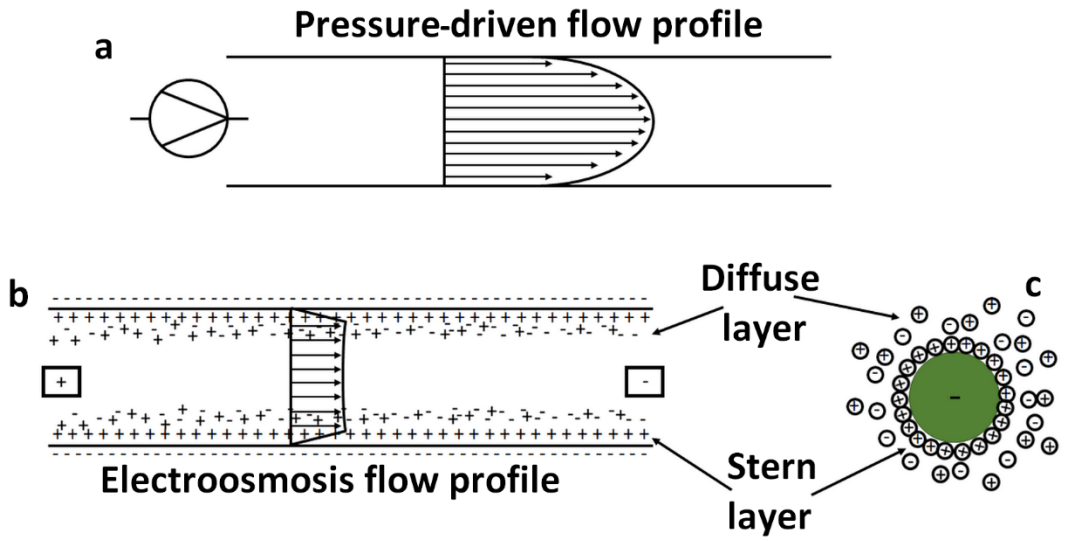

Figure 1.1 Flow profiles for **a** pressure-driven flow in a channel and **b** EO flow in a channel with an EDL. The EDL for the **b** channel and **c** particle are shown and labeled, with the tightly bound ions making up the diffuse layer and the more free-flowing ions making up the stern layer.

The direction and strength of the movement are functions of aqueous solution pH and ionic strength [6]. A charged particle will also acquire an EDL and will move in response to the electric field. The flow profiles for pressure-drive flow and EO flow can be seen in Figure 1.1a and Figure 1.1b, respectively. The EDL of the channel and the particle can be seen in Figure 1.1b and Figure 1.1c, respectively. The movement of the particle due to the EDL is EP^1, and depends on the solution properties as well as the charge-to-mass ratio of the particle [7]. The use of EO means that microfluidic systems, taking advantages of electric fields, can operate without the need of hydrodynamic pumps to induce motion and only need an applied electric potential. This technique is only applicable on the microscale as it requires a very high surface area to volume ratio.

Nonlinear EK effects of concern for this work include dielectrophoresis (DEP) and nonlinear electrophoresis (EP^3), or electrophoresis of the second kind. DEP is a

phenomenon that first surfaced in 1951 [8], utilizing electrodes to generate the electric fields in a technique eventually termed electrode-based DEP (eDEP). The technique relies upon the generation of an electric field gradient between regions of high electric fields and low electric fields. When particles enter this gradient, they polarize, inducing particle movement towards areas of higher electric fields (positive DEP or pDEP) or lower electric fields (negative DEP, or nDEP). One of the benefits of DEP is that is works on all particle types, including uncharged particles that are not influenced by EP. While eDEP has been used in a wide variety of particle separations and manipulations [9]–[15], there are some problems associated with the technique. Electrodes can be expensive, structures can be one-dimensional, fabrication can be difficult, and biofouling is a real issue [16]. While some of these hurdles have been overcome lately with newer materials and techniques, there is also an alternate mode of DEP, insulator-based DEP (iDEP).

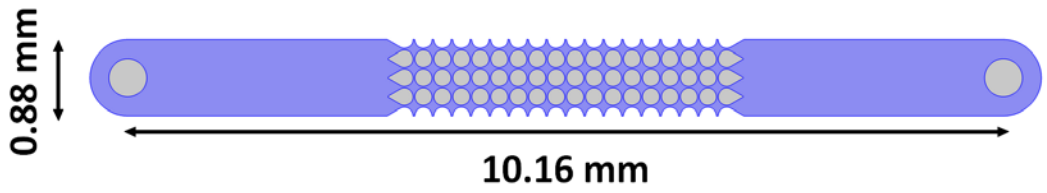

Figure 1.2 Example of the top-down view of an iEK (formerly iDEP) channel. The gray areas indicate insulating posts within the channel and reservoirs for the channel at either end.

Initially discovered in 1989 as a byproduct of a cell fusion technique [17], iDEP was revived into the research sphere in 2000 by Cummings [18]. An example of a device with circle-shaped insulating posts used by our group is shown in Figure 1.2. The technique is still applicable even if biofouling becomes an issue and devices can be repeatedly manufactured from one mold using a basic polymeric material like polydimethylsiloxane (PDMS) [19]. While several different studies have exhibited the utility of iDEP for sorting, separating, concentrating, and characterization for different bioparticles of interest such as

cells [20]–[23], viruses [24]–[26], proteins [27]–[31], organelles [32]–[34], and DNA [35], [36], recent studies have suggested that DEP is not the only nonlinear EK effect that influences cell movement [37]–[41]. Instead, another attribute, EP^3, may be responsible for the particle behavior. At higher electric fields, ion convection leads to concentration polarization in the spaces around particles and the creation of another ion layer outside of the EDL, known as the space charge [42]. This space charge leads to an enhanced electrophoretic force, EP^3, that acts on the particle in the same direction as EP^1 but instead depends on the cube of the electric field [43], [44]. This effect depends on having a high enough current to induce the polarization effect in the particle and is induced by the field itself and not the particle, though it is still a property of the particle as it relies on the initial particle charge. While EP^3 has been observed in mathematics and physics research for a while, the connection to insulator-based microfluidic systems was only recently realized. Trapping and flow reversal of microparticles under an applied DC voltage was observed in a channel without any insulators or electrodes that could create an electric field gradient, meaning that DEP could not be responsible [37]. The postless channel and the particle behavior at increasing electric fields in shown in Figure 1.3.

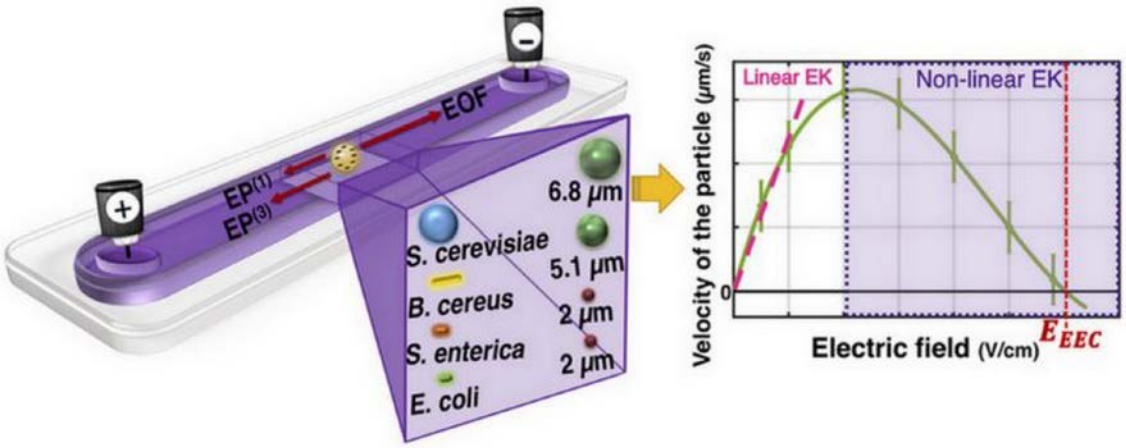

Figure 1.3 Postless iEK channel and particle velocity versus electric field graph for particles subject to linear and nonlinear electrokinetics. Reprinted with permission from [41]. Copyright (2020) American Chemical Society.

Further experiments have suggested that the effect of DEP is negligible compared to EP^3 [39], accounting for very little influence on the velocity terms. EP^3 is still being developed and is a very new concept within the iDEP research fields, but the term insulator-based EK or iEK is now being applied by our group to reflect this paradigm shift.

While iEK devices no longer see DEP as the only nonlinearity at higher electric fields, it is worth it to consider the importance of insulating post and channel geometry. Insulating posts create both an electric field gradient and areas of higher electric fields. These areas result in spaces where, as particles approach, a much higher current exists that can induce the space charge and create EP^3 effects even at lower channel-wide electric fields. These areas of higher electric field lead to a repulsion similar to that attributed to DEP.

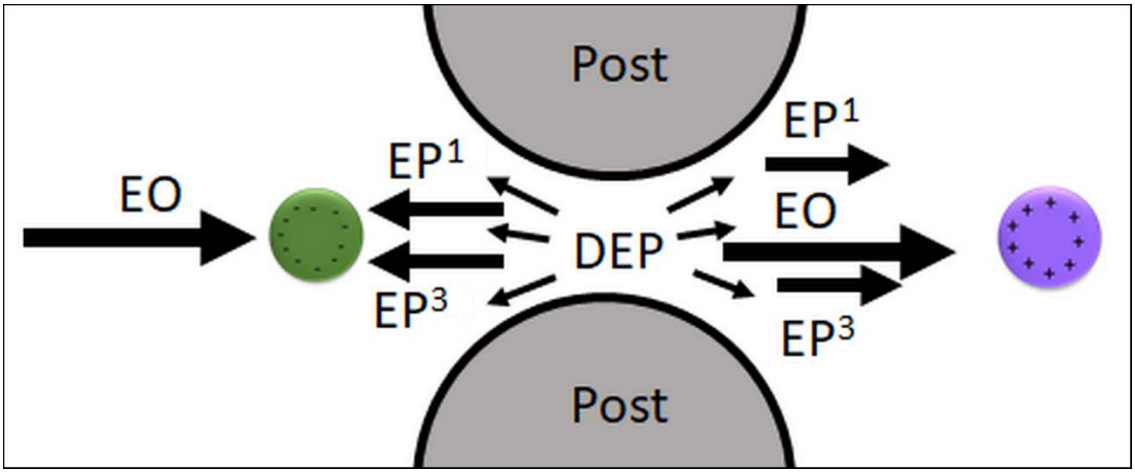

Figure 1.4 Representation of the forces acting on a positive particle (purple) and a negative particle (green) in an iEK device.

Figure 1.4 demonstrates the movement of particles in an iEK device similar to that in Figure 1.2. The EP^1 and EP^3 forces left of the post array represent forces applied to negative particles throughout the system while the EP^1 and EP^3 forces right of the post array represent forces applied to positive particles throughout the system. DEP force for both positive and negative particles will behave the same assuming the particles experience nDEP, as all particles in this work do. For negative particles, the combination of the nonlinear EK effects and EP^1 repulse EO and lead to particle trapping around the insulating posts, where distorted electric field lines lead to an electric field gradient and a higher electric field than in the channel as a whole. For positive particles, only DEP counters the linear EK and EP^3 forces, making it unlikely that the particles will trap in systems involving DEP and impossible for particles to trap in systems without insulators to distort the field and create a DEP force that might be used to mitigate particle motion. This assumes the use of a media that yields upstream EO motion, though for the media used in our group, this is a valid assumption.

1.2 CHROMATOGRAPHIC AND MULTI-TIER SEPARATIONS IN MICROFLUIDIC DEVICES

Two sections of this work, implementation of chromatography concepts on microfluidic electrokinetic devices and electrokinetic cascade devices for sample filtration and separation, involve well-known macroscale concepts, chromatography and separation trains. These concepts and associated innovations in the microfluidic field will be discussed below.

Chromatography is a well-tested analytical technique that has long been recognized for its ability to act as a streaming particle separation and analysis technique [45]. The technique works by relying on differences in affinity of analytes toward the stationary phase of the chromatographic channel while the mobile phase is responsible for moving the analytes through the system. Capillary electrophoresis (CE), another technique that is similar but not identical to chromatography, capitalizes on the EP^1 mobilities of the analytes to separate or analyze the analytes [7]. Capillary electrochromatography is a hybrid of traditional liquid chromatography and CE [46] and is applied to submicron particles, much like CE and liquid chromatography. Streaming EK separations in microchannel with arrays of insulating posts present the possibility to act in a similar fashion as chromatography, with insulating post arrays working in conjunction with EK to facilitate particle separation. Post geometries can be used to tune systems to particular separation types (such as separations by particle electrical charge or particle size) or observe ideal post geometries for EK streaming with a DC voltage application.

While there is a common technique called deterministic lateral displacement that is a streaming separation, this technique largely involves AC fields, the introduction of sheath

flow, or both to fully work [47]–[50]. Deterministic lateral displacement involves offset posts to direct stream flow as it moves through the system. There are no reports of streaming iDEP separations, though there are reports of streaming DEP separations. The first such report came from the Washizu group in 1994 [51] and relied on an eDEP system where interdigitated electrodes selectively trapped biomolecules by size as EO prompted fluid movement through the system. Another group, Holmes and Morgan, took advantage of electrodes to facilitate separation, first focusing the incoming cell stream with planar electrodes on the top and bottom of the channel before subjecting cells to a secondary electrode on the bottom of the channel utilizing pDEP to pull components from the stream into different trajectories [52]. The Hakoda group published some results utilizing first eDEP [53] and then insulating glass beads for iDEP [54], but no separation was reported for the iDEP results to allow for insight into the applicability of the technique. A very recent report exploits eDEP and hydrodynamic flow to separate particles into streams based on polarizability [55]. No other technique, though, combines iEK streaming separations along a chromatographic-like channel and provides information on separation.

EK is capable of effectively separating particle mixtures, but not all mixtures have the same properties. When considering medical or environmental point-of-care testing, effective analysis despite the presence of unwanted components of the system is important. A simple solution lies in the macroscale world of separation trains. When separations between multiple components prove more difficult than can be effectively handled within one separation system, multiple systems are linked in order to facilitate separation, allowing components to leave the system at different times [56] and optimizing separation processes. The same concept can be applied on a microscale; multiple post arrays can be

linked together with geometries modified to suit specific needs in order to facilitate an improved separation. The device can act as a filtration mechanism for some solutions that contain components of no interest to the final product or analyte. One good example of this is in the purification of a bacteriophage cocktail. Bacteriophages are a type of virus that specifically attacks bacteria and have been explored as an alternative to traditional pharmaceutical antibiotics to help combat drug resistance. However, in order for the bacteriophages to replicate, they must be in a bacterial solution and media that facilitates bacterial growth. Samples can be purified by centrifugation, but it is very difficult to purify the solution completely, especially without incurring massive sample loss [24]. Viruses are on the order of hundreds of nanometers or less and larger micro-sized cell debris can easily clog a DEP system, limiting the ability to separate bacteriophages in these partially purified solutions. A multi-tiered separation scheme could be applied to help filter out the undesirable components of a mixture, facilitating downstream sample characterization and processing. A couple of examples of multi-tiered systems already exist in the microfluidic space, but there are some key differences between the system discussed here and previous models. Yang et al. [57] generated a cell sorting system that relies on eDEP. The cascade design they describe has a single electrode that manipulates the location of the target cell, meaning all parts of the system are subjected to the same signal. Gallo-Villanueva et al. [58] proposed a design that works to selectively position particles at different times. A more recent example of this device was used to separate exosome nanoparticles by size through the modification of the vertical distance between the posts within the first post array and the second post array [59]. The system as a whole is subjected to a single electric field. Additionally, these designs can be problematic if clogging is a significant issue for

the system. A multi-tiered system with independent electric fields enables greater control throughout the design and offers more potential.

1.3 OBJECTIVES

This work explores the application of macroscale concepts on microfluidic devices as well as the application of new parameters for bioparticle identification and simulation usage. This is broken into three sections, (i) implementation of chromatography concepts on microfluidic electrokinetic devices, (ii) empirical electrokinetic equilibrium condition, and (iii) electrokinetic cascade devices for sample filtration and separation.

For implementation of chromatography concepts on microfluidic electrokinetic devices, the goal is to explore the potential of chromatographic microfluidic channels to separate plugs of particles into fractions through small differences in their affinities towards insulating posts that add up as particles traverse the channel. This streaming separation technique, can help increase cell viability with smaller electric fields [60] and separate particle streams instead of relying on trapping particles. Particular goals of interest are optimizing the geometries of the post for streaming separations by charge and size.

The empirical electrokinetic equilibrium condition is a new parameter that can be used in simulations to assess application voltage estimations for particles of interest. This parameter is of particular note as it involves the shift from the traditional belief that DEP is the primary nonlinear EK forces in EK microfluidic channels with electric field gradients to the new understanding that EP^3 and DEP both play a role in these channels and influence particle motion. It is primarily presented as a relatively easy method to find value for a good estimation on particle behavior at a given voltage and is contrasted with the

electrokinetic equilibrium condition, another new parameter with much more strenuous calculation requirements which will be described later.

The electrokinetic cascade devices for sample filtration and separation is a multi-tier separation scheme built to filter samples to allow for more complex separation or analysis further along in the process. One of the primary motivating factors behind this objective is the purification of valuable samples like bacteriophages which, by necessity, have to be grown in bacteria in order to replicate and spread. With initial experimental tuning, this technique could be a method that does not require any labeling to filter out samples and concentrate analytes of interest before collection, making it a powerful alternative to techniques that might yield greater sample loss, like centrifugation, in the interest of purity.

2 THEORETICAL BACKGROUND

2.1 LINEAR ELECTROKINETICS

Linear EK, as mentioned above, is made up of EP[1], which corresponds to the impact of the electric field on particle motion, and EO, which corresponds to the impact of the electric field on fluid motion. The relevant velocities of these two forces can be defined by the Helmholtz-Smoluchowski equation [61]:

$$\vec{v}_{EP^1} = \mu_{EP^1}\vec{E} = \frac{\varepsilon_M \zeta_P}{\eta}\vec{E} \tag{2.1}$$

$$\vec{v}_{EO} = \mu_{EO}\vec{E} = -\frac{\varepsilon_M \zeta_W}{\eta}\vec{E} \tag{2.2}$$

where μ_{EP^1} and μ_{EO} represent the EP[1] and EO mobilities, respectively. The mobilities are defined by the media permittivity and media viscosity, ε_M and η, respectively. The EP[1] mobility is defined by ζ_P, the zeta potential of the particle, and the EO mobility is defined by ζ_W, the zeta potential of the channel walls.

The combination of both EP[1] and EO can be described as follows:

$$\vec{v}_{EK} = \mu_{EK}\vec{E} = -\frac{\varepsilon_M(\zeta_W - \zeta_P)}{\eta}\vec{E} \tag{2.3}$$

where μ_{EK} is the EK mobility. For the purposes of clarity, $\vec{v}_{EK}$ will be used to represent the linear EK equations as a unit. The material used for all channels in this work is PDMS, which has a negative surface charge and a negative zeta potential for the medias used in these experiments. All fluid motion under a DC electric potential is directed from the positive electrode to the negative electrode, indicated by a positive velocity. All particles in this work have negative zeta potentials, as do bioparticles in general. These particles will experience an EP[1] force directing particles from the negative electrode to the positive electrode under a DC electric potential. This means the EO velocity and the EP[1]

velocity will always be in opposite directions for the situations described in this work. If $(\zeta_W - \zeta_P) > 0$, then $\vec{v}_{EK}$ will be oriented toward the positive electrode. If $(\zeta_W - \zeta_P) < 0$, then $\vec{v}_{EK}$ is oriented towards the negative electrode.

2.2 NONLINEAR ELECTROKINETICS AND EQUILIBRIUM ELECTROKINETIC CONDITION

The nonlinear EK equations do not depend linearly on the electric field. For DEP, the velocity depends on the electric field gradient. For a DC electric potential applied to a spherical particle, the DEP velocity is [62], [63]:

$$\vec{v}_{DEP} = \mu_{DEP} \nabla(\vec{E} \cdot \vec{E}) = \frac{r_P^2 \varepsilon_M}{3\eta} \mathrm{Re}[f_{CM}] \nabla(\vec{E} \cdot \vec{E}) \tag{2.4}$$

where μ_{DEP} is the DEP mobility, r_P is the radius of the particle, and $\mathrm{Re}[f_{CM}]$ is the real part of the Clausius-Mossotti (CM) factor. The CM factor is defined as [64]:

$$f_{CM} = \frac{\varepsilon_P^* - \varepsilon_M^*}{\varepsilon_P^* + 2\varepsilon_M^*} \tag{2.5}$$

where ε_P^* is the complex permittivity of the particle and ε_M^* is the complex permittivity of the media. The complex permittivity in general is defined as:

$$\varepsilon^* = \varepsilon - i\frac{\sigma}{\omega} \tag{2.6}$$

where i is the imaginary vector, ω is the angular frequency of the applied potential, and σ is the conductivity. For low frequency or DC potentials, this can be simplified to:

$$\lim_{\omega \to 0} f_{CM} = \frac{\sigma_P - \sigma_M}{\sigma_P + 2\sigma_M} \tag{2.7}$$

As the particles used in this work all exhibit nDEP, it can be said that the conductivity of the particles is less than that of the media. The assumption used for

models is that the conductivity of the particles is much less than that of the media, bringing the value to the lower limit for the CM factor, -0.5.

In several works, the need for a correction factor applied as a multiplier to the DEP term in an equation has been used to help match simulations to experimental results [65]. Specifically for the purposes of the section 'Implementation of Chromatography Concepts on Microfluidic Electrokinetic Devices,' a total particle velocity equation involving this correction factor will be shown. The work in this section was performed before EP^3 was understood and so uses this equation for much of its simulation work:

$$\vec{v}_P = \vec{v}_{EK} + c\vec{v}_{DEP} \tag{2.8}$$

where $\vec{v}_P$ is the total particle velocity and c is the correction factor. The correction factor is set to 1 for standard simulations without correction factor.

For the nonlinear EP term, EP^3, the velocity can be defined as [37], [39]–[41]:

$$\vec{v}_{EP^3} = \mu_{EP^3}(\vec{E} \cdot \vec{E})\vec{E} \tag{2.9}$$

where $\vec{v}_{EP^3}$ is the EP^3 velocity and μ_{EP^3} is the EP^3 mobility. The EP^3 mobility is found experimentally.

For particles in a system without insulators posts or any other source of electric field gradient, the total particle velocity, $\vec{v}_T$, can be defined as:

$$\vec{v}_T = \mu_{EP^3}\left(\vec{E} \cdot \vec{E}\right)\vec{E} + \mu_{EP^1}\vec{E} + \mu_{EO}\vec{E} \tag{2.10}$$

For particles that are trapping, the total particle velocity would be 0, making the equation:

$$0 = \mu_{EP^3}\left(\vec{E} \cdot \vec{E}\right)\vec{E} + (\mu_{EP^1} + \mu_{EO})\vec{E} \tag{2.11}$$

Solving for the electric field, the final equation becomes:

$$E = \sqrt{-\frac{(\mu_{EP^1} + \mu_{EO})}{\mu_{EP^3}}} \tag{2.12}$$

where the electric field is the electrokinetic equilibrium condition (E_{EEC}) in this context. This equation can be used to determine μ_{EP^3}. To address the negative sign, if the particle has a positive charge, μ_{EP^1} and μ_{EP^3} will both be positive. In this case, if $\mu_{EO}$is positive, as is the case in all our experiments, then the term as a whole is imaginary, which would make sense as there would be no way to trap the particle. If μ_{EO} is negative and less than μ_{EP^1}, it could not lead to particle trapping. If μ_{EO} is negative and greater than μ_{EP^1}, particle trapping is possible. If the particle has a negative charge, as in the case with all particles used in this work, both μ_{EP^1} and μ_{EP^3} will be negative. If μ_{EO} is negative, the particle will not trap (same idea as all positive values) as there is no opposing force. If μ_{EO} is positive and less than μ_{EP^1}, the particle can never trap. If μ_{EO} is positive and greater than μ_{EP^1}, which should be the case for all experiments presented here, then a real value for the E_{EEC} exists.

2.3 CHROMATOGRAPHIC AND STATISTICAL EQUATIONS

Chromatography has several different separation modes. There are certain equations that are used to bridge these modes and other separation techniques so their progress and success can be effectively compared against one another. The first of these equations defines separation efficiency, a key to comparing different separation techniques:

$$\frac{N}{l} = \frac{16\, t_{R,e}^2}{LD * W^2} \tag{2.13}$$

where N/l refers to the number of theoretical plates per meter, LD is the length of the device, W is the width of the detection curve for the particle, and $t_{R,e}$ refers to the retention time, specifically the experimentally obtained retention time in this work. Retention time used for simulations can be calculated using the following equation:

$$t_R = \frac{LD}{v_P} \tag{2.14}$$

where v_P is the simulated total particle velocity magnitude (Eq. (2.8)). The experimentally derived retention time, $t_{R,e}$, is the peak, or maximum, time for the detection curve.

Another important equation is the resolution equation, built to determine whether two peaks can be considered separated. The equation for resolution is:

$$Rs = \frac{2(t_{R,e2} - t_{R,e1})}{W_1 + W_2} \tag{2.15}$$

where Rs is the resolution, and the subscripts of 1 and 2 refer to the specific peak of interest. Rs is the difference between experimental retention times (peaks of the detection curve) divided by the total width of both curves. For two curves to be considered fully separated, Rs must be at least 1.5.

In order to make statistical comparisons, the following equation for a t-value was used:

$$t = \frac{(\bar{x}_1 - \bar{x}_2)}{\sqrt{\frac{s_1^2}{n_1} + \frac{s_2^2}{n_2}}} \tag{2.16}$$

where $\bar{x}$, s, and n represent the sample average, standard deviation, and size, respectively. The significance level used for these analyses was 0.05.

3 MATERIALS AND METHODS

3.1 FABRICATION

Device fabrication relies on negative replica molding using a patterned silicon wafer. Clean silicon wafers with a 4 inch diameter are coated in SU8 3050 photoresist (MicroChem, Newton, MA) and spun to form a 40 μm thick layer. A transparency mask (Output City, Bandon, OR) with a resolution of 25,000 dpi (Fig. 3.1) was placed on the spun wafer and exposed to ultraviolet radiation. As SU8 3050 is a negative photoresist, the areas exposed to ultraviolet radiation experienced a crosslinking reaction and remained on the wafer after development.

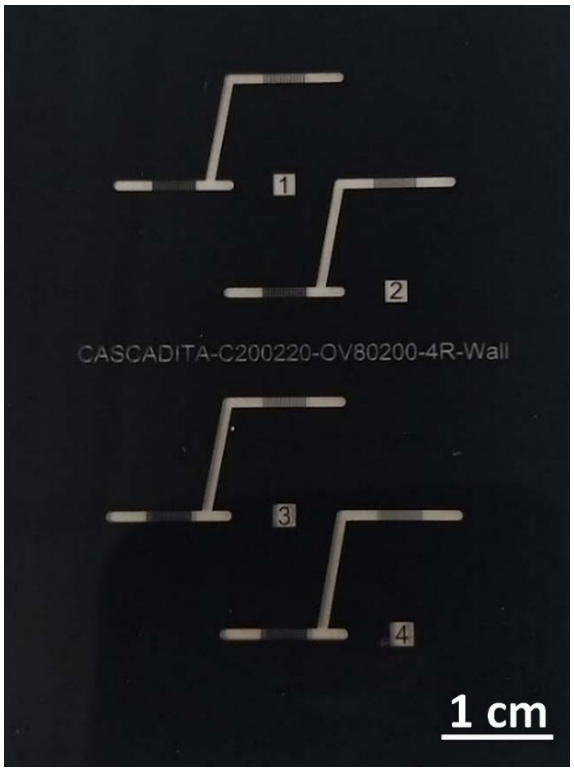

Figure 3.1 High resolution transparency mask used to pattern the SU8 3050 photoresist.

The final mold (Fig. 3.2a) has channel walls and holes where the insulating posts of the device will be. PDMS (Dow Corning, Midland, MI) is cast onto the mold and heated at 85°C for 40 minutes and 135°C for 5 minutes, resulting in a PDMS slab (Fig.

3.2b). The slab is cleaned and sealed to a glass substrate coated in a thin layer of PDMS using a plasma corona wand (Electro Technic Products, Chicago, IL). This allows all inner walls of the device channels to be made from the same PDMS material with the same zeta potential.

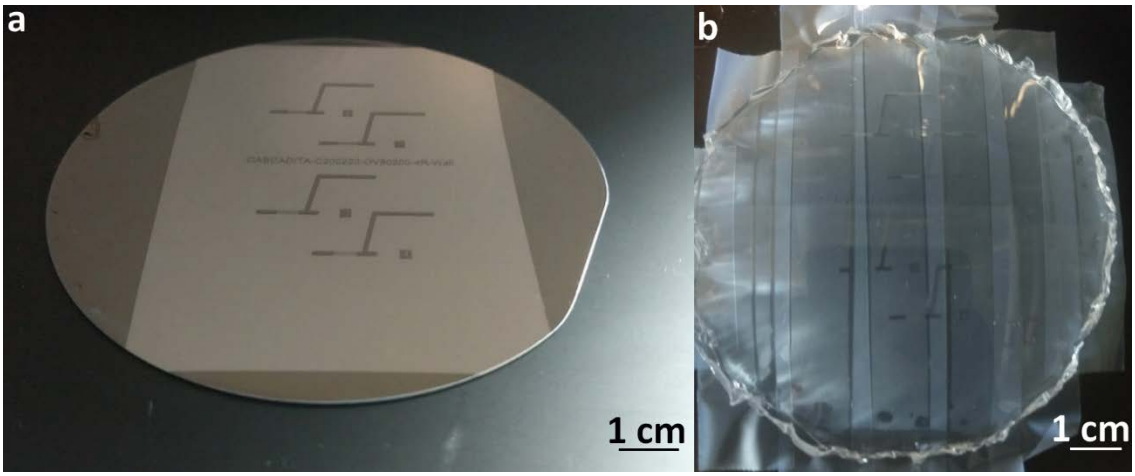

Figure 3.2 Images of the different stages of the device-making process. **a** Silicon mold used as the master for the PDMS device. **b** PDMS device slab covered with tape to remove particulates after removal from the mold.

Devices used for each individual objective and the relevant post dimensions are specified in the relevant sections.

3.2 POLYSTYRENE PARTICLES

Fluorescent polystyrene particles from two different manufacturers, Invitrogen (Eugene, OR) and Magsphere (Pasadena, CA), which fluoresce yellow-green (ex/em 505/515 nm) or red (ex/em 580/605 nm) were employed for experimentation. Stock suspensions were sonicated for at least 10 minutes to break aggregates. Particle concentrations ranged from $7.2 \cdot 10^4$-$1.8 \cdot 10^9$ #/mL. Specific particle details are provided in each relevant section.

3.3 BIOLOGICAL PARTICLES

Three distinct bacterial species and four distinct bacteriophage species were used throughout the work. The specific data for each species will be given in the relevant sections. All bacterial species were plated in lab and cultured in either Lysogeny broth liquid media at 37°C or tryptic soy broth at 30°C, as appropriate, on a shaking incubator. Cells were then spun down twice, fluorescently labeled (or dyed) using one of two nucleic acid stains, either Syto 11 or Syto 40 (Invitrogen, Carlsbad, CA) and resuspended in sterile DI water. Cell concentration was a minimum of 10^6 #/mL. All bacteriophage species were obtained from Dr. Julie Thomas with titers between $1 \cdot 10^{10}$-$1 \cdot 10^{12}$ plaque-forming units/mL (pfu/mL) and stored in SM buffer before usage at which point they were spun down twice, dyed using one of three nucleic acid stains, either Syto 11, Syto 40, or Syto 85, and resuspended in DI water or DI water with 10% w/v glucose.

3.4 SUSPENDING MEDIA

Media used in the experiments for the section Implementation of Chromatography Concepts on Microfluidic Electrokinetic Devices was filtered deionized water with Tween 20 (0.05% v/v) to prevent cell adhesion to the PDMS surface with 0.1 M KOH and 0.1 M KCl used to adjust medium conductivity to 15-25 µS/cm and pH to 6.0-6.5. This media generated an approximate ζ_W = -97.3 mV in PDMS devices. This same suspending media was used for the polystyrene particle experiments for the section Electrokinetic Cascade Devices for Sample Filtration and Separation.

For the experiments analyzed in the section Empirical Electrokinetic Equilibrium Condition, the suspending media was DI water with a conductivity of 15.1 ± 6.1 µS/cm and a pH of 6.7 ± 0.5.

For the experiments with the bacteriophages in the section Electrokinetic Cascade Devices for Sample Filtration and Separation, the suspending media was DI water with 10% w/v anhydrous d-glucose with a conductivity of 11.9 ± 0.7 μS/cm and a pH of 6.7 ± 0.2.

3.5 EQUIPMENT AND SOFTWARE

Two different high voltage sequencers (Model HVS3000VD and Model HVS6000D, LabSmith, Livermore, CA) were used to apply the DC electric potentials for the studies in this work. Platinum wire electrodes (0.584 mm diameter, LabSmith, Livermore, CA) were used to transfer the voltage to the channels through the media. The voltage sequence was programmed and controlled via the Sequence software provided by the manufacturer. Images and videos for the experiments were captured with an Axiovert 40 CFL microscope (Carl Zeiss Microscopy, Thornwood, NY) equipped with an Infinity 2 camera (Luminera, Ottawa, Canada) and a Leica DMi8 inverted microscope (Wetzlar, Germany) paired with a Leica DFC7000 T camera and the LASX software provided by the manufacturer. COMSOL Multiphysics® 4.4 was used to run simulations and ImageJ (National Institute of Health) was used for analysis of experimental videos and images.

3.6 EXPERIMENTAL PROCEDURE

For the experiments associated with the Implementation of Chromatography Concepts on Microfluidic Electrokinetic Devices section, experiments were performed by placing pipette tips in the reservoirs to act as liquid reserves and hold the electrodes in place. Samples of 1-5 μL were injected into the channel for correction factor experiments; for separation experiments, 5-20 μL of particle mixtures were injected.

For the experiments associated with the Empirical Electrokinetic Equilibrium Condition section, 5-25 μL of the relevant microorganism were introduced into the channel at the inlet reservoir. Microorganisms were not sonicated before introduction but were instead shaken or very briefly vortexed.

4 IMPLEMENTATION OF CHROMATOGRAPHY CONCEPTS ON MICROFLUIDIC ELECTROKINETIC DEVICES

4.1 MOTIVATION

Chromatography relies on a simple combination of ideas: a mobile phase containing the analytes that moves through the system and a stationary phase that separates the particles by affinity as they move through the system. These phases take many different forms depending on the system employed for the chromatographic separation, but the primary idea of an affinity-based separation remains throughout the different forms. For EK devices, separation is based on particle trapping or redirection of the flow of particles for a streaming separation. While particle trapping is a convenient technique, concerns about cell viability in high voltage systems that lead to trapping could be mitigated through a type of streaming technique. An EK chromatography technique would represent a different type of streaming separation where a discrete particle plug is put through a long array of posts. The EO flow, representing the mobile phase of the system, pushes particles through the post array while the posts themselves represent the stationary phase. As particles move through the system, the manipulation of the electric field by the insulating posts impacts the motion of the particles moving through the system. The constrictions between insulating posts create areas of high electric fields, and these areas bring about higher intensity linear and nonlinear EK effects. These in turn lead to changes in particle motion depending on the properties of the particles.

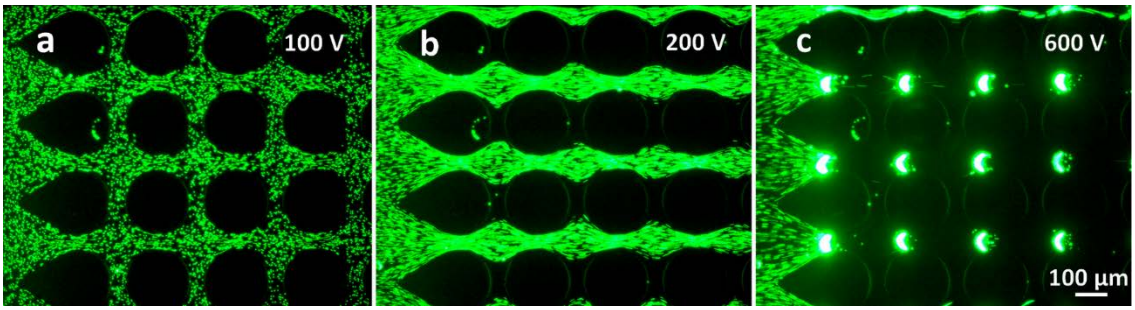

Figure 4.1 Regimes in iEK systems. **a** Linear EK regime where particles move through the device but nonlinear EK effects are not significant enough to impact particle motion. **b** Streaming regime where both linear and nonlinear EK effects are present. **c** Trapping regime where nonlinear EK effects overtake linear EK effects and particle motion is stopped where the electric field and the electric field gradient are high enough. Reprinted with permission from [65]. Copyright (2019) John Wiley and Sons.

In iEK, there are three primary regimes: linear EK (Fig. 4.1a), where voltages are too low for nonlinearities to impact particle motion through the system; streaming (Fig. 4.1b), where both linear and nonlinear EK effects are of similar magnitudes; and trapping (Fig. 4.1c), where nonlinear EK effects overtake linear EK effects and particles motion is halted in regions with particularly high electric fields and electric field gradients [66]. This technique relies on the streaming regime, where particles are still moving through the system and nonlinear EK effects are strong enough to manipulate particle motion. The goal is to be able to use longer insulator post arrays to exaggerate small differences in particle motion in order to yield particle separation. Twelve different geometries were tested in this project. Figure 4.2a shows the device schematic for the chromatography channel used in initial experimentation. Figures 4.2b-4.2m show the twelve different post geometries. While this is not a completely inclusive breakdown, it does cover a variety of different options that can be reviewed: the pointiness of the shape, symmetry versus asymmetry, short side versus long side for the asymmetric posts, the length of the post, and separations between posts.

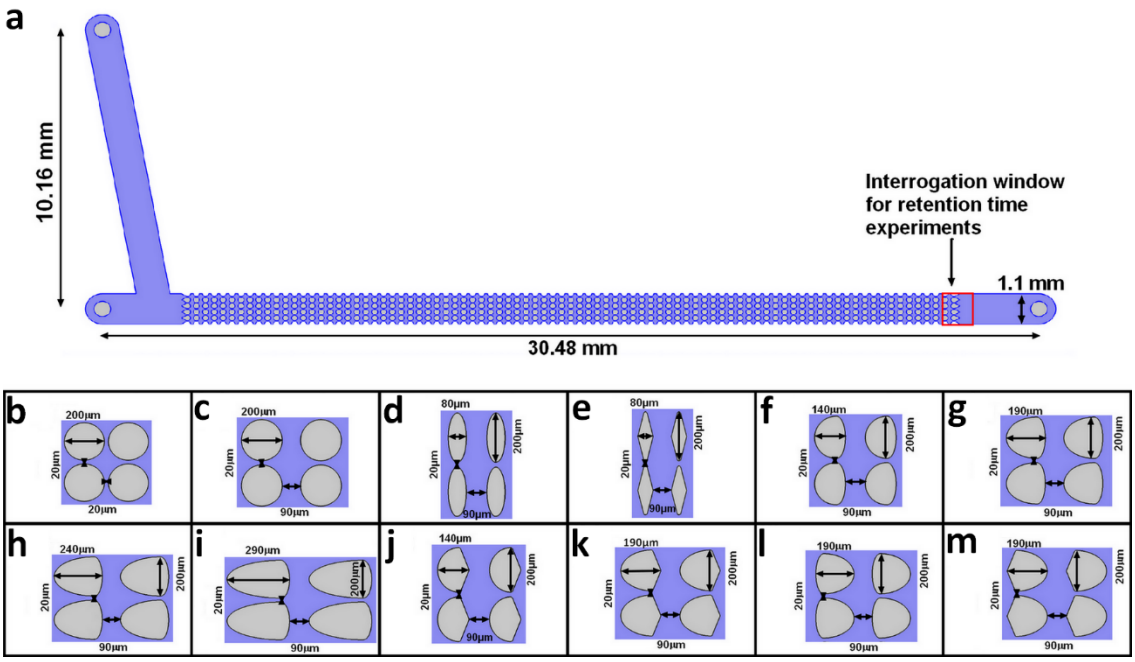

Figure 4.2 Chromatography channel and the post geometries tested in the chromatography project. **a** Overall channel design used for the correction factor experiments. While the shape of the channel varies for the separation experiments to allow for the creation of a sample plug, the post array is always kept consistent and is equidistant from the outlets on the same vertical plane. The insulating post designs are as follows: **b** Circle-200 HS-220 design, **c** Circle-200 HS-90, **d** Oval-200-80, **e** Diamond-200-80, **f** Oval-100-Oval-40, **g** Oval-150-Oval-40, **h** Oval-200-Oval-40, **i** Oval-250-Oval-40, **j** Oval-100-Diamond-40, **k** Oval-150-Diamond-40, **l** Oval-40-Oval-150, and **m** Diamond-40-Oval-150. Reprinted with permission from [67]. Copyright (2020) Springer Nature.

The goal of this project was to find post geometries that optimized the differences in retention times between different particles. Retention time is considered as the amount of time it takes for the analyte of interest to move through the chromatographic channel, in the case of this project the post array. As higher differences in retention time should lead to a better separation, retention time difference is the parameter of interest to assess the best option for post geometry.

This project was initially completed before the second nonlinear effect, EP^3, was acknowledged in EK microfluidics as influencing the systems used in our laboratory. The simulations involved in this project all involve DEP and do not involve EP^3. The initial voltage range determination and geometry optimization process relied on several

simulations that utilized DEP and only EP^1. The correction factors were then calculated to help modify the results and further reinforce the results of the geometry optimization. Correction factors have long been associated with DEP systems to explain the differences in simulation predictions and experimental results [65]. It is now believed that EP^3 bears most of the responsibility for the gap between simulations and experimental results.

4.2 DETERMINATION OF VOLTAGES FOR STREAMING REGIME

The first goal was to attempt to identify an ideal range for voltages that would elicit streaming behavior. While twelve different geometries were tested in the project, initial testing used a symmetric circle geometry (Fig. 4.2c) and an asymmetric oval geometry (Fig. 4.2g) to assess the behavior of a negatively charged particle traveling through the system.

In Figure 4.3, 10 μm particles, the largest used in the study, were used as a representative particle for the velocity profiles. These particle properties were chosen specifically because, as a general trend, the larger the particle, the smaller the correction factor for the particle [65]. The goal was to try and match, as best as possible, the initial simulations to realistic experimental conditions. In using the larger particle, this is most realizable. Figure 4.3 shows the velocity profile lines for particle velocity, EK velocity, and DEP velocity for two different designs, Circle-200 HS-90 and Oval-150-Oval-40. The goal of using symmetric and asymmetric designs is to see how the different velocity trends are impacted.

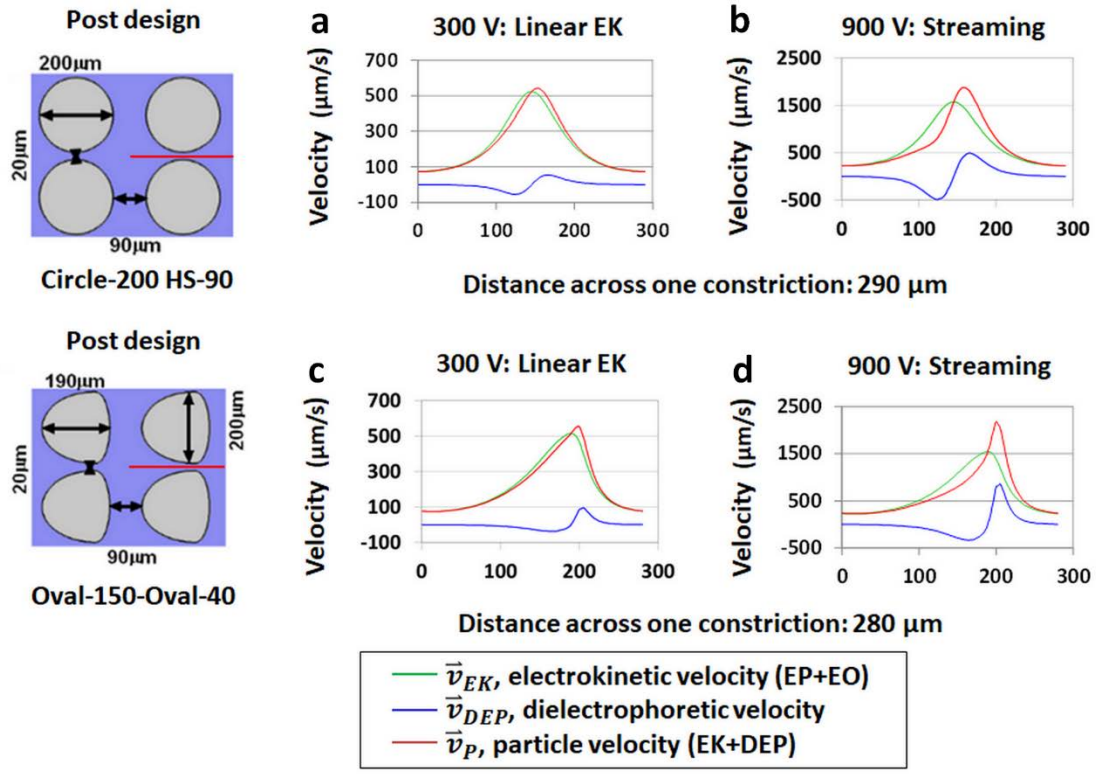

Figure 4.3 Prediction of velocity profiles for 10 µm red Invitrogen carboxylated particles (ζ_P=-72.6 mV) across a single constriction of a symmetric and asymmetric design. **a** Velocity profile for the Circle-200 HS-90 design at 300 V. Note that the particle velocity line (red) and the EK velocity line (green) are nearly identical, indicating a negligible influence of the nonlinear effect of DEP. **b** Velocity profile for the Circle-200 HS-90 design at 900 V. Note that in this case, the particle velocity line (red) is a noticeably different shape from the EK velocity line (green) and more closely matches the shape of the DEP velocity line (blue). **c** Velocity profile for the Oval-150-Oval-40 design at 300 V. Note a similar trend to that exhibited in part **a** of the figure. **d** Velocity profile for the Oval-150-Oval-40 design at 900 V. As in part **b** of the figure, the particle velocity line (red) shape more closely matches the DEP velocity line (blue). Reprinted with permission from [67]. Copyright (2020) Springer Nature.

For each of the velocity profiles, similar trends are apparent. Figure 4.3a shows the symmetric Circle-200 HS-90 design velocity profiles at 300 V. For the EK velocity (green), the particle accelerates as it moves into the constriction. This is supported by both the increasing electric field the particle experiences as the electric field lines are pinched between the insulating posts and the increased velocity due to conservation of mass caused by the constricted region of flow. As the particle leaves the constriction, the velocity decreases by the same logic. For the particle velocity (red), the trend is very similar but

with a very slight shift to the left due to the effects of the DEP velocity (blue). This shift is minimal and results only in a very slight shape deviation and a slightly higher maximum than the EK velocity profile. The DEP velocity looks fairly flat and deviates only slightly above and below zero. As the particles approach the constriction and areas with a high electric field gradient, DEP repels the particles in the opposite direction, downstream or toward the inlet, indicated by the negative velocity. As the particle moves through the constriction and out the other side, it is pushed upstream or toward the outlet instead, repelled by the high electric field gradient.

Figure 4.3b shows the same symmetric Circle-200 HS-90 design at 900 V instead. The same trends for EK velocity and DEP velocity are observed, albeit with higher magnitudes for each of them, such that the shape of the DEP velocity line is more observable. The particle velocity line differs notably from the EK velocity line and more closely matches the DEP velocity line shape, the maximums in nearly identical positions. Figures 4.3c and 4.3d show the asymmetric design Oval-150-Oval-40 at 300 V and 900 V, respectively. The trends are very similar in the way the shape of the particle velocity line shifts between the 300 V and 900 V, but unlike the symmetric curves before, the shape of the EK velocity line and the DEP velocity line are notably different. The velocity climbs up gradually as it approaches the point of minimal vertical distance between the posts and drops off sharply for the EK velocity line. For DEP, more observable in Figure 4.3d where the shape is clear, DEP repulsion gradually increases as the particles approach the constriction before reaching zero and then sharply repelling upstream instead at a higher maximum than the previous downstream repulsion. Based on the information in Figure 4.3, where DEP behavior made an observable shift in total particle velocity, 900 V should

provide a sufficient voltage for the streaming regime and can be used for simulations and experimental work.

4.3 CORRECTION FACTOR WORK AND GEOMETRY OPTIMIZATION

The geometry of the insulating posts modifies the electric field distribution and electric field gradients within the microchannel. The first goal of this project was to attempt to optimize the post geometry for two different types of separation, separation based on particle size and separation based on particle charge. The thought behind this selection is that separations based on particle size rely largely on DEP, meaning posts with higher electric field gradients should produce optimal results, and separations based on particle charge rely largely on EP[1]. To adequately simulate the geometries, correction factors were first experimentally determined.

Table 4.1 shows the particles used in these experiments. All particles were run through the device shown in Figure 4.2a. With respect to the streaming regime determination simulations, 900 V were used. As the goal of this project is to optimize retention time differences between particles, retention time is also the factor used to determine the correction factor. Particles were injected into the post array, and the time between initial injection and peak particle fluorescence, measured at the interrogation window from Figure 4.2a and analyzed using ImageJ, was recorded for each particle. A minimum of three data sets were utilized to find the experimental retention time for each particle.

Table 4.1 Experimental and simulations results for particle retention time, correction factor found based on the results, and separation efficiency for comparisons to other methods. Correction factor experiments were performed using the Circle-200 HS-90 design and run at 900 V. Reprinted with permission from [67]. Copyright (2020) Springer Nature.

#	Particle, brand, surface functionalization	ζ_P (mV)	Predicted t_R (s)	Experimental $t_{R,e}$ (s)	Separation efficiency (N/m)	Correction factor (c)
1	**1.1 µm, Magsphere, Non-functionalized**	-61.4	41.8	43.9±2.0	3,968±584	171.0
2	**2 µm, Magsphere, Non-functionalized**	-39.4	25.9	72.3±10.5	1,890±156	149.0
3	**2 µm, Magsphere, Carboxylated**	-57.5	32.1	35.1±2.9	7,734±1,405	84.0
4	**2 µm, Magsphere, Carboxylated**	-63.8	44.8	61.9±5.1	3,865±622	81.0
5	**5 µm, Magsphere, Carboxylated**	-53.8	34.5	40.4±4.1	24,799± 3617	15.0
6	**5 µm, Magsphere, Non-functionalized**	-61.7	42.1	45.0±1.8	20,459±797	9.1
7	**6.8 µm, Magsphere, Carboxylated**	-50.0	31.7	35.2±2.5	8,671±1,621	8.0
8	**7.6 µm, Magsphere, Carboxylated**	-12.4	22.6	42.9±1.9	61,934± 2,964	15.1
9	**9.7 µm, Magsphere, Carboxylated**	-30.8	17.7	52.7±6.8	27,656± 7,178	7.3
10	**10 µm, Invitrogen, Carboxylated**	-72.6	72.7	100.4±3.3	153,724± 9,226	2.5

Experimental retention times were then used with COMSOL Multiphysics®. As shown in Equation (2.8), the correction factor ‘c’ is used as a multiplier for the DEP velocity. The column describing the predicted retention time refer to the initial retention time found in simulation with a correction factor value of 1. This is the initial starting point for the simulations. Different correction factors were tested until a simulated value closest to the experimental retention time value could be found. The final correction factors are shown in the right-most column of Table 4.1. A couple of notable trends can be seen in the correction factor values. Larger particles require smaller correction factor values and particles with higher magnitude zeta potentials of the same size have lower correction factors. The first result fits with trends in correction factors observed from other

experiments [65]. One interesting deviation in the trend based on size is in the case of Particle #8, the 7.6 μm green Magsphere carboxylated particles. These particles have a higher correction factor than the 5 and 6.8 μm particles, but they have a significantly lower magnitude zeta potential, indicating that size is not the only factor of importance in these results. The lower magnitude zeta potential also means that EP^1, which acts in the opposite direction as EO, is significantly lower in this situation, so the linear EK force would be higher. Indeed, this might be an interesting factor to consider regarding the concept that EP^3 might be responsible for the majority of the discrepancy between simulations and actual experimental results.

The separation efficiency column in Table 4.1 is built mainly to compare this technique to other separation techniques. Separation efficiency, or theoretical plates per meter, is a concept originally developed around separation columns with actual plates. Theoretical plates, used to calculate separation efficiency, represent a way to standardize the effectiveness of vastly different types of separation techniques. Equation (2.13) shows the calculation used to calculate these numbers. The range of values, 1,890-153,724 plates/m, is comparable to ranges of other separation efficiencies from recent CE papers. One explores protein characterization with values that range from 1,830-11,800 plates/m [68], and another uses EO flow modulation with a range of 46,000-685,000 plates/m [69]. The separation efficiencies found for this chromatographic system are comparable to other modern separation efficiencies, indicating that the technique has potential to compete with other separation techniques.

Retention time results were run in the simulations with and without the correction factors applied to the DEP velocity. Retention time differences between particles of the

same size and particles of similar charge were used to find the optimal design for separations by size and separations by charge. This is due to the potential for slight differences among correction factors for the different geometries. The results are summarized in Table 4.2 and Table 4.3.

Table 4.2 Comparison of retention time differences for particles of the same size and different charges. Particle numbers match those in Table 4.1. The bolded red row indicates the design chosen as the optimal design. If the highest value is also optimal among the options, it is underlined. If not, the highest value is bolded and underlined in black. The information is given first for simulations run without the correction factor and then for simulations run with the correction factor. Reprinted with permission from [67]. Copyright (2020) Springer Nature.

Separation by charge comparison				
Without correction factor				
Design name		**Particles #9 and #10**	**Particles #5 and #6**	**Particles #2 and #4**
		Retention time difference (s)	**Retention time difference (s)**	**Retention time difference (s)**
1	Circle-200 HS-20	33.95	6.56	16.14
2	Circle-200 HS-90	39.49	7.66	18.86
3	Oval-200-80	40.19	6.88	16.89
4	Diamond-200-80	TRAP	7.03	17.23
5	Oval-100-Oval-40	38.77	7.40	18.19
6	Oval-150-Oval-40	38.97	7.57	18.64
7	Oval-200-Oval-40	39.06	7.65	18.85
8	**Oval-250-Oval-40**	**39.37**	**7.75**	**19.10**
9	Oval-100-Diamond-40	38.91	7.37	18.13
10	Oval-150-Diamond-40	39.36	7.62	18.75
11	Oval-40-Oval-150	40.56	7.57	18.64
12	Diamond-40-Oval-150	**46.25**	7.64	18.79
With correction factor				
Design name		**Particles #9 and #10**	**Particles #5 and #6**	**Particles #2 and #4**
		Retention time difference (s)	**Retention time difference (s)**	**Retention time difference (s)**
1	Circle-200 HS-20	41.61	4.37	18.48
2	Circle-200 HS-90	**50.03**	4.19	2.73
3	Oval-200-80	TRAP	TRAP	TRAP
4	Diamond-200-80	TRAP	TRAP	TRAP
5	Oval-100-Oval-40	TRAP	2.41	TRAP
6	Oval-150-Oval-40	43.51	6.24	20.61
7	Oval-200-Oval-40	41.69	6.89	20.17
8	**Oval-250-Oval-40**	**41.24**	**7.22**	**20.09**
9	Oval-100-Diamond-40	TRAP	4.38	TRAP
10	Oval-150-Diamond-40	44.80	6.04	**20.97**
11	Oval-40-Oval-150	TRAP	TRAP	TRAP
12	Diamond-40-Oval-150	TRAP	TRAP	TRAP

Table 4.3 Comparison of retention time differences for particles of the similar charge and different sizes. Particle numbers match those in Table 4.1. The bolded red row indicates the design chosen as the optimal design. If the highest value is also optimal among the options, it is underlined. If not, the highest value is bolded and underlined in black. The information is given first for simulations run without the correction factor and then for simulations run with the correction factor. Reprinted with permission from [67]. Copyright (2020) Springer Nature.

Separation by size comparison				
Without correction factor				
Design name		**Particles #3 and #6**	**Particles #1 and #6**	**Particles #5 and #7**
		Retention time difference (s)	**Retention time difference (s)**	**Retention time difference (s)**
1	Circle-200 HS-20	3.83	0.33	2.35
2	Circle-200 HS-90	4.47	0.38	2.74
3	Oval-200-80	4.05	0.39	2.41
4	Diamond-200-80	4.16	**0.42**	2.43
5	Oval-100-Oval-40	4.33	0.38	2.63
6	Oval-150-Oval-40	4.42	0.38	2.71
7	Oval-200-Oval-40	4.47	0.38	2.75
8	Oval-250-Oval-40	**4.52**	0.38	**2.79**
9	**Oval-100-Diamond-40**	**4.32**	**0.39**	**2.62**
10	Oval-150-Diamond-40	4.46	0.39	2.72
11	Oval-40-Oval-150	4.42	0.38	2.70
12	Diamond-40-Oval-150	4.47	0.39	2.72
With correction factor				
Design name		**Particles #3 and #6**	**Particles #1 and #6**	**Particles #5 and #7**
		Retention time difference (s)	**Retention time difference (s)**	**Retention time difference (s)**
1	Circle-200 HS-20	1.51	0.89	3.84
2	Circle-200 HS-90	1.00	1.05	5.12
3	Oval-200-80	TRAP	TRAP	TRAP
4	Diamond-200-80	TRAP	TRAP	TRAP
5	Oval-100-Oval-40	0.63	1.31	6.11
6	Oval-150-Oval-40	2.93	0.80	3.69
7	Oval-200-Oval-40	3.58	0.65	3.34
8	Oval-250-Oval-40	3.88	0.58	3.22
9	**Oval-100-Diamond-40**	**5.65**	**1.58**	**11.59**
10	Oval-150-Diamond-40	2.70	0.86	3.87
11	Oval-40-Oval-150	TRAP	TRAP	TRAP
12	Diamond-40-Oval-150	TRAP	TRAP	TRAP

From Table 4.2, the optimal design for separations by charge is difficult to determine. The design with the most consistent highest reading across both comparisons without and with a correction factor is the Oval-250-Oval-40 design (Fig. 4.2i). Any design

with the word ‘TRAP’ indicates that one or both of the retention times were incalculable as the simulations indicate that the particles would trap against the posts. Considering the desire to utilize streaming and not trapping for particle separation, these designs were considered ineligible. For separations by size, the assessment was much easier, as can be seen in Table 4.3. While the design did not produce particularly high retention time differences without correction factors, with correction factors the same design consistently yielded the highest values, Oval-100-Diamond-40 (Fig. 4.2j).

For separations by charge, longer posts exaggerate the time it takes for a particle to build to a maximum velocity, leading to both a greater retention time and a greater difference in retention time. This concept is better illustrated by comparing the velocity profiles of all the long side Oval-Oval designs (Fig. 4.2f-4.2i).

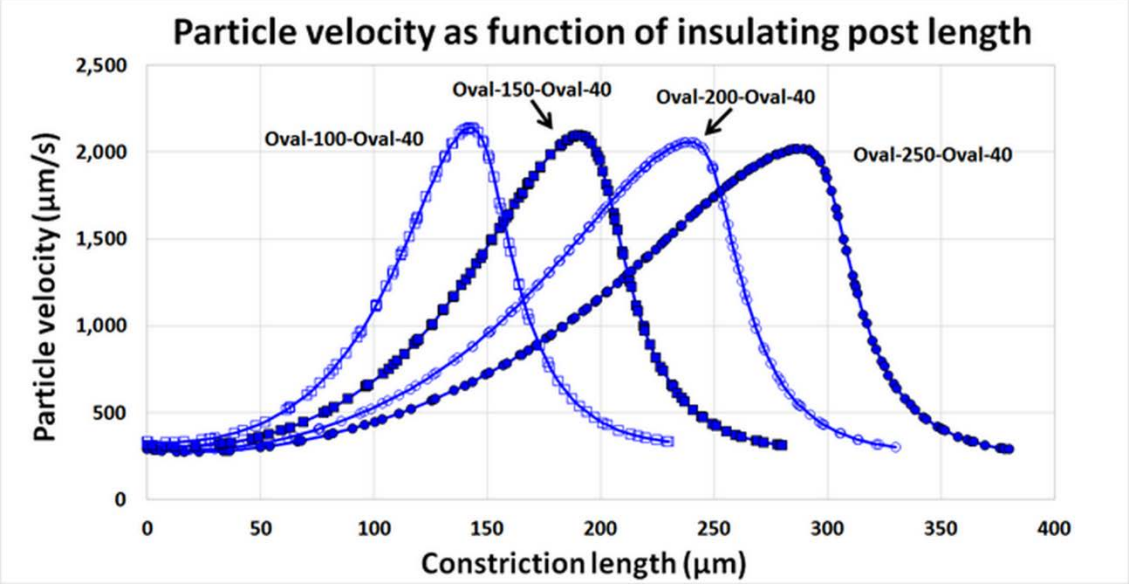

Figure 4.4 Particle velocity plots for Particle #4 (2 µm green Magsphere carboxylated, ζ_P=-63.8 mV) as it migrates across the four long side Oval-Oval designs of increasing constriction length. Note that the maximum velocity and minimum velocity values decrease as the post length increases. Reprinted with permission from [67]. Copyright (2020) Springer Nature.

As shown in Figure 4.4, as the post length increases, the slope of the line decreases, the maximum velocity value reached decreases, and the minimum velocity value reached decreases. These factors contribute to higher retention times and higher retention time differences. For separations by size, where hitting the hurdle of the higher electric field and electric field gradient is more important, shorter posts are key. Shorter posts have shaper increases in electric field and electric field gradient than their longer counterparts. While the desired separation is largely based on streaming, the high electric fields and electric field gradients might temporarily reverse the flow of the particle or slow it significantly. The need to surpass each hurdle as the particles traverse through the system adds up small increments of time to increase the retention time, a factor which is theorized to vary by size so smaller particles have to traverse smaller hurdles and larger particles have greater hurdles.

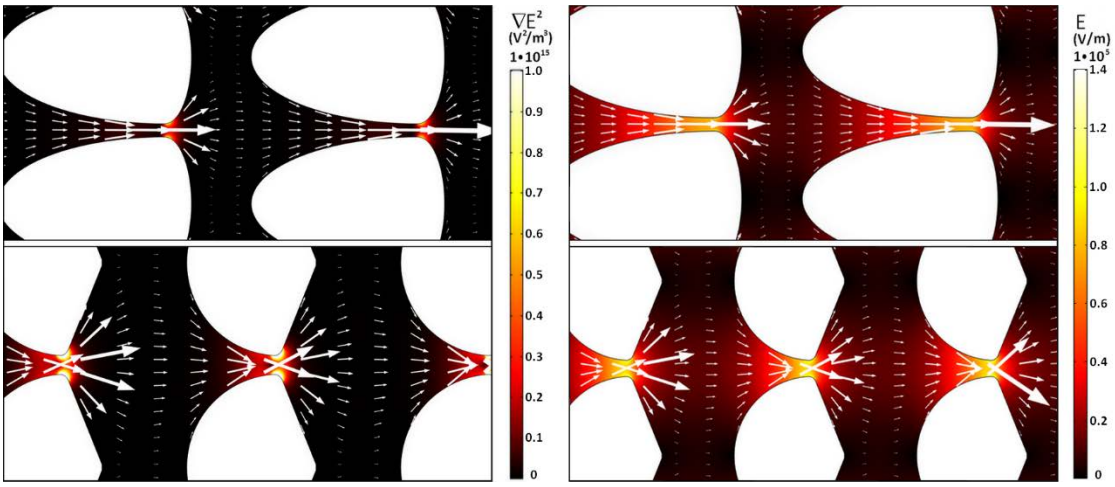

Figure 4.5 Comparison of the particle velocities (arrows), electric field gradients (left images), and electric fields (right images) for the two optimized designs for separation by charge (top, Oval-250-Oval-40) and separation by size (bottom, Oval-100-Diamond-40). Reprinted with permission from [67]. Copyright (2020) Springer Nature.

For post shape, more pointed posts result in higher electric field gradients and higher electric fields, as seen is Figure 4.5. The pure diamond shape had a very high electric

field gradient, but it resulted in particle trapping, removing it from consideration. In general, pointed designs are preferable for separations by size. The results for separations by charge are more varied.

Between the two circle designs (Fig. 4.2b and 4.2c), higher horizontal post spacing is shown to be more suitable for these experiments. Horizontal spacing of 90 μm is optimal for trapping [70] and was capped there for streaming experiments, but theoretically, higher spacing would also improve the separation potential. When particles enter constrictions, they move faster as fluid velocity increases with the decrease in available volume through which fluid can travel, complying with the law of conservation of mass. As they leave, they enter a dead zone of sorts where velocity is at a minimum, only starting to increase as the particles approach the next constriction. With smaller horizontal spacing, the particles are not able to reach the minimum as the constriction comes sooner, leading to particles moving faster throughout the system. While more posts create more hurdles, which would be the case with smaller spacing, increased spacing increases the amount of time that the EK velocity is slowest, or the “dead zone” time with particle velocity at a minimum.

Post symmetry provides an interesting parameter. For posts of roughly the same size, symmetric designs perform quite well. The shorter symmetric posts have much higher electric field gradients, but lead to trapping, and therefore are not desirable for these separations. While symmetric posts show good results, asymmetric posts allow for more tailoring to specific situations of interest.

Post directionality is oriented preferably on the long side (long side leading, short side following, Fig. 4.2f-4.2k) as opposed to the short side (short side leading, long side following, Fig. 4.2l and 4.2m) as short side causes quick and easy trapping, and shows only

modest improvement in retention times. Given that this is a streaming technique, long side is preferable as this allows for the potential of higher voltages without risking trapping as easily.

4.4 SEPARATION BY CHARGE

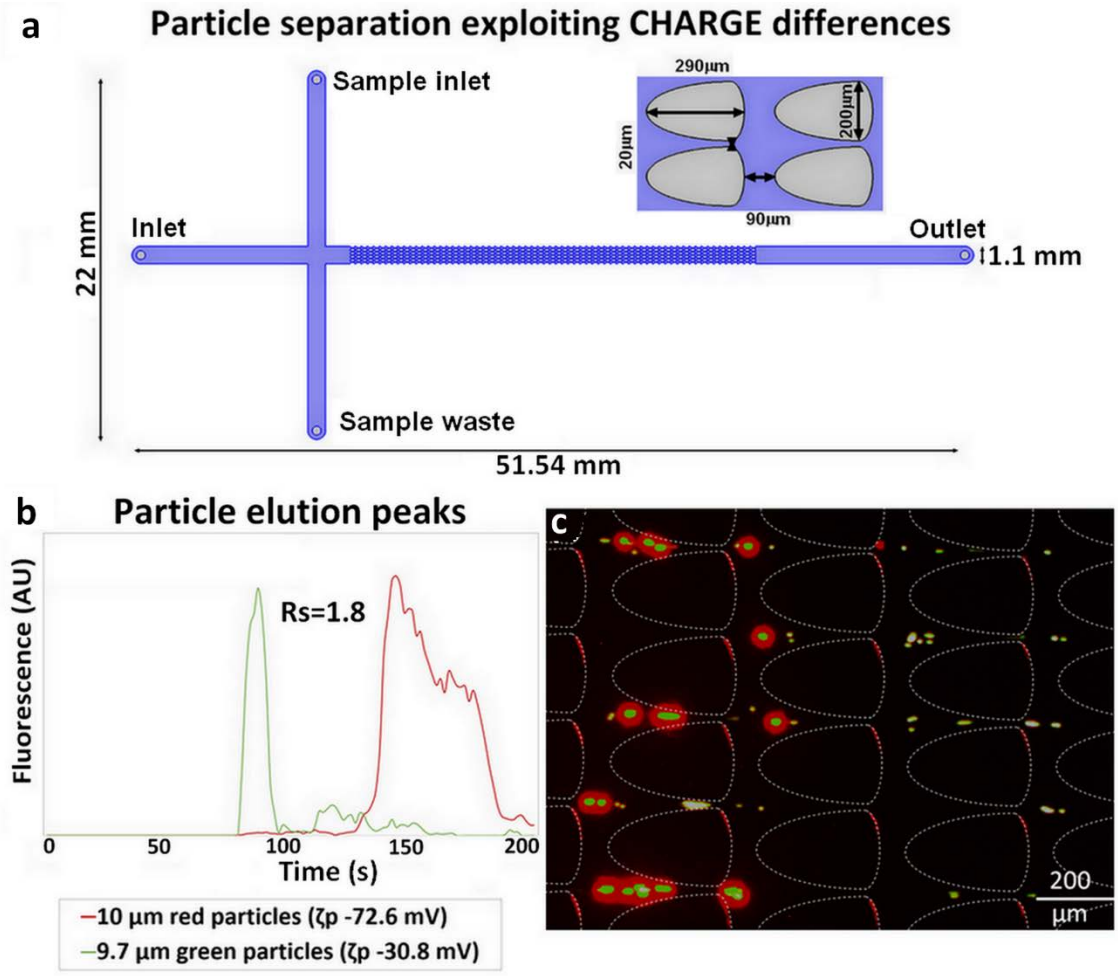

Figure 4.6 Separation of microparticles by charge in Oval-250-Oval-40 design at 1000 V. **a** Channel design with the post geometry insert included. **b** Electropherogram and **c** image at the beginning of the channel demonstrating the start of particle separation within the post array for two types of 10 µm particles, Particle #9 (green, ζ_P=-30.8 mV) and Particle #10 (red, ζ_P=-72.6 mV). Reprinted with permission from [67]. Copyright (2020) Springer Nature.

Figure 4.6 shows the separation by charge scheme. Two 10 µm, spherical polystyrene particles with a 41.8 mV difference in zeta potential were separated by

injecting a mixture of the sample in the sample reservoir (Fig. 4.6a), creating a sample plug, and applying a 1000 V difference between the inlet and outlet reservoir. The separation resolution, calculated using Equation (2.15), was 1.8, enough to indicate a complete separation. The red peak of the electropherogram (Fig. 4.6b) is significantly wider than the green peak, which decreases the resolution value. In theory, a smaller voltage would help exaggerate differences between the peak values, but the bands would also broaden, meaning the larger difference in peak retention times might not make up for the broader band in terms of resolution. Figure 4.6c was captured near the beginning of the channel and shows the particles beginning to separate into zones, with green particles pulling ahead of red particles in a trend that should continue throughout the post array, leading to an increasingly wider separation between the particle types.

4.5 SEPARATION BY SIZE

Figure 4.7 shows the separation by size scheme. Two similarly charged (4.2 mV difference) spherical polystyrene particles from the same manufacturer but with a 3 μm difference in size were injected into the sample inlet (Fig. 4.7a). A sample plug was electrokinetically injected into the channel and a 1500 V difference between the inlet and outlet reservoirs was applied. The separation resolution, on the electropherogram (Fig. 4.7b) was 3.5, more than enough to indicate a complete separation. There is some green particle leakage into the red particle crossover peak. Particles from any distributor have a range of properties associated with them. Most of the particles will be relatively identical, but there will be some particles that are larger, smaller, or slightly different in surface charge or some other feature that might emerge. Some leakage in the red peak is not unusual. Figure 4.7c was taken near the beginning of the channel and shows the start of

particle separation zones, with the red particles pulling ahead of the green particles. The separations by size and charge both show the potential of this technique; further refining could create better separations, especially with a better understanding of simulation dynamics with the new knowledge of the presence of EP[3] in microfluidic EK channels.

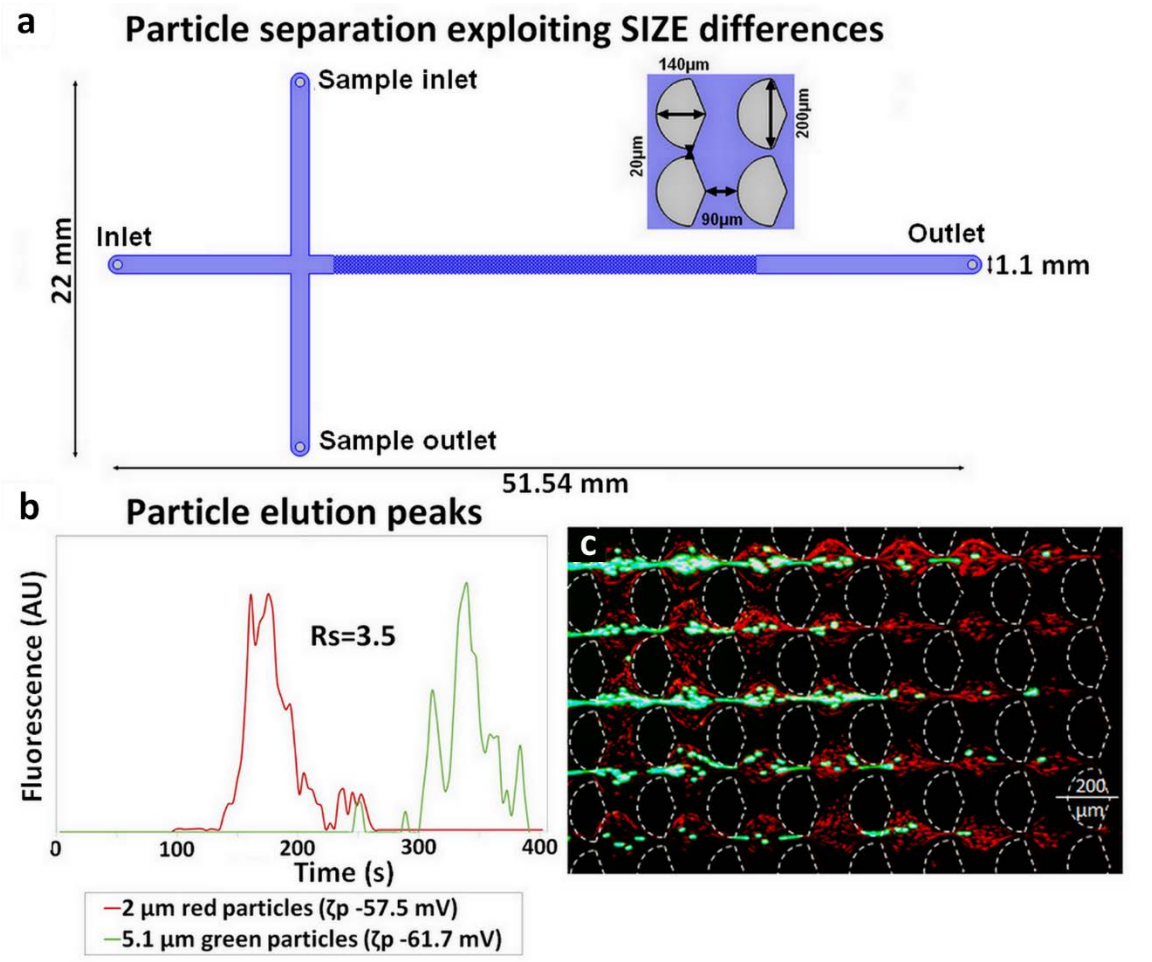

Figure 4.7 Separation of microparticles by size in Oval-100-Diamond-40 design at 1500 V. **a** Channel design with the post geometry insert included. **b** Electropherogram and **c** image at the beginning of the channel demonstrating the start of particle separation within the post array for two types of similarly charged particles, Particle #3 (2 µm red, ζ_P=-57.5 mV) and Particle #6 (5 µm green, ζ_P=-61.7 mV). Reprinted with permission from [67]. Copyright (2020) Springer Nature.

5 EMPIRICAL ELECTROKINETIC EQUILIBRIUM CONDITION

5.1 MOTIVATION

The new shift to understanding the contribution of EP^3 to systems that have historically, attributed the effects of trapping primarily to DEP is going to be a long and challenging road. The ability to simulate EP^3 will quickly become very relevant as the need to properly understand the particle dynamics in a system is eternal. Methods for finding μ_{EP3} are being developed, but something quick that requires minimal analysis and can be applied to previously acquired data would help to make this shift for other groups that need to develop these new methods. Current methods for finding μ_{EP3} and E_{EEC} in the realm of microfluidic EK experiments are explored and improvements on methods that can exploit past images are explained.

5.2 THEORY SHIFT

The prevailing theory that DEP is primarily responsible for the effects of particle trapping in iEK devices was recently tested experimentally by a group that demonstrated both trapping and flow reversal in a channel that could not produce an electric field gradient [37]. The need to explain this trapping and flow reversal behavior at higher voltages led to explorations of literature outside of the field of iEK microfluidics and into the realm of physics. The concept of EP^3 has been understood in the realms of physics and mathematics research for a while [42] and transferring that knowledge to the experimental world of iEK microfluidics is going to be an arduous and significant task.

Another recent publication by our group made the claim that, at least for the particles investigated in that study, the contribution of DEP could almost be considered negligible [39]. While DEP is an important nonlinear EK force, the small contribution and repeatedly cited need for correction factors in order to match results with reality [65]

emphasize the need for EP^3 to be included in order to successfully simulate the forces in iEK systems to match experimental reality.

5.3 THE ELECTROKINETIC EQUILIBRIUM CONDITION

The E_{EEC} represents the voltage at which particles trap in a channel without an electric field gradient, such as postless channels, since DEP prevents mathematic calculation of E_{EEC} (Eq. (2.12)). EP^3 is a force that does not exist at lower voltages. Figure 5.1a shows the progression of particle velocities as the electric field increases assuming a positive μ_{EO} and a negatively charged particle, as positively charged particles would not trap with a positive μ_{EO}. As voltages increase and concentration polarization begins to induce the space charge that leads to EP^3 effects, the linear increase of particle velocity starts to taper off. EP^3 begins to dominate particle motion as it overtakes EO and particle flow stops and eventually reverses. The electric field magnitude, as determined by the applied voltage, at which the particle stops moving is the E_{EEC}. The pictorial representation of forces acting on the particle are labeled like the graph in Figure 5.1a. An example of this motion with arrows acting as vectors of motion in postless channels can be seen in Figure 5.1b.

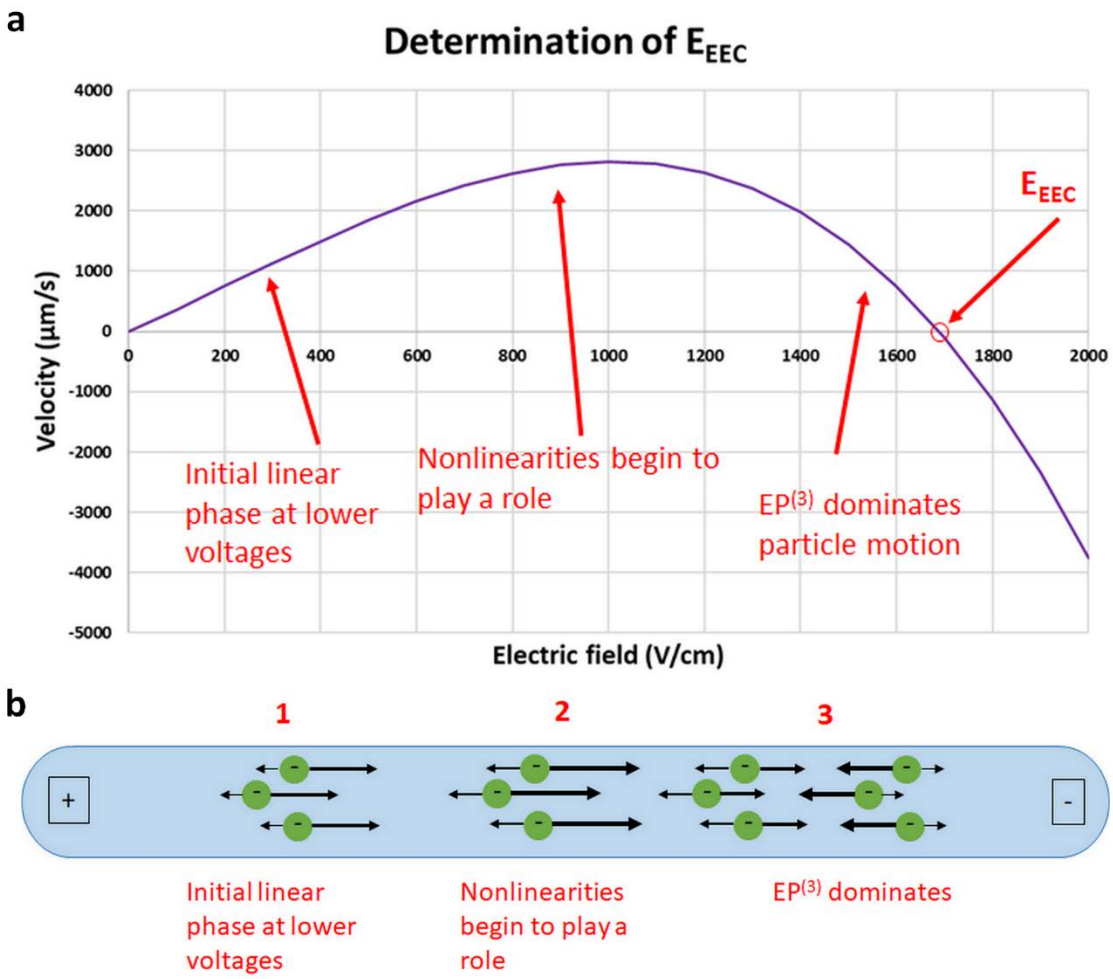

Figure 5.1 Conceptual representation of E_{EEC} in a channel without insulating posts or an electric field gradient based on trends from real experimental results. **a** Example of particle movement as a function of the electric field as it moves through the system. **b** Example of particle movement in the channel with arrows acting to show the relative strength of the vectors. Note that all particles are negative; positively charged particles in a system with a positive μ_{EO}, as explained in the theory, will not trap.

Two recent different papers have determined E_{EEC} in postless channels [37], [41]. In both cases, the parameter was determined by calculating particle velocities for a variety of particles at several different voltages. This means that several different experiments need to be performed with each individual particle and then time consuming analysis needs to be performed to track the average particle velocity for each video of each particle. The process requires several carefully performed experiments with dilute solutions of particles in order to successfully track the velocities of the individual particles. While this allows

for an accurate determination of E_{EEC} and, correspondingly, μ_{EP3}, it is extremely time consuming. Additionally, it can be difficult to reach higher electric fields without the presence of elements, such as posts, that can disturb and concentrate the electric field should that be necessary for the particles of interest. There are machine limits to generating voltages and corresponding limitations such as the potential for electrolysis at higher voltages. While this is the most accurate process, it requires significant time, understanding, and analytical effort.

5.4 METHOD OF FINDING EMPIRICAL ELECTROKINETIC EQUILIBRIUM CONDITION

Another study from our group reported finding the E_{EEC} using a different methodology [39], but further investigation proved that the analysis of this variable needed to be modified.

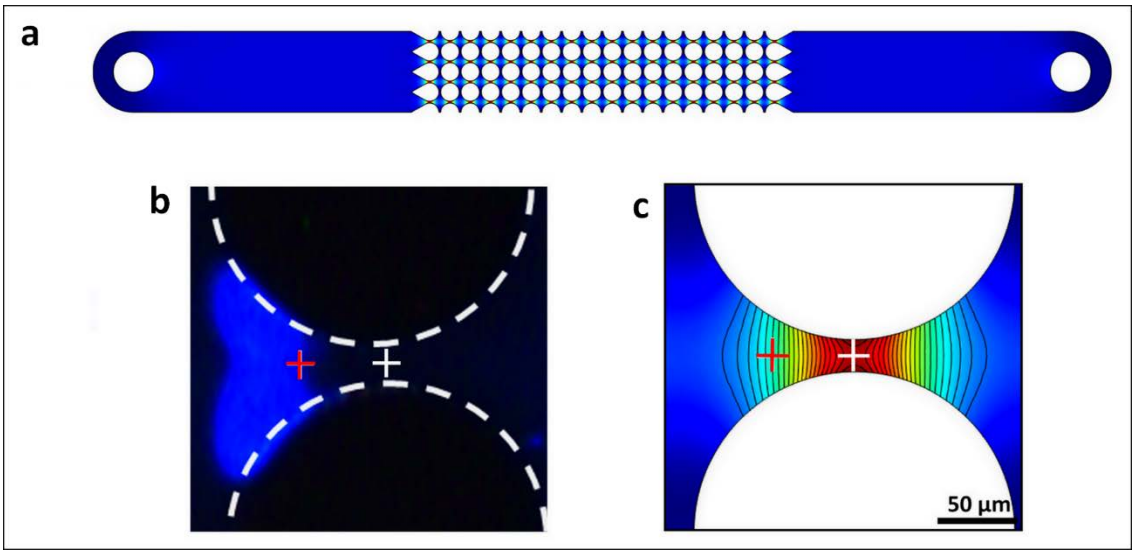

Figure 5.2 Representation of the methodologies for finding eE_{EEC} in channels with posts. **a** COMSOL simulation of a channel with posts and the electric field distribution in the channel. **b** Experimental image of *E. coli* cells trapping at 1000 V between two circle posts. **c** Distribution of the electric field within a constriction region between two circles at 1000 V. The white cross in images **b** and **c** represents the area with the highest electric field in the system. The red cross in images **b** and **c** represents the electric field at the particle band. Reprinted from [40].

Figure 5.2a shows the COMSOL simulation of a channel with circle posts and the electric field distribution between them. This channel with posts has an electric field gradient, and therefore DEP is also a factor in experiments involving these channels. The different methodology noted above can be explained with Figures 5.2b and 5.2c. Particle trapping can be defined in different stages. There is the initial point at which particles trap, the trapping voltage (TV). This is the point at which the first signs of trapping appear. The trapping voltage is then simulated and the electric field at the center of the constriction, the highest voltage in the constriction, is used as the E_{EEC} value. This is indicated by the white cross in Figures 5.2b and 5.2c.

There are a few problems with this approach. Firstly, as DEP is present in this system and, more importantly, particles are highly concentrated, this would not be E_{EEC} as determined in the postless channels. Secondly, trapping voltage relies on observable estimation of a value and can be very difficult to determine. It requires, primarily, that the phenomenon can be observed. Given that the particles used in the study [39] were all biological particles manually dyed in lab and are difficult to see on an individual basis, it can be very difficult to estimate the trapping voltage for these species. Particle trapping may not be observable until the particles are highly concentrated, which would happen at higher voltages, making the estimation relatively subjective. Even with different particles, the trapping voltage is not necessarily observed at the center of the constriction, meaning the electric field at that center point would not be the most accurate value.

To counter these concerns, a new parameter, eE_{EEC}, is proposed. This parameter is meant to apply to systems that have posts and therefore contributions from both DEP and particle-particle interactions that would be caused by the higher concentrations associated

with trapping experiments. The terminology would also apply to the study discussed above, as it shares the DEP and particle-particle interactions. The new method does not require ascertaining a single specific voltage, the trapping voltage, but instead only requires a voltage at which a stable band of particles can be observed, the stable trapping voltages (sTV). This voltage is still applied to simulations, but instead of trying to find the maximum electric field, the electric field at the right-most edge of the band (the point closest to the constriction) is used, as indicated by the red cross in Figures 5.2b and 5.2c. This is the point where particle trapping can be said to begin at a given voltage. When voltages increase, particles are pushed further out, therefore the band should be able to accurately track the electric field at which particle motion is genuinely zero and the particles can be considered trapped. This means that it does not rely on a precise observable moment but instead relies on tracking the band. Since the band is already made of concentrated particles, it is much easier to observe. This method gives more accurate results and can be easily applied to previously completed experiments if trapping was observed within those spaces. This also means that the voltage does not need to be any specific value, just high enough for the observable band to form, and, with post constrictions pinching together electric field lines, there are higher available electric fields between the posts than those that could be found in a postless channel with the same applied voltage. Utilizing this method, the eE_{EEC} can be found.

5.5 ESTIMATION OF EMPIRICAL ELECTROKINETIC EQUILIBRIUM CONDITION

To test this hypothesis, experiments utilizing biological particles trapped between posts were analyzed to determine their eE_{EEC} values. These values should theoretically be

geometry independent as it tracks the exact electric field at the space, but, much like E_{EEC} and all linear and nonlinear EK terms, depend on the media.

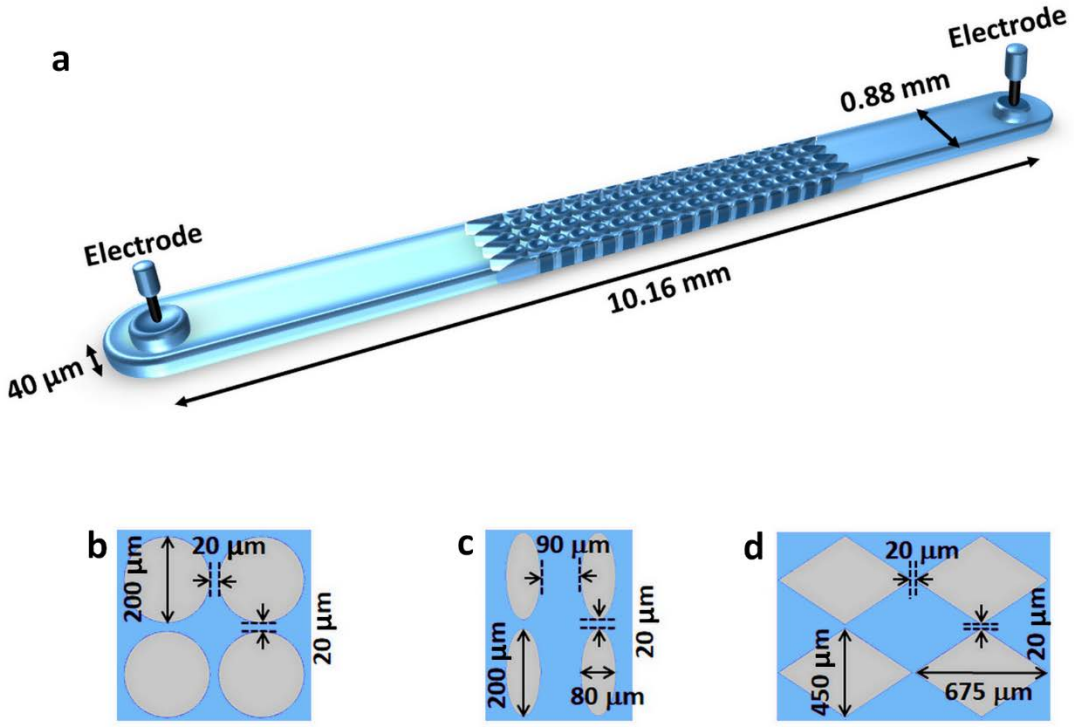

Figure 5.3 Images of the channel and posts used in the experiments analyzed. **a** Representation of the channels used in these experiments. Channel-wide dimensions are accurate for all three post designs, which are **b** circle posts, **c** oval posts, and **d** diamond posts. Reprinted from [40].

All experiments analyzed were performed using channels with the dimensions shown in Figure 5.3a. Three different kinds of posts, circle (Fig. 5.3b), oval (Fig. 5.3c), and diamond (Fig. 5.3d), were used for the experiments.

Table 5.1 List of all the bacteria used in the experiments for this section, along with their eE_{EEC}, the standard deviations, and the coefficient of variation. All eE_{EEC} values were estimated from experimental data. Reprinted from [40].

Species	Size (µm)	eE_{EEC} (V/cm)	CoV (%)
Bacillus cereus (ATCC® 14579™)	**Length:** 4.94±0.47 **Width:** 1.32±0.13	618 ± 32	5.2
Escherichia coli (ATCC® 25922)	**Length:** 2.01±0.42 **Width:** 0.97±0.21	1,092 ± 76	6.9
Salmonella enterica (TT9079)	**Length:** 2.00±0.31 **Width:** 0.97±0.11	1,928 ± 170	8.8

Table 5.2 List of all the bacteriophages used in the experiments for this section, along with their eE_{EEC}, the standard deviations, and the coefficient of variation. All eE_{EEC} values were estimated from experimental data.

Species	Host cell	# of different virion proteins	Genome length (bp)	GenBank accession	eE_{EEC} (V/cm)	CoV (%)
201Φ2-1	*Pseudomonas chlororaphis*	76 [71]	316,674	EU197055	3,094 ± 238	7.7
ΦKZ	*Pseudomonas aeruginosa*	62 [72]	280,334	NC_004629	2,140 ± 107	5.0
SPN3US	*Salmonella enterica*	86 [73]	240,413	JN641803	2,932 ± 246	8.4

The different microorganisms analyzed are listed in Table 5.1 for bacteria and Table 5.2 for bacteriophages, along with the values for their eE_{EEC} determined through the analyses. Three images for each species in each post design, circle and oval for bacteria and circle, oval, and diamond for the bacteriophages, were analyzed and the results were averaged together for each geometry and the species across all geometries. The results should be, largely, geometry independent. Based on the coefficients of variation for the species, the values within species can be said to be reasonably close together.

Figure 5.4a shows the results of each geometry for the bacteria species. The bacteria have a lower eE_{EEC} value than the bacteriophages (Fig. 5.4b), which can be seen when compared together in Figure 5.4c. Given that bacteriophages are notably smaller than bacteria, the smaller values make sense [74]. Larger particles would experience higher EP^3 force and so the values at which larger particles trap should be smaller than the values at which smaller particles trap [75]. The coefficient of variation values across post shapes for all species ranged from 0.8 to 9.9%. For the bacteria specifically, the coefficient of variation values ranged from 0.8 to 8.3% across post shapes and for the bacteriophages, values ranged from 2.5 to 9.9%.

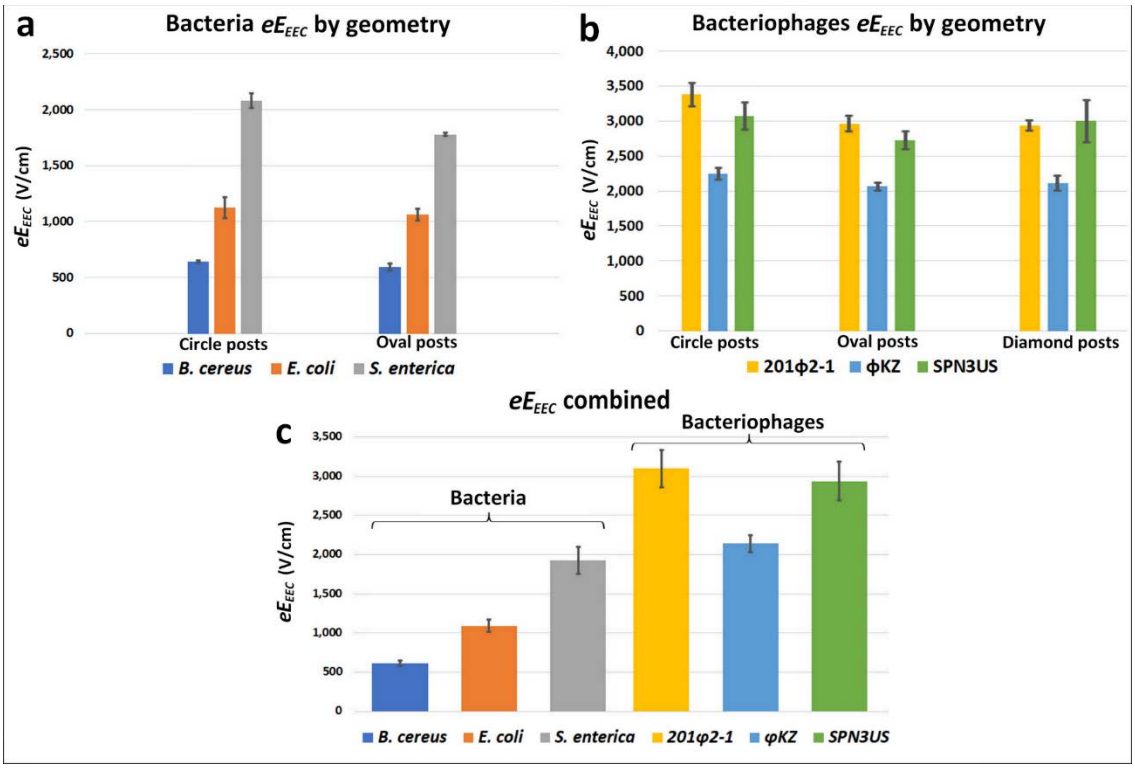

Figure 5.4 The eE_{EEC} values for each post shape and each species analyzed. **a** Results of analysis for bacterial species by post shape. **b** Results of analysis for bacteriophage species by post shape. **c** Average results across all geometries for the bacteria and bacteriophages. Reprinted from [40].

The average standard deviations across all species for the circle, oval, and diamond posts were 4.6%, 3.6%, and 5.8%, respectively. The small values, despite analyzing only three images for each geometry within a species, imply that this technique is not biased towards any particular post shape. The values for each post shape within a species were averaged together, yielding low coefficients of variation (see Table 5.1). The low variability in eE_{EEC} values illustrates high precision and accuracy of this method. Considering the innate population diversity of biological samples, these variations can be partially attributed to that.

5.6 APPLICATION OF EMPIRICAL ELECTROKINETIC EQUILIBRIUM CONDITION TO ESTIMATE STABLE TRAPPING VOLTAGES (sTV)

The applicability of the eE_{EEC} value was tested by using two sample species, the bacteria species *S. enterica* and the bacteriophage species SPN3US. The electric field values in Figures 5.4a and 5.4b were used to estimate sTV values in various geometries. In an effort to provide variance to the estimations, three distinct locations were used for each post shape by employing an average distance from the center of the constriction, with one standard deviation above and below for the other distances. In all simulations, the third column of posts was used to perform a voltage sweep to determine the electric field values. Since these electric field values were found at a single location, the values were linearly dependent on voltage. Linear interpolation was used to estimate the voltage associated with the averaged eE_{EEC} for each shape. The sTV values found at each position were averaged together. The estimated voltages were then compared with the experimental voltages.

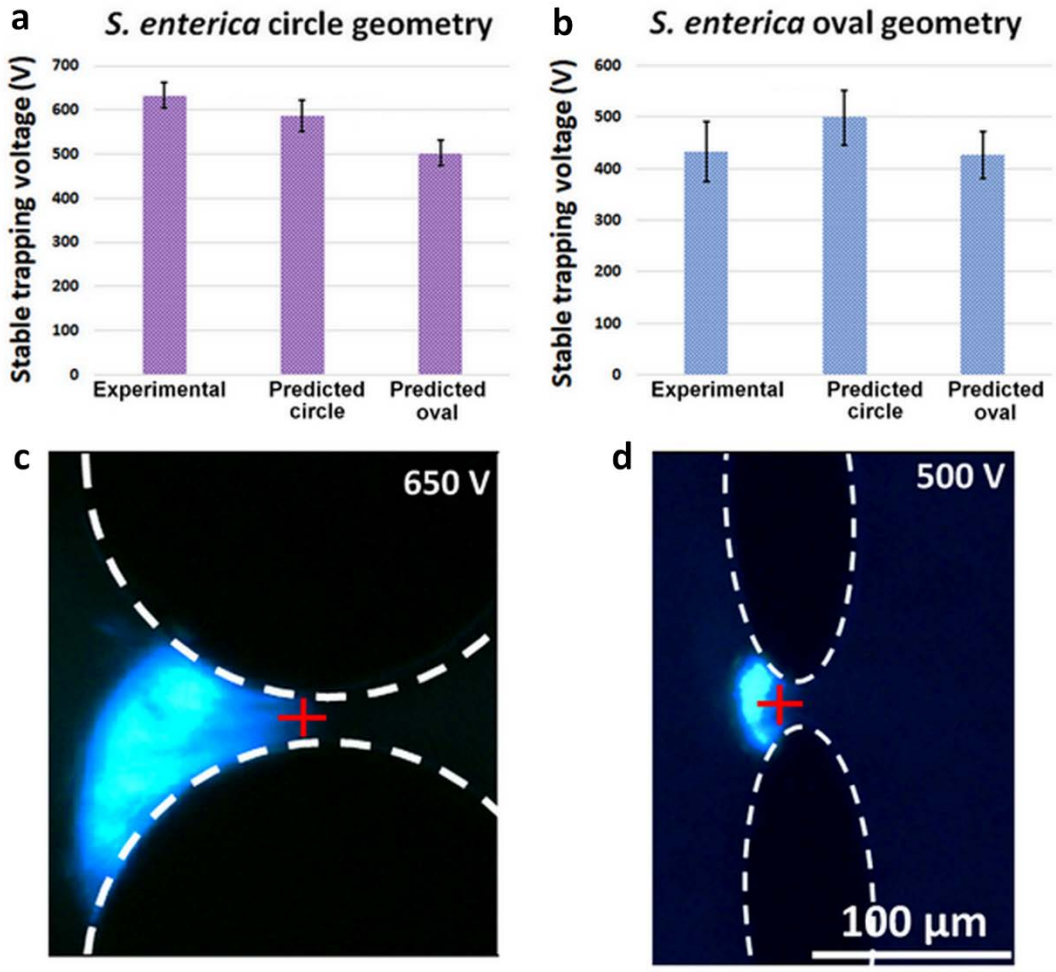

Figure 5.5 Comparison of experimental sTV values and estimated sTV values for bacteria *S. enterica*. Experimental and estimated sTV values for *S. enterica* in **a** circle geometry and **b** oval geometry. Images of trapped microorganisms illustrating the location used for estimations (red cross) for *S. enterica* in the **c** circle geometry at 650 V and the **d** oval geometry at 500 V. Reprinted from [40].

The relative error in the estimation of sTV ranged between 2.0% and 10.2% with an average of 5.2% for *S. enterica*. Only the oval estimation for the circle geometry (Fig. 5.5a) is not within a standard deviation of the experimental result. The estimations of both the circle and oval eE_{EEC} values on the oval geometry were within one standard deviation (Fig. 5.5b). Variations in suspending media characteristics, accuracy for determining band positions, and choice of placement for the red crosses (Fig. 5.5c and 5.5d) can all account for the deviations.

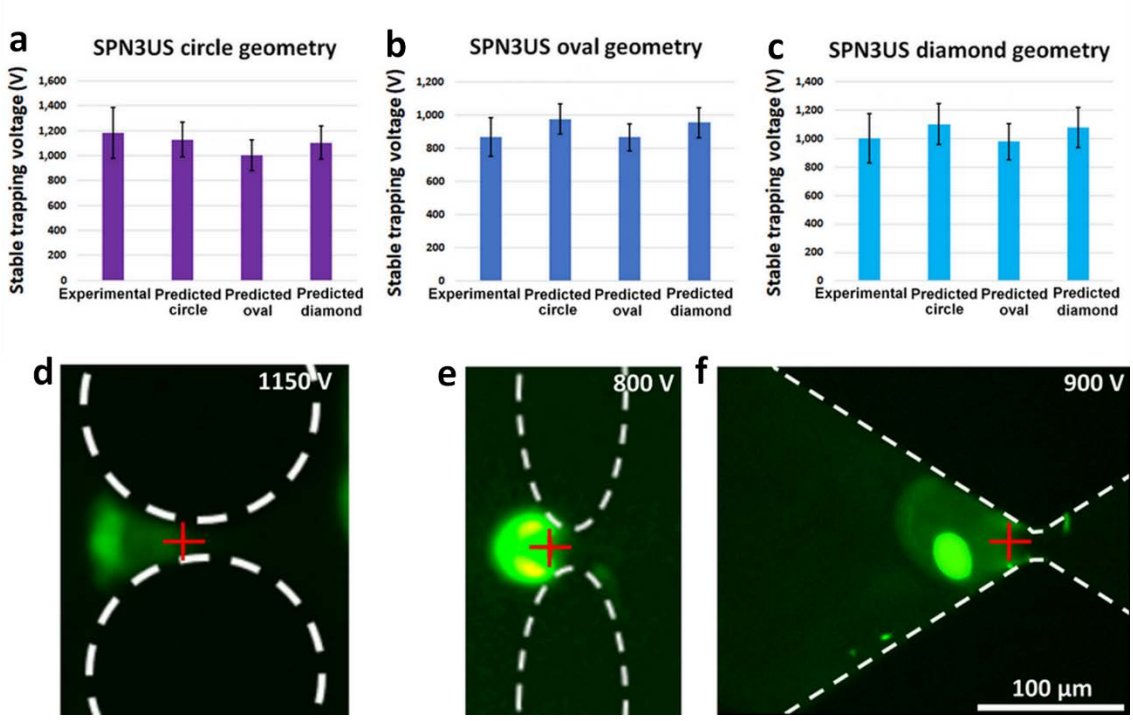

Figure 5.6 Comparison of experimental sTV values and estimated sTV values for bacteriophage SPN3US. Experimental and estimated sTV values for SPN3US **a** circle geometry, **b** oval geometry, and **c** diamond geometry. Images of trapped microorganisms illustrating the location used for estimations (red cross) for SPN3US in the **d** circle geometry at 1150 V, **e** oval geometry at 800 V, and **f** diamond geometry at 900 V. Reprinted from [40].

The relative error in the estimation of sTV ranged between 0.3% and 19.6% with an average of 5.7% for SPN3US. All three results show that the estimates from each individual geometry are within one standard deviation of the experimental geometry values for circle (Fig. 5.6a), oval (Fig. 5.6b), and diamond (Fig. 5.6c) post shapes. Variations in suspending media characteristics, accuracy for determining band positions, and choice of placement for the red crosses (Fig. 5.6d, 5.6e, and 5.6f) can all account for the deviations. The applicability and accuracy of this approach are supported by the small overlap in error bars for everything but the circle experimental geometry with the oval prediction (Fig. 5.5a). To check the similarity of these values, t-tests were performed to test the hypothesis that the predicted values matched the experimental ones, using Equation (2.16), a two-

tailed assumption, and a significance level of 0.05. With the single exception of the oval prediction of the circle experimental geometry (Fig. 5.5a), the t-tests could not reject the null hypothesis.

As expected from previous reports [16], [74], the results for the circle geometry is the highest, followed closely by the diamond when present, then the ovals. This is consistent throughout several experiments. This can also explain the lower values in general for the oval predictions throughout results for both *S. enterica* (Fig. 5.5a and 5.5b) and SPN3US (Fig. 5.6a, 5.6b, and 5.6c). While the sTV estimations may not exactly match the prediction, it can be safe to say that they would give good initial estimations for TV within different systems.

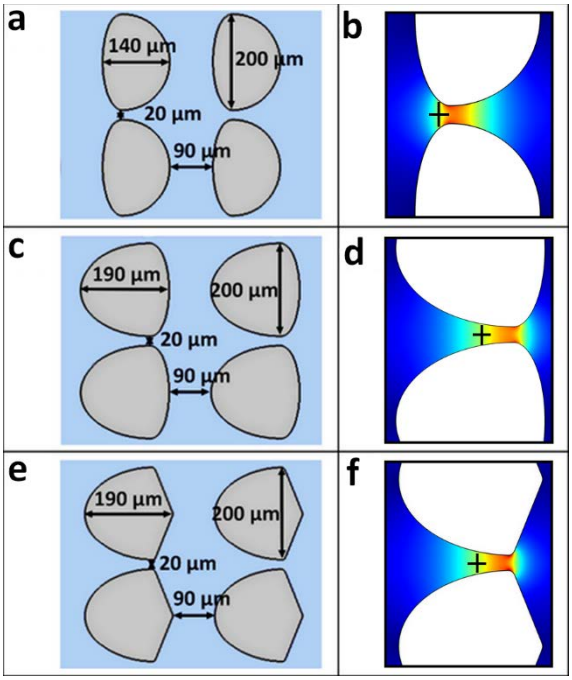

Figure 5.7 Schematic representation of the post dimensions and example of the electric field between the constriction for **a,b** the Oval-40-Oval-100 posts, **c,d** the Oval-150-Oval-40 posts, and the **e,f** Oval-150-Diamond-40 posts. The color distribution represents the magnitude of the electric field where red is the highest electric field value and blue is the lowest. The black crosses represent the location where the sTV values were estimated. Reprinted from [40].

To demonstrate further potential applicability of this technique, predictions of sTV values in three extra post shapes (Fig. 5.7a-5.7f) at positions 25% of the distance from the closest point in the constriction to the left edge of the posts were conducted. This position was used because it is the average distance from the constriction center for the images analyzed in this work. For symmetric post shapes, the highest electric field value exists at the exact center of the constriction, where the distance between posts is at a minimum, but for these asymmetric posts, the highest electric field value is actually a little off from the point where the two posts are closest together (Fig. 5.7b, 5.7d, and 5.7f). For consistency with our previous results, the third column of posts within the channel were used. Results of these simulations can be seen in Table 5.3.

Table 5.3 Predicted sTV values for *S. enterica* and SPN3US in each of the simulated asymmetric post designs. Reprinted from [40].

Species	iEK microfluidic channel	Predicted sTV (V)
S. enterica	Oval-40-Oval-100 (Fig. 5.7a,b)	519
	Oval-150-Oval-40 (Fig. 5.7c,d)	542
	Oval-150-Diamond-40 (Fig. 5.7e.f)	535
SPN3US	Oval-40-Oval-100 (Fig. 5.7a,b)	780
	Oval-150-Oval-40 (Fig. 5.7c,d)	815
	Oval-150-Diamond-40 (Fig. 5.7e,f)	805

As expected from previous results in this investigation, the sTV values are higher for the bacteriophage SPN3US and the bacteria *S. enterica*. Additionally, it can be seen that the highest predicted sTV values are for the Oval-150-Oval-40 design and the lowest are the Oval-40-Oval-100 design. The pointer edge for the Oval-150-Diamond-40 yields a lower sTV than the very similar design with more rounded edges (Oval-150-Oval-40), but the shorter side of the post means the electric field is higher at the 25% distance mark, which can be seen in the darker red at the cross in Figure 5.7b. While these values are

modeling predictions only, they do match previous modeling predictions described in Section 4 and experimental observations for the species, which provides encouragement at the potential of this parameter.

6 ELECTROKINETIC CASCADE DEVICES FOR SAMPLE FILTRATION AND SEPARATION

6.1 MOTIVATION

The ability to effectively filter or prescreen a sample in order to purify, analyze, concentrate, or some combination therein is incredibly useful. The ability to preemptively remove contaminants from samples in the field before collecting smaller particles, such as bacteria, can greatly assist in analysis. Certain very valuable microorganisms, such as bacteriophages, must propagate in bacterial cultures, so purifying and concentrating the samples require the ability to first remove host cells and cell debris from the solution. The combination of these two ideas is the primary motivation behind this work. The cascade device acts as a multi-tier separation platform that can effectively filter or prescreen samples to allow for other analysis further into the system.

Manual transfers of samples between devices have been used in the past by our group to allow for analysis of samples that have contaminating elements in their starting solution. These elements clog the space between insulating posts, impeding the potential of the insulating post array for analysis of the particles. Figure 6.1a shows the scheme for a manual transfer. In Figure 6.1ai, the first stage of sample purification, the largest particles are trapped. After that, sample is removed from reservoir 2 of the circle post design (used for the first device and the first segment of the cascade device) and injected into reservoir 1 of the oval post device, shown in Figure 6.1aii. The second stage of the manual transfer, Figure 6.1aii, removes the medium-sized particles as the purified small particles are left for collection in reservoir 2 of the oval post design. The cascade design scheme, Figure 6.1b, has the same two stages but without removing the sample in between. Instead, after stage one (Fig. 6.1bi) where the large particles are trapped in the circle post design, the

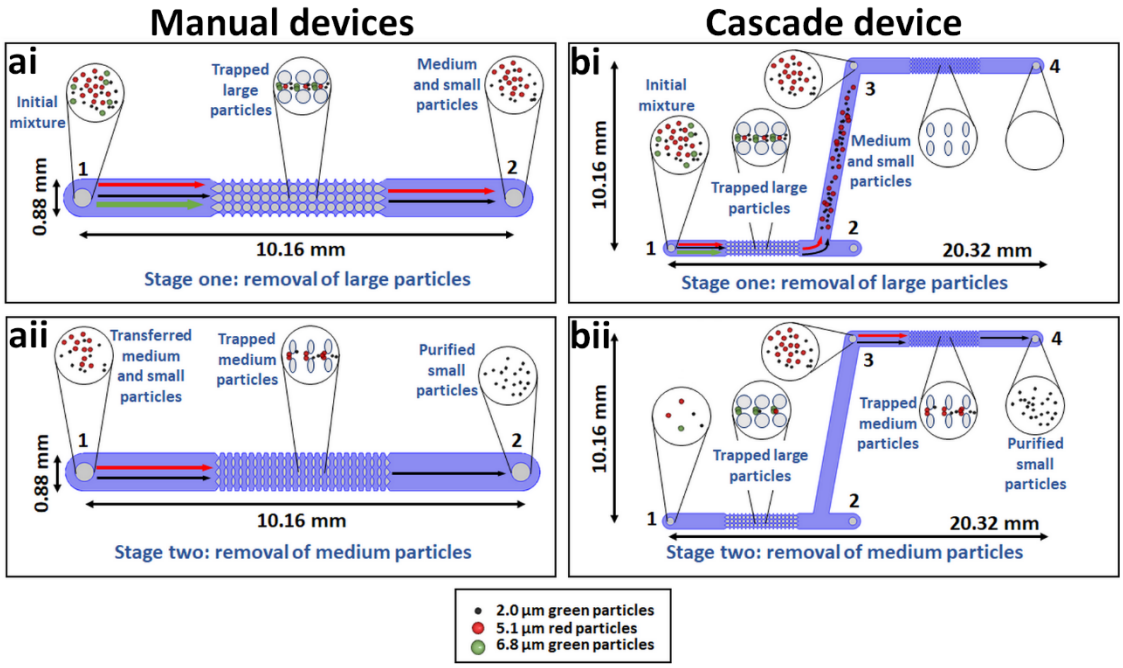

Figure 6.1 Multi-tier separation scheme for both the manual transfer of sample between single post array devices, **ai** and **aii**, and the cascade device, **bi** and **bii**. The reservoirs are numbered from left to right, as indicated by the numbers 1-2 or 1-4, in accordance with the direction of the applied electric field. The devices are divided into two stages with two different applied potential schemes. These stages are built to demonstrate how the cascade scheme works, using the mixture with three distinct particle types (the small black 2 µm particles, medium-sized red 5.1 µm particles, and large green 6.8 µm particles) as an example. **ai** Stage one of the manual transferring process with the circle posts design. This section is used to root out larger particles. Particles are transferred from reservoir 2 of the device in **ai** into reservoir 1 of the oval posts device in **aii**. **aii** Stage two of the manual transferring process with the oval posts design. This section is used to eliminate the medium-sized particles so only the small particles remain. The cascade device is shown in **bi** and **bii**. **bi** For stage one in the cascade device, sample is injected in reservoir 1 and passes through the first part of the iEK device, the circle post array, before being transferred to reservoir 3. The goal is to eliminate the larger particles in this stage. **bii** The second stage of the cascade sequence, particles move from reservoir 3 into the oval post array where the medium-sized particles are trapped and the small particles are able to move to reservoir 4.

medium and small particles are sent to reservoir 3 until the second stage, where the new voltage scheme traps the medium particles in the oval post design (Fig. 6.1bii). The purified small particles are left for collection in reservoir 4. Manual transfers are a way to help filter a sample but tend to lead to sample loss. The cascade device, theoretically, should lead to lower sample loss than the manual device transferring because there is less pipetting, less

chance of loss from particle extraction. Demonstrating lower sample loss in the cascade device over the manual transferring was one of the primary points of interest in this project.

6.2 CHARACTERIZATION OF PARTICLE ELECTROKINETIC TRAPPING

Before experiments in the cascade device could be effectively performed, stable trapping voltages for the particles in the post arrays of interest, circle posts and oval posts, with the media of interest needed to be determined. This information both helps to develop a proper voltage scheme for trapping and establishes whether or not the selected particles have the possibility of working within this scheme. The particles used in this objective are shown in Table 6.1.

Table 6.1 Description of polystyrene particles used in this objective.

#	Particle diameter (μm)	Color	Surface functionality	ζ_P (mV)
1	2.0	Green	Carboxyl	-63.8±5.9
2	5.1	Red	Carboxyl	-53.8±8.6
3	6.8	Green	Carboxyl	-50.0±9.9

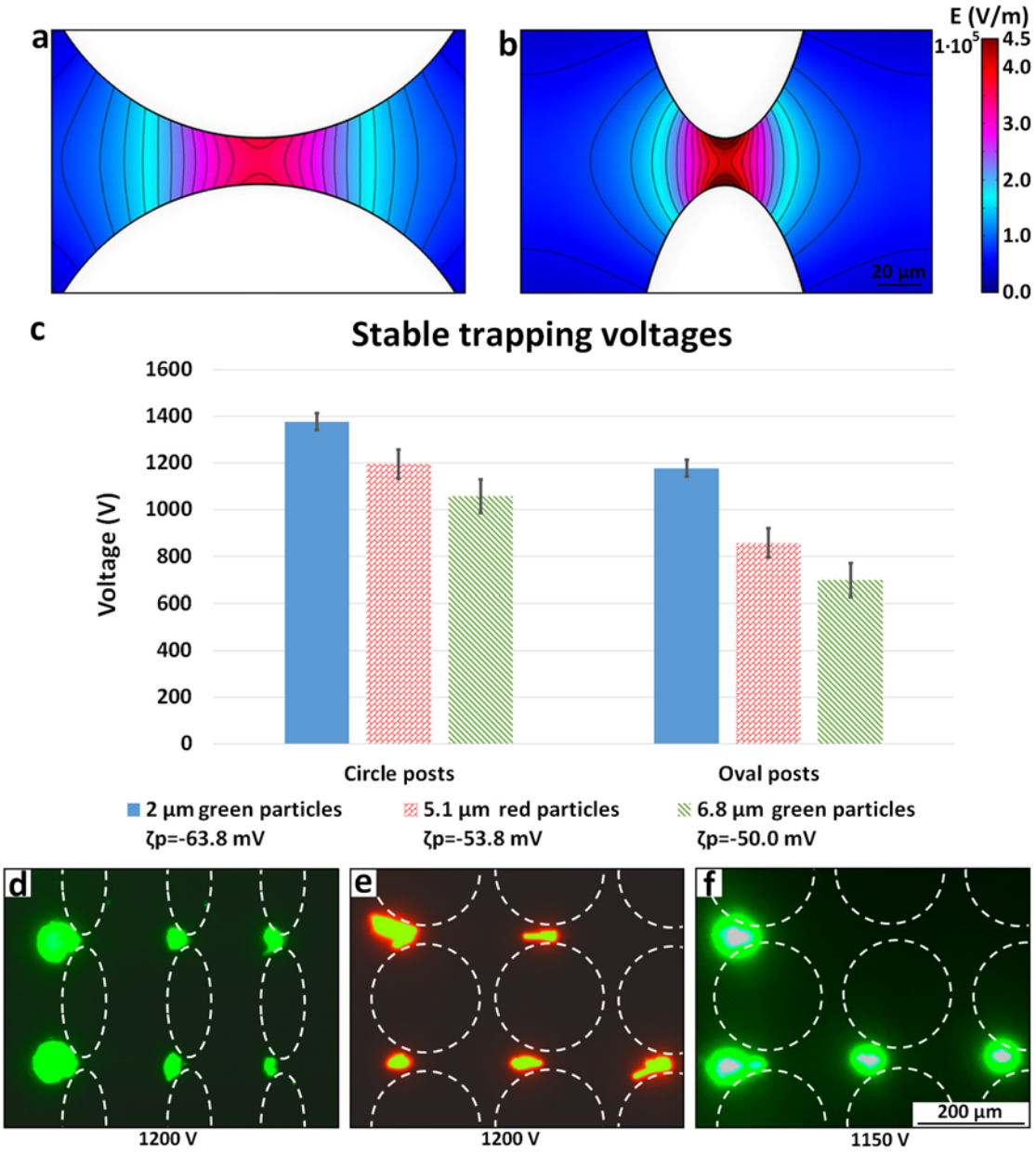

Figure 6.2 Stable trapping voltages for the three polystyrene particles used in this objective. The electric field distribution for **a** the circle post design and **b** the oval post design at 900 V are shown. The darker red color represents the higher electric field magnitudes and the darker blue color represents the lower electric field magnitudes. **c** The stable trapping voltages, the point at which particles have minimum movement between posts, for each polystyrene particle used in these experiments. **d** The 2 µm green particles trapping in the oval post design, **e** the 5.1 µm red particles trapping in the circle post design, and **f** the 6.8 µm green particles trapping in the circle post design.

Figure 6.2 shows the electric field distribution in the two chosen post designs and the stable trapping voltages for the particles used in this objective. The choice of post shapes for this study was based on frequently used designs in our group. As shown in

Figures 6.2a and 6.2b, circle posts have the lower electric field values and oval posts have a much sharper rise in electric field values. Figure 6.2c demonstrates that circle posts have higher trapping voltages in general and are less selective while oval posts have lower trapping voltages and greater discrimination between particle types. Given the notably higher electric field distribution around the oval posts at the same voltage, the lower trapping voltages for particles in the oval post design is expected, as is higher particle discrimination. However, the required potential for achieving particle trapping in the oval posts is more greatly impacted by clogging, so using circles to first remove the larger particles and then the more discriminating ovals to purify the smaller particles works well for sample separation. The oval posts also allow for improved particle concentration at lower voltages than the circles, ideal for sensitive biological particles. Figures 6.2d-6.2f show the stable trapping of particles in the post designs; minimal particle movement between posts give the stable trapping voltages desired for this objective. Figure 6.2c shows that the particles can be separated and the second post array, the oval post design, will be much more effective at removing the 5.1 μm particles from the 2 μm particles.

6.3 COMPARISON OF MANUAL DEVICE TRANSFERRING AND CASCADE DEVICE

Once stable particle voltages were established, the voltage schemes could be designed for the separation process. These applied voltages are near but lower than the stable trapping voltages, which work as a starting point, as particle-particle interactions influence the trapping voltages [76]. For the manual devices, 850-900 V was used for the first stage voltage trapping scheme with the circle post design (Fig. 6.1ai) and 700-800 V

for the second stage voltage trapping scheme with the oval post design (Fig. 6.1aii). For the cascade devices, the first stage (Fig. 6.1bi) applied 850-900 V to reservoir 1, 0 V to reservoir 2, -400 V to reservoir 3, and -200 V to reservoir 4. The voltage difference between reservoirs 1 and 2 in this stage matches that of the manual device for stage one, but the negative applied voltages were used to transfer particles to reservoir 3. The most negative voltage was applied to reservoir 3 so particles would transfer there, but an additional negative voltage was applied to reservoir 4 in an attempt to prevent pushback of particles into reservoir 3. The second stage in the cascade device (Fig. 6.1bii) was the same throughout all trials with 1500 V applied to reservoir 1, 900 V applied to reservoir 2, 900 V applied to reservoir 3, and 0 V applied to reservoir 4. The highest voltage (reservoir 1) was applied to prevent particles trapped in that post array from leaking. Reservoirs 2 and 3 had the same applied voltage so particles would be unlikely to transfer between the reservoirs, meaning the primary area of interest between reservoirs 3 and 4 had a voltage difference of 900 V. This is higher than that applied for the manual devices, partially because voltage leakage between channels meant that the higher voltage was more effective for trapping the medium-sized particles. A minimum of nine repetitions were performed for each scheme, the manual device transfer scheme (Fig. 6.1a) and the cascade device scheme (Fig. 6.1b). The results are given in Figure 6.3a.

The original concentration of the small green particles was $2.28 \cdot 10^8$ #/mL with 5 µL injected into the original device. The processing in the device ran for a total of four minutes, two minutes for stage one and two minutes for stage two. This is true of both the manual transferring process and the cascade device. Between the first and second stage, 50 µL were withdrawn from reservoir 2 of the circle post device (Fig. 6.1ai) and injected into

reservoir 1 of the oval post device (Fig. 6.1aii). For both schemes, 50 µL was withdrawn from the final reservoir (reservoir 2 for the oval post design and reservoir 4 for the cascade design) and 10 µL of sample was used for each side of the hemocytometer. The average value of the count from both sides of the hemocytometer was used as the value for that experimental run.

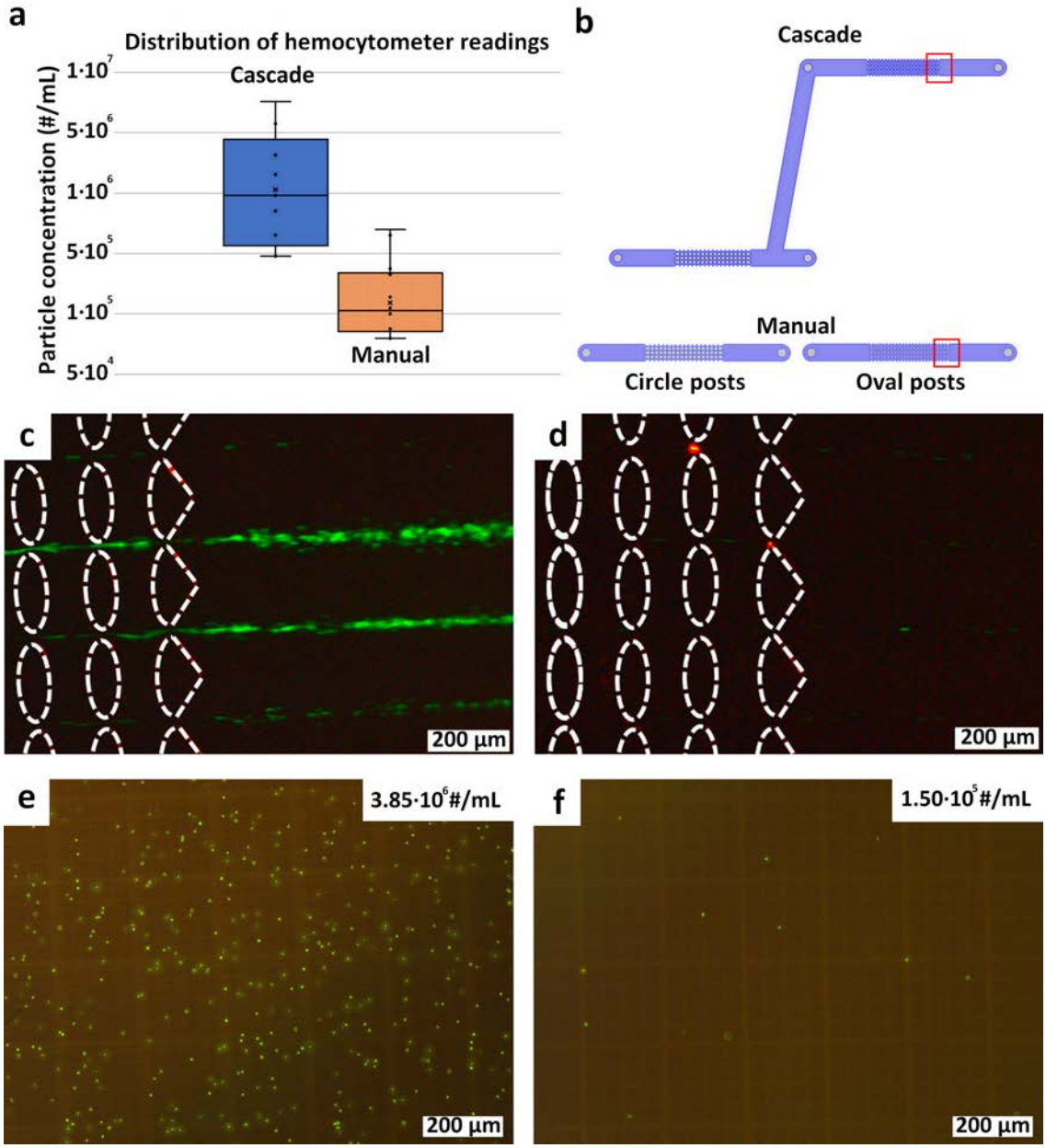

Figure 6.3 Hemocytometer readings for several trials of both the cascade device and manual device transfer runs. **a** Distribution of hemocytometer readings for the cascade device and the manual device transferring process on a log scale. **b** Schematic of the devices used during these experiments. Red interrogation windows show where images **c** and **d** were taken in the channel. **c** Image of the outlet of the cascade device where the red interrogation window on the cascade device in **b** shows. **d** Image of the outlet of the oval post device where the red interrogation window on the oval post device in **b** shows. **e** Representative image of a hemocytometer reading from the cascade device. Final particle count is listed as $3.85 \cdot 10^6$ #/mL. **f** Representative image of a hemocytometer reading from the oval post device. Final particle count is listed as $1.50 \cdot 10^5$ #/mL.

From the results demonstrated in Figure 6.3a, it is clear that the cascade device incurs less sample loss than the manual cascade, with an order of magnitude difference between average concentrations. Higher concentrations could be achieved through longer times for the sample to process and more refinement of voltage schemes. The conditions were kept as consistent as possible between devices to allow for a fair comparison. It should be noted that both techniques did have the odd medium sized particle, and one trial of the cascade scheme had a large green particle, but there was very little contamination from the other particles and this could be explained by an abnormal particle outside of the normal particle distribution for charge. Figure 6.3b shows the devices for each scheme and gives red interrogation windows for the images of Figures 6.3c-6.3d. These images were taken at the end of the oval post array, and while Figure 6.3c shows a healthy particle stream in the cascade device, Figure 6.3d shows a far less concentrated stream of green particles from the manual transferring scheme. These images are representative of the results over several trials. Figure 6.3e is one of the hemocytometer readings for the cascade scheme samples and has a large smattering of particles across the surface. Figure 6.3f is one of the hemocytometer readings for the manual transferring scheme samples and shows a far sparser distribution of particles. The hemocytometer readings correspond to the experimental images in Figures 6.3c-6.3d. It is safe to conclude that the cascade device scheme does reduce sample loss during EK processing.

6.4 CASCADE DEVICE APPLICATION: BACTERIOPHAGE PURIFICATION

Bacteriophages are very valuable microorganisms, but current separation techniques are not very versatile and have low yield, especially for giant bacteriophages [77], [78], a non-taxonomic term generally used to refer to bacteriophages with >200

kilobase pairs in their genome [78]–[81]. Electrokinetic purification has been used successfully on bacteriophage samples in our group [24], but there was significant clogging, leading to the necessity of manual transfers in order to be able to electrokinetically analyze the bacteriophages. The cascade device presents a good alternative for removing and purifying samples of bacteriophages in a single device. In particular, the cascade device can remove sources of clogging in the first stage, such as cells and cell debris present in the growth solution for the bacteriophages, and allow the bacteriophages to be concentrated or even analyzed downstream in the second stage. Three distinct bacteriophage species, PhiPA3, PhiKZ, and SPN3US, were purified using the cascade device. All three bacteriophages belong to a related group of large bacteriophages notable for large, complex virions comprised of a large number of different proteins relative to other tailed bacteriophages [72], [73], [82]–[85]. Initial titers for the bacteriophages used in this objective were $1 \cdot 10^{10}$-$1 \cdot 10^{11}$ pfu/mL. Information on these bacteriophages is in Table 6.2.

Table 6.2 Description of bacteriophages used in this objective.

Species	Host cell	# of different virion proteins	Genome length, bp	GenBank accession
ΦPA3	*Pseudomonas aeruginosa*	>70*	309, 208	NC_028999
ΦKZ	*Pseudomonas aeruginosa*	62 [72]	280,334	NC_004629
SPN3US	*Salmonella enterica*	86 [73]	240,413	JN641803

* Expected number of different virion proteins based on genome similarity between PhiPA3, PhiKZ, and SPN3US [72], [73], [84].

Each bacteriophage sample was first prescreened in the circle post array before being concentrated in the oval post array.

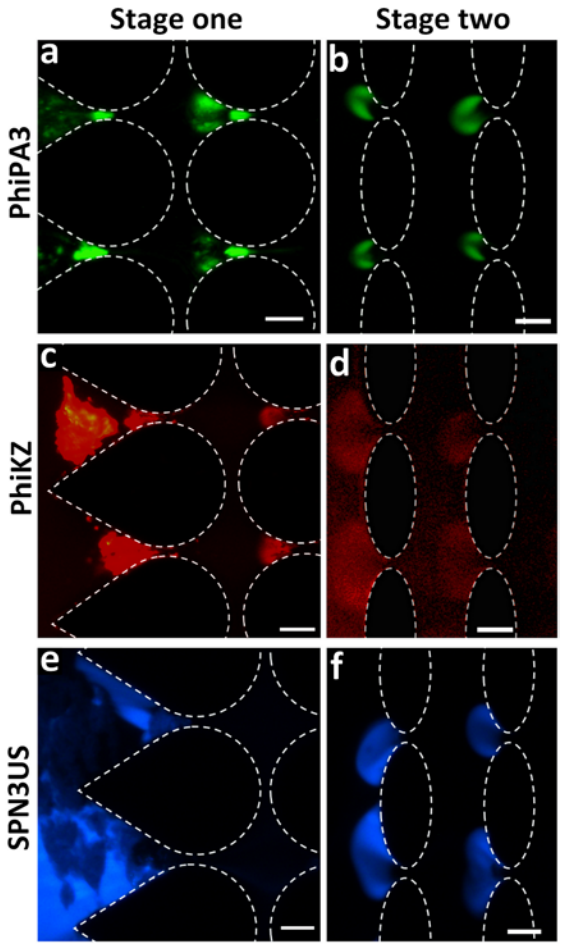

Figure 6.4 Images of EK trapping of all three bacteriophages and the corresponding cells and cell debris in the cascade device. Cells and cell debris from the growth solution are trapped in stage one while bacteriophages are trapped in stage two. All scale bars in the images are 50 µm in length. **a** Cell debris from the PhiPA3 sample trapped in the circle posts of stage one of the cascade and **b** PhiPA3 virions trapped in the oval posts of stage two of the cascade device. **c** Cell debris from the PhiKZ sample trapped in the circle posts of stage one of the cascade and **d** PhiKZ virions trapped in the oval posts of stage two of the cascade device. **e** Cell debris from the SPN3US sample trapped in the circle posts of stage one of the cascade and **f** SPN3US virions trapped in the oval posts of stage two of the cascade device.

Figure 6.4 shows each of the three bacteriophages and the debris prescreened from the samples. The bacteriophages appear as clouds in the channel as opposed to brighter, more vivid, solid color chunks that characterize the cells and cell debris. The bacteriophages can be seen as bands due to the trapping process and are much easier to see as a mass in bands than individual microorganisms, indicating that the bacteriophages are being enriched at the posts. The sample for PhiPA3 can be seen in Figures 6.4a and 6.4b,

with Figure 6.4a showing the trapping of host cells and cell debris and Figure 6.4b showing the trapping of bacteriophages. The same can be said of PhiKZ as illustrated Figures 6.4c-6.4d and SPN3US for Figures 6.4e-6.4f.

Phage viability was tested for one bacteriophage, PhiKZ, as a representative for all the bacteriophages. An initial sample was run using dyed bacteriophages to track movement; a second sample, same bacteriophages but a different starting titer, was run with undyed bacteriophages. The dyed bacteriophages established the voltage scheme. The sample was run through the cascade for two minutes, one minute in stage one, half a minute in stage two for enrichment, and then half a minute to transfer the enriched bacteriophages from the oval post array to reservoir 4.

Figure 6.5 shows the assessment for the dyed and undyed bacteriophages. These images were obtained from bacterial lawns. Bacterial lawns are bacterial growth media plates evenly coated with a chosen bacteria, *Pseudomonas aeruginosa* in this case. To assess bacteriophage viability, a 5 µL sample of the diluted bacteriophage PhiKZ was applied to the bacteria lawn. The order of magnitude of the dilution is indicated by the negative numbers in Figure 6.5. The bacteriophages created ‘holes’ or ‘plaques’ in the bacterial lawn, represented by the dark spots. A 10 µL sample of bacteriophage solution was diluted with 990 µL of SM media, refrigerated, and then continuously diluted by an order of magnitude for each dilution until the individual bacteriophage colonies were identifiable. At this point, the bacteriophage titer is calculated to determine the concentration using the units of pfu/mL, or plaque forming units per mL. As the bacteriophages are able to lyse the cells, this is a way to test the number of viable bacteriophage plaque forming units. The samples before any EK processing were retrieved

after the dyeing process or, for the undyed sample, after the same processing but without the dyeing phase for consistency purposes. The samples retrieved from the cascade devices post EK processing were withdrawn as described in Section 6.3; namely, 50 µL were withdrawn from reservoir 4 once the voltage steps were finished and then 10 µL of that sample were diluted. The resulting titers are listed below in Table 6.3.

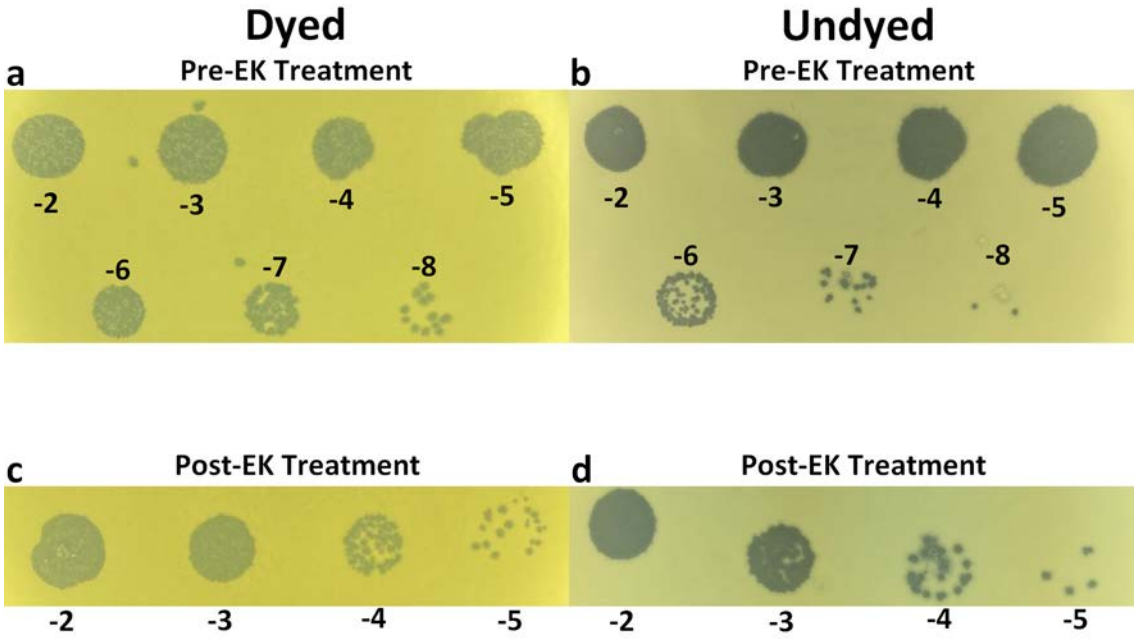

Figure 6.5 Qualitative viability assessment for a representative bacteriophage, PhiKZ, **a** before EK treatment for dyed bacteriophages, **b** before EK treatment for undyed bacteriophages, **c** after EK treatment in the cascade system for dyed bacteriophages, and **d** after EK treatment in the cascade system for undyed bacteriophages. Negative numbers indicate the dilution order of magnitude associated with the sample.

Table 6.3 Averaged titers from the PhiKZ samples.

Sample	Titer
Dyed Pre-EK	$2.4 \cdot 10^{11}$
Undyed Pre-EK	$8.0 \cdot 10^{10}$
Dyed Post-EK	$4.3 \cdot 10^{8}$
Undyed Post-EK	$6.0 \cdot 10^{7}$

As shown in the titers, the EK processing led to a loss of about three orders of magnitude. The sample run through the cascade device was processed for about half the time as the polystyrene particles, which might explain some of the sample loss. One important aspect of these results is that a dyed sample can be used (and, indeed in this case, was used) to establish a voltage scheme for bacteriophage purification and then the process can continue without labelling and still proceed with similar success. The ability to utilize this technique with an unlabeled sample after minor preliminary investigation makes it a far more potent tool for potential bacteriophage enrichment and separation.

The cascade device design is a simple way to increase separation potential by allowing for particle filtering and multiple post shapes in a connected space with control over the voltages for the individual post arrays and the design as a whole. The ability to utilize this technique with bacteriophages and other similarly valuable microorganisms, such as bacteria of similar sizes to the polystyrene particles utilized in this experiment, also makes it a powerful potential tool for biological analysis.

7 CONCLUSIONS

The three objectives presented within this document, implementation of chromatography concepts on microfluidic electrokinetic devices, empirical electrokinetic equilibrium condition, and electrokinetic cascade devices for sample filtration and separation, represent the further progress of electrokinetic techniques in microfluidic devices. These objectives also represent the bridging of concepts from outside of the microfluidics field: the well-used chromatography and separation trains that began as macroscale techniques and continue to evolve and the concept of nonlinear electrophoresis that has only recently entered into the field of electrokinetic research from the physics and math research spheres.

From implementation of chromatography concepts on microfluidic electrokinetic devices, the idea of iEK chromatography (formerly iDEP chromatography) was developed to allow for streaming separations of microscale particles in longer insulating post array. The goal was to take advantage of small differences in particle properties that add across the length of the post array to separate particle samples. A study on the geometry of insulating posts and the impact said geometry has on linear EP and DEP was performed to assess the optimal post design for separations by particle size and particle charge. Experiments were performed to enhance the mathematical model by adding required correction to the model. These corrections factor were obtained by comparing experimental particle retention times with predicted retention times. Two distinct microdevice designs were optimized for different kinds of particle separations: separations by differences in electrical charge with the Oval-250-Oval-40 design and separations by differences in size with the Oval-100-Diamond-40 design. These separations were performed using two

different 10 μm particles with a charge difference of 41.8 mV between them and two particles with a charge difference of only 4.2 mV but with sizes of 2 μm and 5.1 μm, respectively. This technique can be further exploited for different kinds of particles that need lower electric fields, especially biological particles, such as yeast and bacterial cells, that risk loss of viability when exposed to higher fields. Additional future work could include exploiting differences in particle shape to induce a separation on the long chromatography channels. Further geometry optimization that now includes nonlinear EP influence in simulations could be conducted, allowing for a more complete story of particle behavior within the chromatography channel and highlighting how the particles interact with different posts, especially asymmetric posts. The introduction of EP^3 in chromatography simulations will help to more adequately modify experimental simulations to match reality. An example of velocity profiles for particles with and without the inclusion of EP^3 is shown in Figure 7.1.

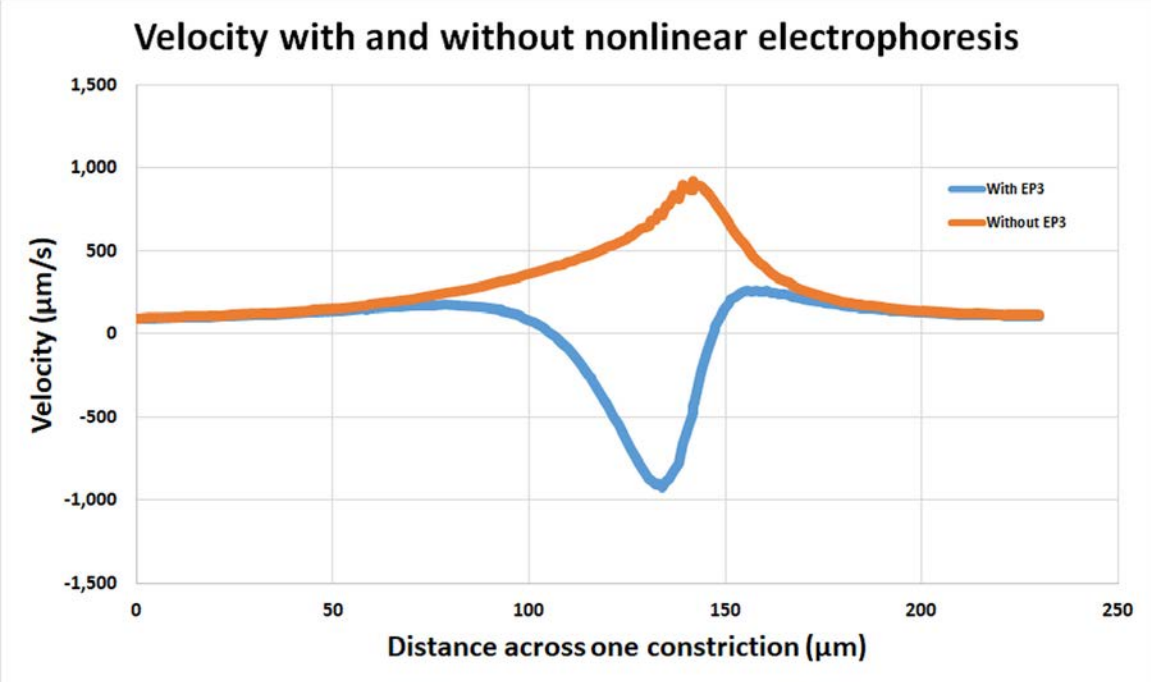

Figure 7.1 Simulated velocity of a 2 µm red carboxylated Invitrogen particle (ζ_P=-46.5 mV) immersed in a 0.2 mM K_2HPO_4 buffer. The μ_{EP^3} value for this particle in the specified buffer is -4.59·10^{-18} $\frac{m^4}{V^3 s}$. The blue line represents the total particle velocity with EP^3 included while the orange line represents the total particle velocity without EP^3 included. **Figure 4.7a** is the device design used to generate the image. 1000 V were applied to the inlet and -500 V were applied to the outlet with 0 V applied to both the sample inlet and sample outlet. The distance across one constriction begins between two post constrictions, covers the space between the post constriction, and ends at the point between the post constriction used and the next post constriction.

As demonstrated in Figure 7.1, the inclusion of the EP^3 velocity greatly impacts the velocity of the particle. With EP^3 velocity include, the total particle velocity is negative, indicating the voltage is too high for the particle once it enters the constriction, hitting zero before the particle halfway across the post. The use of a DC-biased AC field can further enhance separations in an iEK chromatography channel by strategically magnifying differences between particle electromigration velocity, allowing for successful particle separation at lower average electric fields.

The empirical electrokinetic equilibrium condition objective was borne out of the necessity to understand and quantify the newly adapted nonlinear EP term. The electrokinetic equilibrium condition was defined using postless channels and relies on low

particle concentrations and extensive experimentation and analysis. The empirical electrokinetic equilibrium condition instead takes into account particle-particle interactions and the presence of insulating posts and can be applied to trapping experiments that have previously been performed. The method relies on finding the leading edge of a band of trapped particles that represents the electric field at which the particles are trapped and using that to find the eE_{EEC} value for the particle, something that should be geometry independent but dependent on suspending media conditions. Analyzing results obtained from previous experiments led to eE_{EEC} values with low standard deviations (<10%) among species in different geometries. The technique was used to estimate trapping voltages in geometries based on average values for a bacterial species, *S. enterica*, and a bacteriophage species, SPN3US, at a prescribed distance and comparing these results to actual experimentally yielded results that, with one outlier, were all statistically similar. Finally, one potential use for this value lies in the prediction of trapping in devices without previous experiments, giving a good starting value for a stable trapping voltage that can then be utilized when trying to perform trapping experiments. Another potential application of this technique might be distinguishing eE_{EEC} values between live cells and dead cells. Live and dead cells have been shown to be separable in the past [86], [87] using iDEP. Viewing this past data through the new lens of EP^3 can help to improve understanding of the different states of microorganisms and how EP^3 might be able to separate out microorganisms by different states of development. Developing a greater understanding of E_{EEC}, eE_{EEC}, and their uses in both simulations and characterization experiments can help to expand information on microorganisms throughout the sphere of electrokinetics research and continue to improve separation techniques and simulations.

The third objective, electrokinetic cascade devices for sample filtration and separation, relies on the concept of separation trains. Essentially, a prescreening/filtering stage is first presented to help to remove contaminants and clear the way for the second stage. Once larger contaminants have been removed by the first stage, the second stage can be focused on target particle analysis, enrichment, or as a highly discriminating separation stage. While the focus of this section was separations by size, different charges should also be able to effectively sort particles within a similar array. Proving that the cascade device design led to lower sample loss than manual device transferring was an important initial step. The cascade device had a higher final sample concentration average than the manual transferring scheme by one order of magnitude, indicating that the cascade device is an effective way to help decrease sample loss. Additionally, it shows that the technique can effectively work to purify a particle sample. The primary application of this objective was the purification of bacteriophage samples. Bacteriophages are propagated in a solution containing cells and cell debris and can be difficult to purify, especially in a manner that is applicable across different bacteriophage species. Electrokinetics provides a potential solution for this problem. The cells and cell debris were effectively trapped in the initial prescreening stage while bacteriophages themselves were enriched in the second stage. A viability study was performed using PhiKZ as a representative bacteriophage and showed that dyed and undyed samples show similar results in terms of sample loss, notable because it indicates that this system can be easily used for unlabeled bacteriophage purification once an initial voltage scheme is developed. Future work for this project could include refining the geometries used in the designs, adding reservoirs for sample collection, and improving voltage schemes for a more finely tuned separation process. Possible

improvements or applications of this technique could include using a cascade device to help separate out cells in different states. The combination of this technique and the multi-part separation devices originally proposed by Gallo-Villanueva [58], [59] could actually make quite an interesting pairing, especially with changes in the vertical distance between posts. While larger particles and debris can still be trapped between normal spaces or even larger spacings between posts, separating the post array out into component parts could help to more effectively root out different distributions of bacteria or even distinguish between live and dead bacteria or bacteria in different stages of growth. Additionally, the lower the number of columns of cells, the smaller the necessary trapping voltage [88]. The combination of both concepts and the ability to carefully tailor voltages across different designs could be a more useful device overall and lead to better potential for analysis and separation. Additionally, even while releasing some trapped particles, the second array could trap larger particles at a lower voltage, yielding ordered release of particles. A proposed version of this design is presented in Figure 7.2.

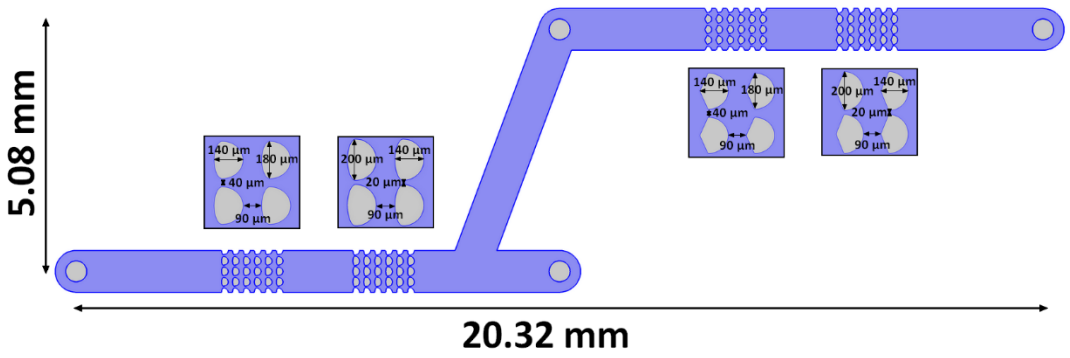

Figure 7.2 Projected design idea with separated post arrays of smaller column sizes and changes in the vertical constriction gaps widths.

In Figure 7.2, there are four post arrays with varying constriction gap sizes, 40 µm for the first design and 20 µm for the second design. The designs also reflect post geometry

choices that are more optimized for trapping, which would be necessary for biological particles to attempt to optimize viability after extraction. A device like this could potentially be used to help analyze cells in different states.

Electrokinetics is a powerful tool and continuously developing new designs to act as improved separation platforms or new understandings of fundamental theories can help the field continue to grow. The future work in this field may someday be used in medical, environmental, or agricultural testing sites and become invaluable tools in analysis and separation of microparticles.

8 BIBLIOGRAPHY

[1] G. M. Whitesides, “The origins and the future of microfluidics,” *Nature*, vol. 442, no. 7101, pp. 368–373, 2006.

[2] N. M. Jesús-Pérez and B. H. Lapizco-Encinas, “Dielectrophoretic monitoring of microorganisms in environmental applications,” *Electrophoresis*, vol. 32, no. 17, pp. 2331–2357, 2011.

[3] W. Su, X. Gao, L. Jiang, and J. Qin, “Microfluidic platform towards point-of-care diagnostics in infectious diseases,” *J. Chromatogr. A*, vol. 1377, pp. 13–26, 2015.

[4] S. Haeberle and R. Zengerle, “Microfluidic platforms for lab-on-a-chip applications,” *Lab Chip*, vol. 7, no. 9, pp. 1094–1110, 2007.

[5] S. Chakraborty, “Electrical Double Layers,” in *Encyclopedia of Microfluidics and Nanofluidics*, D. Li, Ed. Springer US, 2008, pp. 444–453.

[6] M. A. Saucedo-Espinosa and B. H. Lapizco-Encinas, “Refinement of current monitoring methodology for electroosmotic flow assessment under low ionic strength conditions,” *Biomicrofluidics*, vol. 10, no. 3, p. 033104, 2016.

[7] R. P. Oda and J. P. Landers, *Handbook of Capillary Electrophoresis*, Second. CRC Press, 1997.

[8] H. A. Pohl, “The Motion and Precipitation of Suspensoids in Divergent Electric Fields,” *J. Appl. Phys.*, vol. 22, no. 7, pp. 869–871, 1951.

[9] R. Pethig, “Review—Where Is Dielectrophoresis (DEP) Going?,” *J. Electrochem. Soc.*, vol. 164, no. 5, pp. B3049–B3055, 2017.

[10] A. Y. L. Jiang, A. R. Yale, M. Aghaamoo, D. H. Lee, A. P. Lee, T. N. G. Adams, and L. A. Flanagan, “High-throughput continuous dielectrophoretic separation of neural stem cells,” *Biomicrofluidics*, vol. 13, no. 6, p. 064111, Nov. 2019.

[11] A. R. Minerick, R. Zhou, P. Takhistov, and H. C. H.-C. Chang, “Manipulation and characterization of red blood cells with alternating current fields in microdevices,” *Electrophoresis*, vol. 24, no. 21, pp. 3703–3717, 2003.

[12] L. U. Syed, J. Liu, A. K. Price, Y. F. Li, C. T. Culbertson, and J. Li, “Dielectrophoretic capture of E. coli cells at micropatterned nanoelectrode arrays,” *Electrophoresis*, vol. 32, no. 17, pp. 2358–2365, 2011.

[13] C. J. Ramirez-Murillo, J. M. de los Santos-Ramirez, and V. H. Perez-Gonzalez, “Toward low-voltage dielectrophoresis-based microfluidic systems: A review,” *Electrophoresis*, p. elps.202000213, Nov. 2020.

[14] R. Natu, M. Islam, D. Keck, and R. Martinez-Duarte, “Automated ‘pick and transfer’ of targeted cells using dielectrophoresis,” *Lab Chip*, vol. 19, no. 15, pp. 2512–2525, 2019.

[15] H. Zhang, H. Chang, and P. Neuzil, “DEP-on-a-Chip: Dielectrophoresis Applied to Microfluidic Platforms,” *Micromachines*, vol. 10, no. 6, p. 423, Jun. 2019.

[16] A. LaLonde, A. Gencoglu, M. F. Romero-Creel, K. S. Koppula, and B. H. Lapizco-Encinas, “Effect of insulating posts geometry on particle manipulation in insulator based dielectrophoretic devices,” *J. Chromatogr. A*, vol. 1344, pp. 99–108, 2014.

[17] S. Masuda, M. Washizu, and T. Nanba, “Novel method of Cell Fusion in Field Constriction Area in Fluid Integrated Circuit,” *IEEE Trans. Ind. Appl.*, vol. 25, no. 4, pp. 732–737, 1989.

[18] E. B. Cummings and A. K. Singh, “Dielectrophoretic trapping without embedded electrodes,” in *Proceedings of SPIE*, 2000, vol. 4177, pp. 151–160.

[19] C.-P. P. Jen and W.-F. F. Chen, “An insulator-based dielectrophoretic microdevice for the simultaneous filtration and focusing of biological cells,” *Biomicrofluidics*, vol. 5, no. 4, pp. 44105–44111, 2011.

[20] H. Moncada-Hernández and B. H. Lapizco-Encinas, “Simultaneous concentration and separation of microorganisms: Insulator-based dielectrophoretic approach,” *Anal. Bioanal. Chem.*, vol. 396, no. 5, pp. 1805–1816, 2010.

[21] P. V. Jones, A. F. DeMichele, L. K. Kemp, and M. A. Hayes, “Differentiation of *Escherichia coli* serotypes using DC gradient insulator dielectrophoresis,” *Anal. Bioanal. Chem.*, vol. 406, no. 1, pp. 183–192, 2014.

[22] S. Bhattacharya, T.-C. C. Chao, N. Ariyasinghe, Y. Ruiz, D. Lake, R. Ros, and A. Ros, “Selective trapping of single mammalian breast cancer cells by insulator-based dielectrophoresis,” *Anal. Bioanal. Chem.*, vol. 406, no. 7, pp. 1855–1865, 2014.

[23] J. Gimsa, K. Titipornpun, M. Stubbe, and U. Gimsa, “Combined detection of AC-

electrokinetic effects: Experiments with three-axial chicken red blood cells," *Electrophoresis*, vol. 39, no. 17, pp. 2253–2261, Sep. 2018.

[24] A. Coll De Peña, N. H. Mohd Redzuan, M. Abajorga, N. Hill, J. A. Thomas, and B. H. Lapizco-Encinas, "Analysis of bacteriophages with insulator-based dielectrophoresis," *Micromachines*, vol. 10, no. 7, p. 450, 2019.

[25] J. Ding, R. M. Lawrence, P. V. Jones, B. G. Hogue, and M. A. Hayes, "Concentration of Sindbis virus with optimized gradient insulator-based dielectrophoresis," *Analyst*, vol. 141, no. 6, pp. 1997–2008, Mar. 2016.

[26] T. Masuda, H. Maruyama, A. Honda, and F. Arai, "Virus enrichment for single virus infection by using 3D insulator based dielectrophoresis," *PLoS One*, vol. 9, no. 6, p. e94083, 2014.

[27] A. Nakano, F. Camacho-Alanis, and A. Ros, "Insulator-based dielectrophoresis with [small beta]-galactosidase in nanostructured devices," *Analyst*, vol. 140, no. 3, pp. 860–868, Feb. 2015.

[28] A. Nakano, T.-C. C. Chao, F. Camacho-Alanis, and A. Ros, "Immunoglobulin G and bovine serum albumin streaming dielectrophoresis in a microfluidic device," *Electrophoresis*, vol. 32, no. 17, pp. 2314–2322, Jul. 2011.

[29] M. A. Mata-Gomez, V. H. Perez-Gonzalez, R. C. Gallo-Villanueva, J. Gonzalez-Valdez, M. Rito-Palomares, and S. O. Martinez-Chapa, "Modelling of electrokinetic phenomena for capture of PEGylated ribonuclease A in a microdevice with insulating structures," *Biomicrofluidics*, vol. 10, no. 3, p. 33106, 2016.

[30] B. H. Lapizco-Encinas, "Microscale electrokinetic assessments of proteins employing insulating structures," *Curr. Opin. Chem. Eng.*, vol. 29, pp. 9–16, Sep. 2020.

[31] D. F. Quevedo, C. J. Lentz, A. Coll De Peña, Y. Hernandez, N. Habibi, M. Rikako, J. Lahann, and B. H. Lapizco-Encinas, "Electrokinetic characterization of synthetic protein nanoparticles," *Beilstein J. Nanotechnol.*, vol. 11, pp. 1556–1567, 2020.

[32] J. Luo, B. G. Abdallah, G. G. Wolken, E. A. Arriaga, and A. Ros, "Insulator-based dielectrophoresis of mitochondria," *Biomicrofluidics*, vol. 8, no. 2, pp. 1–11, Mar. 2014.

[33] J. Luo, K. A. Muratore, E. A. Arriaga, and A. Ros, “Deterministic Absolute Negative Mobility for Micro- and Submicrometer Particles Induced in a Microfluidic Device,” *Anal. Chem.*, vol. 88, no. 11, pp. 5920–5927, 2016.

[34] A. Rohani, J. H. Moore, J. A. Kashatus, H. Sesaki, D. F. Kashatus, and N. S. Swami, “Label-Free Quantification of Intracellular Mitochondrial Dynamics Using Dielectrophoresis,” *Anal. Chem.*, vol. 89, no. 11, pp. 5757–5764, Jun. 2017.

[35] P. V. Jones, G. L. Salmon, and A. Ros, “Continuous Separation of DNA Molecules by Size Using Insulator-Based Dielectrophoresis,” *Anal. Chem.*, vol. 89, no. 3, pp. 1531–1539, 2017.

[36] R. C. Gallo-Villanueva, C. E. Rodríguez-López, R. I. Díaz-de-la-Garza, C. Reyes-Betanzo, and B. H. Lapizco-Encinas, “DNA manipulation by means of insulator-based dielectrophoresis employing direct current electric fields,” *Electrophoresis*, vol. 30, no. 24, pp. 4195–4205, 2009.

[37] B. Cardenas-Benitez, B. Jind, R. C. Gallo-Villanueva, S. O. Martinez-Chapa, B. H. Lapizco-Encinas, and V. H. Perez-Gonzalez, “Direct Current Electrokinetic Particle Trapping in Insulator-Based Microfluidics: Theory and Experiments,” *Anal. Chem.*, vol. 92, no. 19, pp. 12871–12879, Sep. 2020.

[38] S. Tottori, K. Misiunas, U. F. Keyser, and D. J. Bonthuis, “Nonlinear Electrophoresis of Highly Charged Nonpolarizable Particles,” *Phys. Rev. Lett.*, vol. 123, no. 1, p. 14502, Jul. 2019.

[39] A. Coll De Peña, A. Miller, C. J. Lentz, N. Hill, A. Parthasarathy, A. O. Hudson, and B. H. Lapizco-Encinas, “Creation of an electrokinetic characterization library for the detection and identification of biological cells,” *Anal. Bioanal. Chem.*, vol. 412, no. 16, pp. 3935–3945, 2020.

[40] A. Coll De Peña, N. Hill, and B. H. Lapizco-Encinas, “Determination of the Empirical Electrokinetic Equilibrium Condition of Microorganisms in Microfluidic Devices,” *Biosensors*, vol. 10, no. 10, p. 148, Oct. 2020.

[41] S. Antunez-Vela, V. H. Perez-Gonzalez, A. Coll De Peña, C. J. Lentz, and B. H. Lapizco-Encinas, “Simultaneous Determination of Linear and Nonlinear Electrophoretic Mobilities of Cells and Microparticles,” *Anal. Chem.*, vol. 92, no. 22, pp. 14885–14891, Oct. 2020.

[42] S. S. Dukhin, “Electrokinetic phenomena of the second kind and their applications,” *Adv. Colloid Interface Sci.*, vol. 35, no. C, pp. 173–196, 1991.

[43] O. Schnitzer, R. Zeyde, I. Yavneh, and E. Yariv, “Weakly nonlinear electrophoresis of a highly charged colloidal particle,” *Phys. Fluids*, vol. 25, no. 5, p. 052004, May 2013.

[44] O. Schnitzer and E. Yariv, “Nonlinear electrophoresis at arbitrary field strengths: Small-Dukhin-number analysis,” *Phys. Fluids*, vol. 26, no. 12, p. 122002, Dec. 2014.

[45] J. G. Dorsey, “Introduction to Modern Liquid Chromatography, 3rd ed,” *J. Am. Chem. Soc.*, vol. 132, no. 26, p. 9220, Jul. 2010.

[46] M. G. Cikalo, K. D. Bartle, M. M. Robson, P. Myers, and M. R. Euerby, “Capillary electrochromatography . Tutorial Review,” *Analyst*, vol. 123, no. 7, pp. 87R-102R, 1998.

[47] V. Calero, P. Garcia-Sanchez, C. Honrado, A. Ramos, and H. Morgan, “AC electrokinetic biased deterministic lateral displacement for tunable particle separation,” *Lab Chip*, vol. 19, no. 8, pp. 1386–1396, Apr. 2019.

[48] V. Calero, P. Garcia-Sanchez, A. Ramos, and H. Morgan, “Combining DC and AC electric fields with deterministic lateral displacement for micro- And nano-particle separation,” *Biomicrofluidics*, vol. 13, no. 5, p. 054110, Sep. 2019.

[49] V. Calero, P. García-Sánchez, A. Ramos, and H. Morgan, “Electrokinetic biased deterministic lateral displacement: scaling analysis and simulations,” *J. Chromatogr. A*, vol. 1623, p. 461151, May 2020.

[50] M. Aghaamoo, A. Aghilinejad, X. Chen, and J. Xu, “On the design of deterministic dielectrophoresis for continuous separation of circulating tumor cells from peripheral blood cells,” *Electrophoresis*, vol. 40, no. 10, pp. 1486–1493, May 2019.

[51] O. Kurosawa, S. Suzuki, T. Nishizaka, T. Shinohara, M. Washizu, S. Suzuki, O. Kurosawa, T. Nishizaka, and T. Shinohara, “Molecular Dielectrophoresis of Biopolymers,” *IEEE Trans. Ind. Appl.*, vol. 30, no. 4, pp. 835–843, 1994.

[52] D. Holmes and H. Morgan, “Dielectrophoretic Chromatography of Cells,” in *Micro Total Analysis Systems 2002*, Y. Baba, S. Shoji, and A. Berg, Eds. Springer

Netherlands, 2002, pp. 829–831.

[53] M. Hakoda and T. Otaki, “Analytical Characteristic of Chromatography Device Using Dielectrophoresis Phenomenon,” in *Silicon Science and Advanced Micro-Device Engineering II*, 2012, vol. 497, pp. 87–92.

[54] Y. Umezawa, O. Kobayashi, S. Kanai, and M. Hakoda, “Development of Particle Packed Bed Type Chromatography Using Dielectrophoresis,” *Key Eng. Mater.*, vol. 534, pp. 88–92, 2013.

[55] J. Giesler, G. R. Pesch, L. Weirauch, M.-P. Schmidt, J. Thöming, and M. Baune, “Polarizability-Dependent Sorting of Microparticles Using Continuous-Flow Dielectrophoretic Chromatography with a Frequency Modulation Method,” *Micromachines*, vol. 11, no. 1, p. 38, Dec. 2020.

[56] E. Marcoulaki, P. Linke, and A. Kokossis, “Design of Separation Trains and Reaction-Separation Networks Using Stochastic Optimization Methods,” *Chem. Eng. Res. Des.*, vol. 79, no. 1, pp. 25–32, 2001.

[57] F. Yang, X. Yang, H. Jiang, and G. Wang, “Cascade and staggered dielectrophoretic cell sorters,” *Electrophoresis*, vol. 32, no. 17, pp. 2377–2384, 2011.

[58] R. C. Gallo-Villanueva, V. H. Pérez-González, R. V. Davalos, and B. H. Lapizco-Encinas, “Separation of mixtures of particles in a multipart microdevice employing insulator-based dielectrophoresis,” *Electrophoresis*, vol. 32, no. 18, pp. 2456–2465, 2011.

[59] S. Ayala-Mar, V. H. Perez-Gonzalez, M. A. Mata-Gómez, R. C. Gallo-Villanueva, and J. Gonzalez-Valdez, “Electrokinetically driven exosome separation and concentration using dielectrophoretic-enhanced PDMS-based microfluidics,” *Anal. Chem.*, vol. 91, no. 23, pp. 14975–14982, 2019.

[60] A. Lalonde, M. F. Romero-Creel, and B. H. Lapizco-Encinas, “Assessment of cell viability after manipulation with insulator-based dielectrophoresis,” *Electrophoresis*, vol. 36, no. 13, pp. 1479–1484, 2015.

[61] R. F. Probstein, *Physicochemical Hydrodynamics: An Introduction*, Second. John Wiley & Sons, Ltd, 1994.

[62] N. G. Weiss, P. V. Jones, P. Mahanti, K. P. Chen, T. J. Taylor, and M. A. Hayes,

"Dielectrophoretic mobility determination in DC insulator-based dielectrophoresis," *Electrophoresis*, vol. 32, no. 17, pp. 2292–2297, 2011.

[63] T. Honegger, K. Berton, E. Picard, and D. Peyrade, "Determination of Clausius–Mossotti factors and surface capacitances for colloidal particles," *Appl. Phys. Lett.*, vol. 98, no. 18, p. 181906, 2011.

[64] T. Honegger, K. Berton, E. Picard, and D. Peyrade, "Determination of Clausius–Mossotti factors and surface capacitances for colloidal particles," *Appl. Phys. Lett.*, vol. 98, no. 18, p. 181906, 2011.

[65] N. Hill and B. H. Lapizco-Encinas, "On the use of correction factors for the mathematical modeling of insulator based dielectrophoretic devices," *Electrophoresis*, vol. 40, no. 18–19, pp. 2541–2552, 2019.

[66] E. B. Cummings and A. K. Singh, "Dielectrophoresis in microchips containing arrays of insulating posts: Theoretical and experimental results," *Anal. Chem.*, vol. 75, no. 18, pp. 4724–4731, 2003.

[67] N. Hill and B. H. Lapizco-Encinas, "Continuous flow separation of particles with insulator-based dielectrophoresis chromatography," *Anal. Bioanal. Chem.*, vol. 412, no. 16, pp. 3891–3902, Jun. 2020.

[68] J. Beckman, Y. Song, Y. Gu, S. Voronov, N. Chennamsetty, S. Krystek, N. Mussa, and Z. J. Li, "Purity Determination by Capillary Electrophoresis Sodium Hexadecyl Sulfate (CE-SHS): A Novel Application For Therapeutic Protein Characterization," *Anal. Chem.*, vol. 90, no. 4, pp. 2542–2547, Feb. 2018.

[69] L. Leclercq, M. Morvan, J. Koch, C. Neusüß, and H. Cottet, "Modulation of the electroosmotic mobility using polyelectrolyte multilayer coatings for protein analysis by capillary electrophoresis," *Anal. Chim. Acta*, vol. 1057, pp. 152–161, 2019.

[70] M. A. Saucedo-Espinosa and B. H. Lapizco-Encinas, "Design of insulator-based dielectrophoretic devices: Effect of insulator posts characteristics," *J. Chromatogr. A*, vol. 1422, pp. 325–333, 2015.

[71] J. A. Thomas, M. R. Rolando, C. A. Carroll, P. S. Shen, D. M. Belnap, S. T. Weintraub, P. Serwer, and S. C. Hardies, "Characterization of Pseudomonas chlororaphis myovirus 201phi2-1 via genomic sequencing, mass spectrometry, and

electron microscopy," *Virology*, vol. 376, no. 2, pp. 330–338, 2008.

[72] E. Lecoutere, P. J. Ceyssens, K. A. Miroshnikov, V. V. Mesyanzhinov, V. N. Krylov, J. P. Noben, J. Robben, K. Hertveldt, G. Volckaert, and R. Lavigne, "Identification and comparative analysis of the structural proteomes of φKZ and EL, two giant Pseudomonas aeruginosa bacteriophages," *Proteomics*, vol. 9, no. 11, pp. 3215–3219, 2009.

[73] B. Ali, M. I. Desmond, S. A. Mallory, A. D. Benítez, L. J. Buckley, S. T. Weintraub, M. V. Osier, L. W. Black, and J. A. Thomas, "To be or not to be T4: Evidence of a complex evolutionary pathway of head structure and assembly in giant Salmonella virus SPN3US," *Front. Microbiol.*, vol. 8, no. NOV, p. 2251, Nov. 2017.

[74] M. A. Saucedo-Espinosa and B. H. Lapizco-Encinas, "Experimental and theoretical study of dielectrophoretic particle trapping in arrays of insulating structures: Effect of particle size and shape," *Electrophoresis*, vol. 36, no. 9–10, pp. 1086–1097, 2015.

[75] S. S. Dukhin, "Electrokinetic phenomena of the second kind and their applications," *Adv. Colloid Interface Sci.*, vol. 35, pp. 173–196, 1991.

[76] M. A. Saucedo-Espinosa and B. H. Lapizco-Encinas, "Exploiting Particle Mutual Interactions To Enable Challenging Dielectrophoretic Processes," *Anal. Chem.*, vol. 89, no. 16, pp. 8459–8467, Aug. 2017.

[77] P. Serwer, S. J. Hayes, S. Zaman, K. Lieman, M. Rolando, and S. C. Hardies, "Improved isolation of undersampled bacteriophages: finding of distant terminase genes," *Virology*, vol. 329, no. 2, pp. 412–424, 2004.

[78] Y. Yuan and M. Gao, "Jumbo Bacteriophages: An Overview," *Jumbo Bacteriophages An Overview. Front. Microbiol*, vol. 8, p. 403, 2017.

[79] R. W. Hendrix, "Jumbo Bacteriophages," in *Lesser Known Large dsDNA Viruses*, J. L. Van Etten, Ed. Berlin, Heidelberg: Springer Berlin Heidelberg, 2009, pp. 229–240.

[80] V. Krylov, M. Bourkaltseva, E. Pleteneva, O. Shaburova, S. Krylov, A. Karaulov, S. Zhavoronok, O. Svitich, and V. Zverev, "Phage phiKZ-The First of Giants," *Viruses*, vol. 13, no. 2, p. 149, Jan. 2021.

[81] V. V Mesyanzhinov, J. Robben, B. Grymonprez, V. A. Kostyuchenko, M. V Bourkaltseva, N. N. Sykilinda, V. N. Krylov, and G. Volckaert, “The genome of bacteriophage φKZ of Pseudomonas aeruginosa,” *J. Mol. Biol.*, vol. 317, no. 1, pp. 1–19, 2002.

[82] A. Fokine, A. J. Battisti, V. D. Bowman, A. V Efimov, L. P. Kurochkina, P. R. Chipman, V. V Mesyanzhinov, and M. G. Rossmann, “Cryo-EM Study of the Pseudomonas Bacteriophage φKZ,” *Structure*, vol. 15, no. 9, pp. 1099–1104, Sep. 2007.

[83] J. B. Heymann, B. Wang, W. W. Newcomb, W. Wu, D. C. Winkler, N. Cheng, E. R. Reilly, R.-C. Hsia, J. A. Thomas, and A. C. Steven, “The Mottled Capsid of the Salmonella Giant Phage SPN3US, a Likely Maturation Intermediate with a Novel Internal Shell,” *Viruses*, vol. 12, no. 9, p. 910, Aug. 2020.

[84] R. Monson, I. Foulds, J. Foweraker, M. Welch, and G. P. C. Salmond, “The Pseudomonas aeruginosa generalized transducing phage φPA3 is a new member of the φKZ-like group of ‘jumbo’ phages, and infects model laboratory strains and clinical isolates from cystic fibrosis patients,” *Microbiology*, vol. 157, no. 3, pp. 859–867, 2011.

[85] J. A. Thomas, A. D. Benítez Quintana, M. A. Bosch, A. Coll De Peña, E. Aguilera, A. Coulibaly, W. Wu, M. V. Osier, A. O. Hudson, S. T. Weintraub, and L. W. Black, “Identification of Essential Genes in the *Salmonella* Phage SPN3US Reveals Novel Insights into Giant Phage Head Structure and Assembly,” *J. Virol.*, vol. 90, no. 22, pp. 10284–10298, 2016.

[86] B. H. Lapizco-Encinas, B. A. Simmons, E. B. Cummings, and Y. Fintschenko, “Dielectrophoretic Concentration and Separation of Live and Dead Bacteria in an Array of Insulators,” *Anal. Chem.*, vol. 76, no. 6, pp. 1571–1579, 2004.

[87] C.-P. Jen and T.-W. Chen, “Selective trapping of live and dead mammalian cells using insulator-based dielectrophoresis within open-top microstructures,” *Biomed. Microdevices*, vol. 11, no. 3, pp. 597–607, 2009, [Online]. Available: http://dx.doi.org/10.1007/s10544-008-9269-1 DO - 10.1007/s10544-008-9269-1.

[88] V. H. Perez-Gonzalez, R. C. Gallo-Villanueva, B. Cardenas-Benitez, S. O. Martinez-Chapa, and B. H. Lapizco-Encinas, “Simple Approach to Reducing

Particle Trapping Voltage in Insulator-Based Dielectrophoretic Systems,” *Anal. Chem.*, vol. 90, no. 7, pp. 4310–4315, 2018.

Figure Reprint Permissions

All figure reprint permissions are available upon request.

APPENDIX A: COMSOL MODELING

A.1 EQUATIONS AND BOUNDARY CONDITIONS

The COMSOL models used are two-dimensional models with the electric current module under AC/DC physics. The studies performed are stationary. Meshes were user defined, defined for fluid dynamics, had a minimum resolution of the narrow regions of 10, and the Laplace equation was employed to describe the distribution of the electric potential across the microchannel:

$$\nabla^2 \phi = 0 \quad \text{(A.1)}$$

where ϕ is the electric potential. The boundary conditions considered are as follows:

$$\vec{n} \cdot \vec{J} = 0 \quad \text{(A.2)}$$

$$\phi = V_{reservoir} \quad \text{(A.2)}$$

where $\vec{n}$ is the vector normal to the surface, $\vec{J}$ is the electric current density, and $V_{reservoir}$ represents the electrical potential applied to any given reservoir in the designs. The boundaries considered are the sections containing PDMS, the channel walls and the insulating posts. A relative permittivity of 78.4 was applied to every model. The electrical conductivity matched the conductivity of the suspending media. The PDMS is considered to be non-conductive for these experiments. An example of the boundary conditions is shown in Figure A.1.

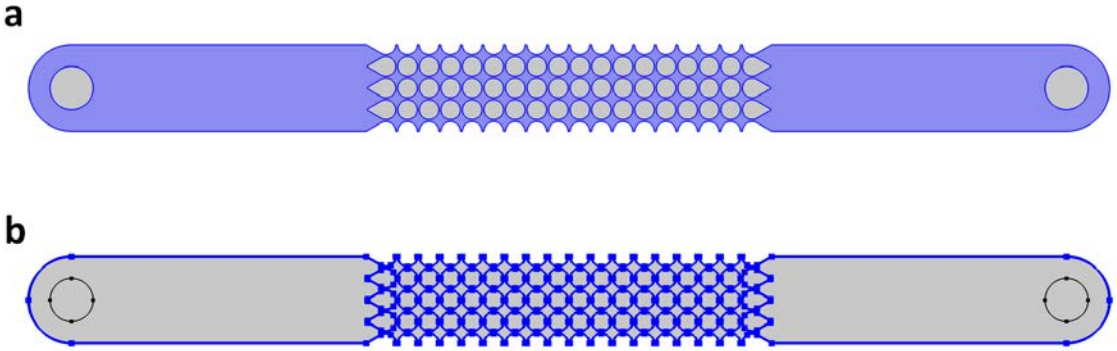

Figure A.1 Boundary condition illustration of the channel. **a** The purple color represents the media and the section of the design through which electric currents are able to travel. **b** The blue lines represent electrical insulation. The areas outlined in blue are considered insulating so only the areas outside of the posts can allow for the passage of current. The black outlines represent the inlet and outlet of the design where the electric potential and ground are applied.

Figure A.1 shows a visual representation of the boundaries present in the COMSOL simulations. While there are several different device designs simulated, all follow the same boundaries. The media fills all the space outside of the posts and the reservoirs (Fig. A.1a). The posts and channel walls, outlined in blue, are all considered insulators (Fig. A.1b). The reservoirs represent where the electric potential is allowed to contact the media.

A.2 PARAMETERS AND VARIABLES FILES USED

Parameter and variable files for the chromatography project

Table A.1 Chromatography COMSOL parameters. Please note that the lengths for the constriction and array, zeta potential of the particle, and the size of the particle all varied by geometry of the posts and particle properties. Correction factor value is set at 1 as a default.

Parameter	Value	Description
c	1	Correction Factor
LC	290[um]	Constriction Length
LA	25340[um]	Length of the post array
VAin	900[V]	Voltage at inlet
VBin	750[V]	Voltage at sample inlet
VCin	0[V]	Voltage at outlet
cmf	-0.5	Clausius Mossotti Factor
eo	8.854e-12[F/m]	Permittivity of free space
dp	5e-6[m]	Diameter of particle
zeta_wall	-93.93[mV]	Zeta potential for Wall
zeta_particle	-55.186[mV]	Zeta potential for Particle
rp	dp/2	Radius of particle
vis	8.91e-4[kg/(m*s)]	Viscosity of medium
em	78.4	Permittivity of medium
mobEP	zeta_particle*em*eo/vis	EP mobility
mobEOF	-zeta_wall*em*eo/vis	EOF mobility
mobEK EK mobility	mobEP+mobEOF	EK mobility
mobDEP	rp^2*em*eo*cmf/(3*vis)	DEP mobility

Table A.2 Chromatography COMSOL variables.

Variable	Equation	Description
EE	ec.Ex^2+ec.Ey^2	E point product
gradEE_x	d(EE,x)	Gradient of E point product, x component
gradEE_y	d(EE,y)	Gradient of E point product, y component
gradEE	sqrt(gradEE_x^2+gradEE_y^2)	Gradient of E point product, norm
vEK_x	mobEK*ec.Ex	EK velocity, x component
vEK_y	mobEK*ec.Ey	EK velocity, y component
vEK	sqrt(vEK_x^2+vEK_y^2)*abs(vEK_x)/vEK_x	EK velocity, norm
vDEP_x	mobDEP*gradEE_x	DEP velocity, x component
vDEP_y	mobDEP*gradEE_y	DEP velocity, y component
vDEP	sqrt(vDEP_x^2+vDEP_y^2)*abs(vDEP_x)/vDEP_x	DEP velocity, norm
TC	(vDEP_x*ec.Ex+vDEP_y*ec.Ey)/(vEK_x*ec.Ex+vEK_y*ec.Ey)	Trapping condition
vEP_x	mobEP*ec.Ex	vEP x
vEP_y	mobEP*ec.Ey	vEP y
vEP	sqrt(vEP_x^2+vEP_y^2)*abs(vEP_x)/vEP_x	vEP
vEOF_x	mobEOF*ec.Ex	vEOF x
vEOF_y	mobEOF*ec.Ey	vEOF y
vEOF	sqrt(vEOF_x^2+vEOF_y^2)*abs(vEOF_x)/vEOF_x	vEOF
vT	sqrt((vDEP_x+vEK_x)^2+(vDEP_y+vEK_y)^2)*abs(vDEP_x+vEK_x)/(vDEP_x+vEK_x)	Total velocity

Parameter and variable files for the empirical electrokinetic equilibrium condition project

Table A.3 The eE_{EEC} COMSOL parameters.

Parameter	Value	Description
Vin	1200[V]	Voltage @inlet
eps0	8.854e-12[F/m]	Permittivity of free space
vis	8.91e-4[kg/m/s]	Viscosity of medium
epsm	78.4	Permittivity of medium

Table A.4 The eE_{EEC} COMSOL variables.

Variable	Equation	Description
E3	(ec.normE)^3	E^3

Parameter for the cascade project

Table A.5 Cascade COMSOL parameter.

Parameter	Value	Description
Vin	900[V]	Voltage @ inlet

There were no variables, only built-in COMSOL functions were used.

Parameter and variable files for EP^3 simulation

Table A.6 EP^3 COMSOL parameters.

Parameter	Value	Description
cmf	cmf -0.5	Clausius Mossotti Factor for DC Signal
eo	8.854e-12[F/m]	Permittivity of free space
vis	8.91e-4[kg/(m*s)]	Viscosity of medium
em	78.4	Permittivity of medium
zw	-60.12[mV]	Zeta potential for Wall
zp1	-46.48[mV]	Zeta potential for p1
dp1	5.1[um]	Diameter of p1
rp1	dp1/2	Radius of p1
mEOF	-zw*em*eo/vis	EOF mobility
mEP1p1	zp1*em*eo/vis	EP1 Mobility for p1
mEP3p1	-4.59269004738406e-18[m^4/(V^3*s)]	EP3 Mobility for p1
mDEPp1	rp1^2*em*eo*cmf/(3*vis)	DEP mobility for p1
V1	0[V]	Voltage at North Electrode
V2	1000[V]	Voltage at West Electrode
V3	0[V]	Voltage at South Electrode
V4	-500[V]	Voltage at East Electrode

Table A.7 EP^3 COMSOL variables.

Variable	Equation	Description
VEOFx	mEOF*ec.Ex	x component of EOF velocity
VEOFy	mEOF*ec.Ey	y component of EOF velocity
VEOF	sqrt(VEOFx^2+VEOFy^2)*abs(VEOFx)/VEOFx	EOF Vel
VEP1p1x	mEP1p1*ec.Ex	x component of EP vel p1
VEP1p1y	mEP1p1*ec.Ey	y component of EP vel p1
VEP1p1	sqrt(VEP1p1x^2+VEP1p1y^2)*abs(VEP1p1x)/VEP1p1x	EP1 Vel p1
VEP3p1x	mEP3p1*(ec.Ex)^3	x component of EP3 vel p1
VEP3p1y	mEP3p1*(ec.Ey)^3	y component of EP3 vel p1
VEP3p1	sqrt(VEP3p1x^2+VEP3p1y^2)*abs(VEP3p1x)/VEP3p1x	EP3 Vel p1
VDEPp1x	mDEPp1*gradE2x	x component of DEP vel p1
VDEPp1y	mDEPp1*gradE2y	y component of DEP vel p1
VDEPp1	sqrt(VDEPp1x^2+VDEPp1y^2)*abs(VDEPp1x)/VDEPp1x	DEP Vel p1
gradE2x	d(ec.normE*ec.normE,x)	x component of Grad(E.E)
gradE2y	d(ec.normE*ec.normE,y)	y component of Grad(E.E)
gradE2	sqrt(d(ec.normE*ec.normE,x)^2+d(ec.normE*ec.normE,y)^2)	Grad(E.E)
VPp1x	VEOFx+VEP1p1x+ VEP3p1x+VDEPp1x	x component of total vel p1
VPp1y	VEOFy+VEP1p1y+ VEP3p1y+VDEPp1y	y component of total vel p1
VPp1	sqrt(VPp1x^2+VPp1y^2)*abs(VPp1x)/VPp1x	Total vel p1

A.3 FIGURES EXTRACTED FROM MODELS IN THE THESIS BODY

There are several figures that have images extracted from COMSOL, but all of these images only use the COMSOL interface to generate the design. These images include Figure 1.2, Figure 4.2, Figure 4.6a, Figure 4.7a, Figures 5.3b-5.3d, Figure 6.1, Figure 6.3b, and Figure 7.2. As these images do not rely on anything more than importing into COMSOL and extracting the image of an imported structure, they are not included in this list.

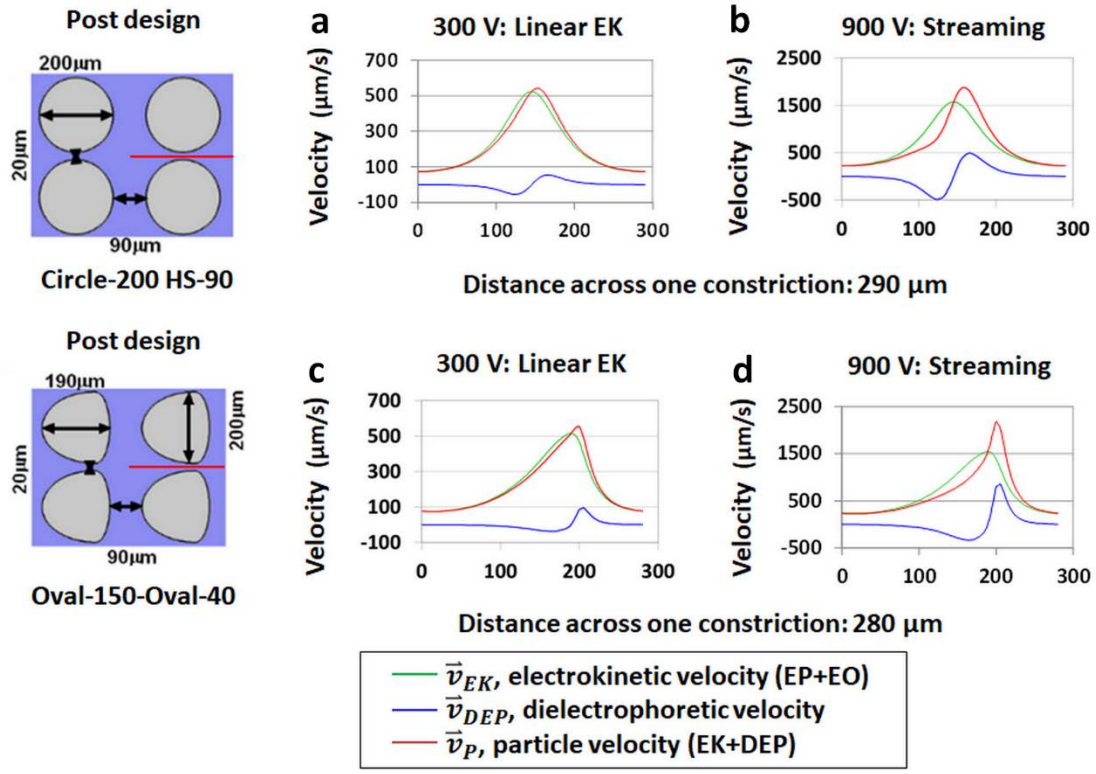

Figure A.2 Originally Figure 4.3, this figure relies on the parameter and variable files for the chromatography project. A cutline is drawn as shown in the figure for a post in the center of the post array. The velocity values were generated using a line plot that simulated the relevant velocities at the given voltages.

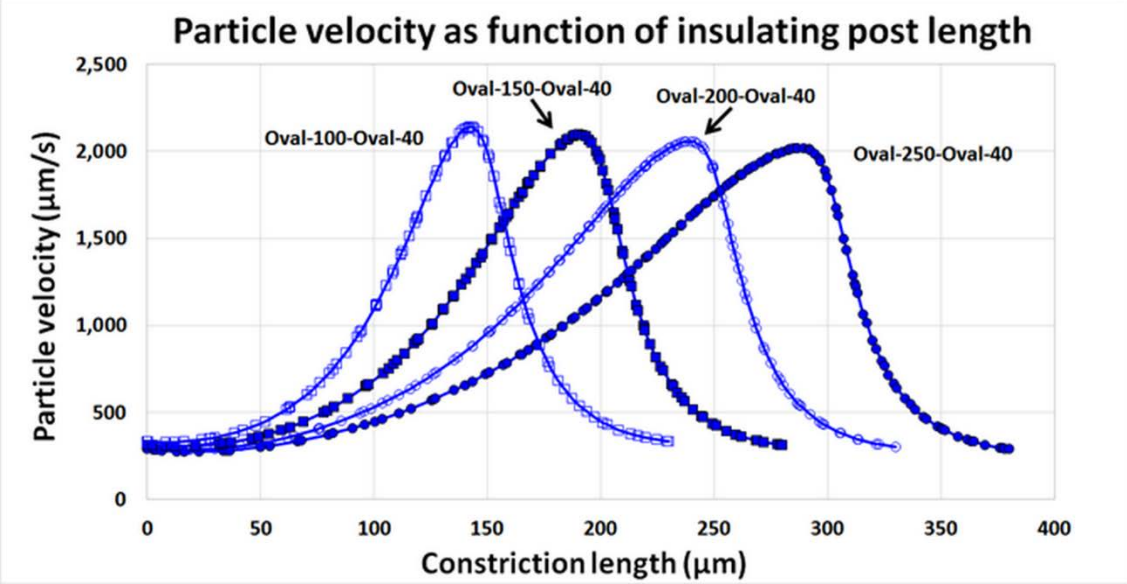

Figure A.3 Originally Figure 4.4, this figure relies on the parameter and variable files for the chromatography project. A cutline is drawn as shown in the figure for a post in the center of the post array. The velocity values were generated using a line plot that simulated the relevant velocities for each post design with 900 V applied to the main inlet.

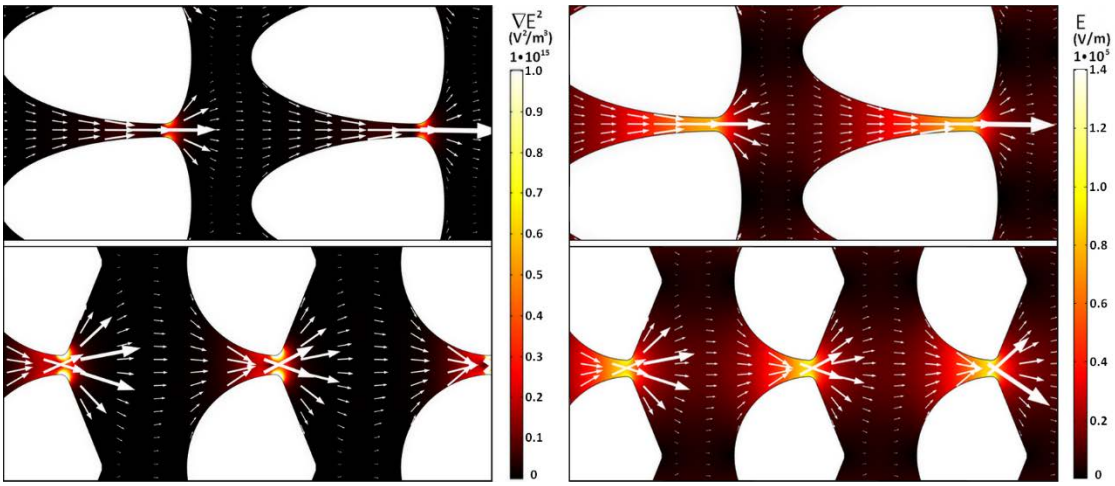

Figure A.4 Originally Figure 4.5, this figure relies on the parameter and variable files for the chromatography project. The gradient of the electric field squared, variable gradEE, and the electric field, a built-in COMSOL function, were plotted on a surface plot. The arrows represent the total particle velocity at the given points.

Table A.8 Originally Table 4.1, the predicted retention time values in this table rely on the parameter and variable files for the chromatography project. Retention time values were calculated by dividing the length of the post array by the total particle velocity average, found by creating a cutline across the entire post array and using the line average derived value.

#	Particle, brand, surface functionalization	ζ_P (mV)	Predicted t_R (s)	Experimental $t_{R,e}$ (s)	Separation efficiency (N/m)	Correction factor (c)
1	**1.1 µm, Magsphere, Non-functionalized**	-61.4	41.8	43.9±2.0	3,968±584	171.0
2	**2 µm, Magsphere, Non-functionalized**	-39.4	25.9	72.3±10.5	1,890±156	149.0
3	**2 µm, Magsphere, Carboxylated**	-57.5	32.1	35.1±2.9	7,734±1,405	84.0
4	**2 µm, Magsphere, Carboxylated**	-63.8	44.8	61.9±5.1	3,865±622	81.0
5	**5 µm, Magsphere, Carboxylated**	-53.8	34.5	40.4±4.1	24,799± 3617	15.0
6	**5 µm, Magsphere, Non-functionalized**	-61.7	42.1	45.0±1.8	20,459±797	9.1
7	**6.8 µm, Magsphere, Carboxylated**	-50.0	31.7	35.2±2.5	8,671±1,621	8.0
8	**7.6 µm, Magsphere, Carboxylated**	-12.4	22.6	42.9±1.9	61,934± 2,964	15.1
9	**9.7 µm, Magsphere, Carboxylated**	-30.8	17.7	52.7±6.8	27,656± 7,178	7.3
10	**10 µm, Invitrogen, Carboxylated**	-72.6	72.7	100.4±3.3	153,724± 9,226	2.5

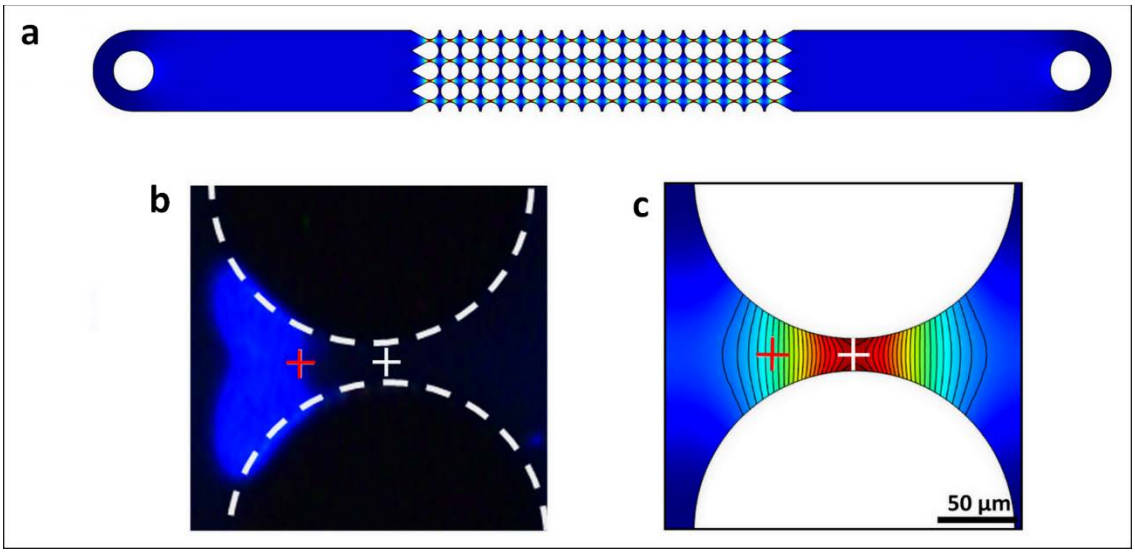

Figure A.5 Originally Figure 5.2, this figure relies on the parameter and variable files for the empirical electrokinetic equilibrium condition project. A voltage of 1000 V was applied to the inlet reservoir and the graph represents the electric field applied across the channel. The contour plot is applied to the same expression as the surface plot.

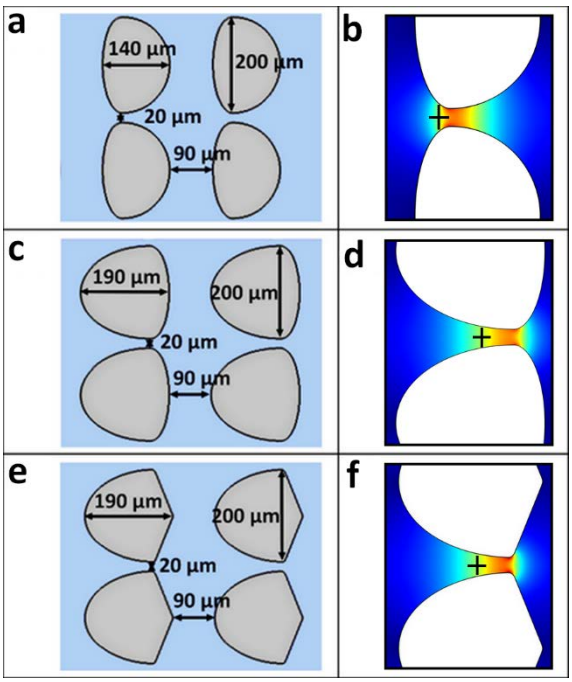

Figure A.6 Originally Figure 5.7, this figure relies upon the parameter and variable files for the empirical electrokinetic equilibrium condition. A voltage sweep was performed across a range of voltages for one particular cut point, marked by the black crosses on the figure. While the voltage is nonlinear across the post constriction, at one particular point the rise in voltage is linear. This means that, as long as all electric field readings at each voltage in the sweep are performed at the same point, the value for eE_{EEC} can be linearly interpreted.

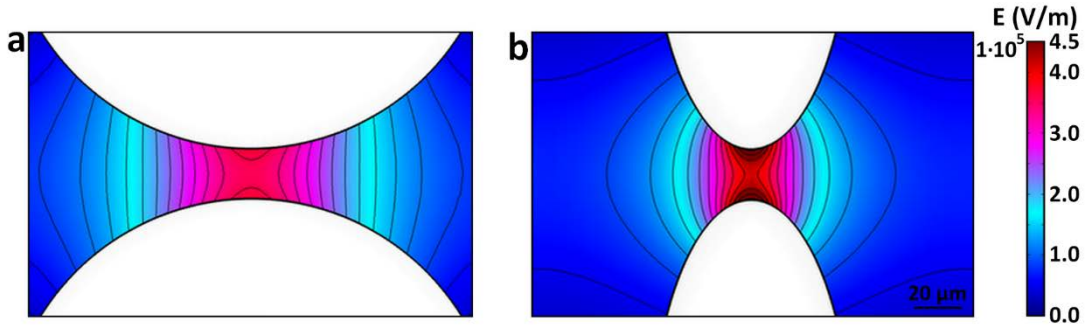

Figure A.7 Originally Figure 6.2, this figure relies upon only a single parameter: Vin, set to 900 V here. The electric field was simulated with a surface plots as were the electric field contours, all built-in COMSOL functions.

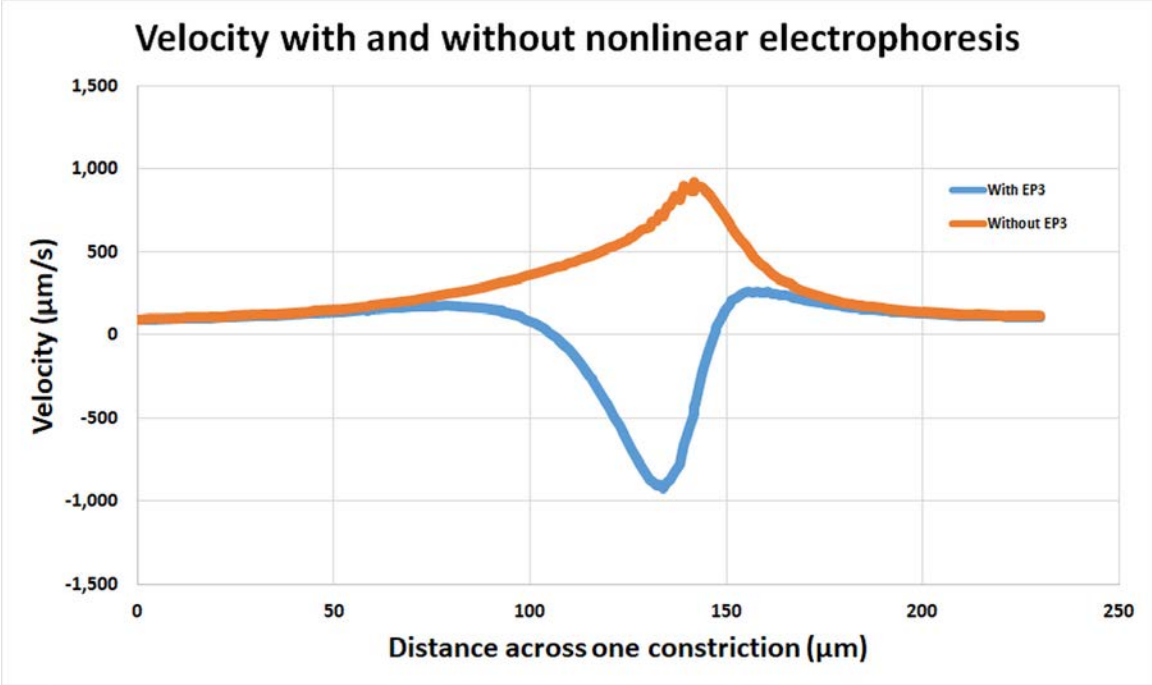

Figure A.8 Originally Figure 7.1, this figure relies upon the parameter and variable files for EP^3 simulation. The velocity of a 2 µm red carboxylated Invitrogen particle (ζ_P=-46.5 mV) immersed in a 0.2 mM K_2HPO_4 buffer is simulated across the post constriction for the left-most column of posts. A line plot simulating the total particle velocity both including and not including EP^3 were generated and the data was exported to form the plots.

APPENDIX B: EXPERIMENTAL PROTOCOLS

B.1 FLUORESCENT LABELING PROTOCOL FOR VIRUSES

1. Inject the desired amount of sample into an Eppendorf tube using sterile pipette tips. Note: the amount of sample is going to be three times the final amount desired. For instance, if the final desired amount is 300 µL, the initial sample amount is 900 µL.

2. Place the sample into a centrifuge with an appropriate counterbalance. Run the centrifuge for 10 minutes at 13,000 rpm.

3. Remove samples from the centrifuge and remove the supernatant without disturbing the pellet. Dispose of the supernatant and tips in the appropriate biological waste containers.

4. Resuspend the sample in an amount of fluid equal to the final desired concentration using sterile DI water and vortex the samples for no more than five seconds.

5. Centrifuge again with appropriate counterbalances for 10 minutes at 13,000 rpm.

6. Remove the supernatant and resuspend in 500 µL of sterile DI water. This amount is constant. Wear an extra pair of gloves and add 3 µL of the desired nucleic acid stain to the solution. Vortex for 5 seconds.

7. Wrap the sample in foil and let it sit in a dark, dry, room temperature space for 20 minutes.

8. Centrifuge the samples at 13,000 rpm for 10 minutes.

9. Remove the supernatant and resuspend using desired media with the desired final amount.

10. Wrap the sample in foil. The sample needs to be used within the next two days. The sample should have minimum exposure to light.

B.2 CURRENT MONITORING PROTOCOL

Device fabrication

1. For the creation of the device, mix 30 grams of PDMS with 3 grams of curing agent. Cover the current monitoring mold with a thin layer of PDMS, just enough to coat the surface of the device.

2. Heat the device thin layer for 30 minutes at 85°C.

3. Use sample tubes, such as Eppendorf tubes, of at least 1.5 mL to create the reservoirs. Cut off the cap and the end of the tube.

4. Place the large reservoirs on the PDMS coat. They should preferably be placed in such a way that the center of the outer channel reservoirs are in the center of the reservoir.

5. Pour the remainder of the PDMS onto the device, being careful not to pour any inside of the reservoirs. Heat the device for 40 minutes at 85°C and then for 5 minutes at 135°C.

6. Remove the device and use 2 mm biopsy punch to punch out the reservoir. Plasma bond the device to a PDMS-covered glass wafer.

7. Soak the device in the desired media for at least 18 hours.

Current monitoring experiments

1. Create a 90% solution of the media, that is one part water to nine parts media. At least 50 mL is needed.

2. Place at least three positive electrodes and their corresponding negative electrodes in the channels. Our group has a device with one electrode cable split into three electrodes. This is necessary to decrease sample noise.

3. Apply 1000 V across the channels and trace the corresponding voltage and currents over time. Apply the voltage until the current values reach a relative plateau with minimum differences between the values.

4. Stop the voltage, remove the positive electrodes, and remove the liquid from the reservoirs that held the positive electrodes.

5. Quickly fill the reservoirs with the 90% solution, place the positive electrodes back into the device, and apply the 1000 V again.

6. Apply the voltage until a new plateau is reached. This plateau should be smaller than the previous value.

7. Stop the voltage application and stop the tracing process. Dump the liquid in the device and refill the device with the media. Wait at least five minutes before performing another trial.

B.3 LOW VOLTAGE PARTICLE IMAGE VELOCIMETRY PROTOCOL

1. Using a PIV device (postless channel), inject 1 µL of a low concentration particle solution into the inlet reservoir of the device.

2. Place the positive electrode in the inlet and negative electrode in the outlet of the device and balance the pressure in the device with media until minimum particle movement is observed.

3. Apply 50 V for 15 seconds. If the particle movement is too minimal to be observed and only in this case, increase the starting voltage to 100 V. If any particle movement is observed which does not appear linear, such as particles moving in a wave-like pattern, then start the process in a new channel.

4. Apply 100 V (or higher if needed) for 15 seconds.

5. Apply 150 V (or higher if needed) for 15 seconds.

6. Repeat at least three times in a random order.

B.4 RETENTION TIME EXPERIMENTAL PROTOCOL

1. Inject a 10 µL sample of highly concentrated particles into the sample inlet for the iEK chromatography channel of choice.

2. Inject a plug of particles into the post array. EK injection should be performed if necessary, but a combination of careful pressure balancing and well-chosen voltages can allow for sample injection without the EK injection process. Ensure that the point at which particles enter the post array can be clearly visualized.

3. Move the microscope stage so the end of the post array can be clearly visualized.

4. Wait for particles to elute from the end of the post array. Plan for long videos, possible up to six minutes. Take a long initial video and modify it as necessary.

5. Repeat with at least one additional channel for at least three runs.

B.5 STABLE TRAPPING EXPERIMENTAL PROTOCOL

1. Inject particles the inlet reservoir of the device. Particle concentration should be reasonably high, with injection values between 1-5 μL.

2. The positive electrode should be placed in the inlet reservoir and the negative electrode should be placed in the outlet reservoir. Pressure balance the particles until minimal movement is observed by adding or removing media from the reservoirs.

3. Apply an initial voltage of 200 V for 10 seconds followed by higher voltages ramping up by either 100 V for initial experiments or 50 V once the stable trapping region is evident in the experiments. The initial voltage is to allow particles to enter the channel and to stop a high current spike upon application of the higher voltages. The total voltage application should last for 70 seconds.

4. Repeat the experiments for every individual particle and channel geometry of interest. A new channel should be used. If the old channel can be flushed with media or reused (minimum particle clumping is observed), the channel can be reused after a break period of at least five minutes.